EXPERIMENTAL INVESTIGATION OF INLET DISTORTION IN A MULTISTAGE AXIAL COMPRESSOR

by

Razvan Rusu

A Thesis

Submitted to the Faculty of Purdue University

In Partial Fulfillment of the Requirements for the degree of

Master of Science in Aeronautics and Astronautics

School of Aeronautics and Astronautics

West Lafayette, Indiana

December 2017

THE PURDUE UNIVERSITY GRADUATE SCHOOL
STATEMENT OF COMMITTEE APPROVAL

Dr. Nicole L. Key, Chair
Department of Mechanical Engineering
Dr. Carson D. Slabaugh
Department of Aeronautics and Astronautics
Dr. Guillermo Paniagua
Department of Mechanical Engineering

Approved by:
Dr. Wayne Chen
Head of the Graduate Program

ACKNOWLEDGMENTS

First of all, I would like to thank my advisor Dr. Nicole Key for giving me the opportunity to be part an incredible compressor research facility and for her support throughout this research. I also like to thank Dr. Guillermo Paniagua and Dr. Carson Slabaugh for serving on my advisory committee. I am also very grateful for the financial support of the GUIde V consortium which sponsored this project and my education here at Purdue.

This work would not have been possible without the selfless support and friendship of my lab mates: Nick, Doug, Ruben, Ben, Amelia, Will, Cameron, James, Trey, Nitya, and Matt. I can think of numerous occasions where each one of them has generously offered up their time to help with something unrelated to their own work. I would like to thank Dr. Lou Fangyuan, Dr. Yujun Leng, Grant Malicoat, John Fabian, and Rob McGuire for their guidance and expertise. I would also like to acknowledge the efforts of a past student, Dave Monk, who did a great job with the design of a large part of the hardware used for this study.

I would like to thank my parents, Cristian and Antonela Rusu, as well as my grandparents and extended family back in Romania for their love and support and for being incredible role-models of hard-work and perseverance. Finally, I want to thank my girlfriend Alicia Jarosz whose love and encouragement has been instrumental in helping me persist through challenges.

LIST OF TABLES

LIST OF FIGURES

NOMENCLATURE

Acronyms

AC	Alternating Current
AIP	Aerodynamic Interface Plane
AIR	Aerospace Information Report
AoA	Angle of Attack
ARD	Aerospace Resource Document
ARP	Aerospace Recommended Practice
ATA	Arrival Time Analysis
BDC	Bottom Dead Center
Blisk	Blade Integrated Disks
BTT	Blade Tip Timing
BVM	Blade Vibration Monitoring
CAD	Computer Aided Design
CFD	Computational Fluid Dynamics
COTS	Commercial Off-the-Shelf
CTA	Constant Temperature Anemometer
CWB	Chord-Wise Bending
DAQ	Digital Acquisition
DSA	Digital Sensor Arrays
DYNTECC	Dynamic Turbine Engine Compressor Code
EO	Engine Order
FEA	Finite Element Analysis
HL	High Loading
HPC	High-Pressure Compressor
IGV	Inlet Guide Vane
LL	Low Loading
MLC	Meanline Code
NL	Nominal Loading

NSMS	Non-Intrusive Stress Measurement System
P33	Purdue 3-Stage
PAV	Ring Average Pressure
PAVLOW	Average Low Pressure
PFAV	Face-Average Pressure
PS	Pressure Surface
PRAA	Rake Area-Average Pressure
PVAA	Vane Area-Average Pressure
R{#}	Rotor 1-3
S{#}	Stator 1-3
SLCC	Streamline Curvature Code
SNR	Signal-to-Noise Ratio
SS	Suction Surface
T	Torsion
TEACC	Turbine Engine Analysis Compressor Code
TPR	Total Pressure Ratio
TRL	Technology Readiness Level
VFD	Variable Frequency Drive
ΔPC/P	Circumferential Intensity Element
ΔPR/P	Radial Distortion Element

Symbols

∞	Freestream Conditions
a	Acquired Measurement
act	Actual
avg	Average
c	Corrected
corr	Corrected
i	Index Number
k	Index Number
max	Maximum

mech	Mechanical
min	Minimum
norm	Normalized
ps	Pitot-Static
ref	Reference
rms	Root-Mean-Square Value
sync	Synchronous Vibration
w	Wire
0	Stagnation Property

Subscripts

∞	Freestream Conditions
a	Acquired Measurement
act	Actual
avg	Average
c	Corrected
corr	Corrected
i	Index Number
k	Index Number
max	Maximum
mech	Mechanical
min	Minimum
norm	Normalized
ps	Pitot-Static
ref	Reference
rms	Root-Mean-Square Value
sync	Synchronous Vibration
w	Wire
0	Stagnation Property

ABSTRACT

Author: Rusu, Razvan. MSAA
Institution: Purdue University
Degree Received: December 2017
Title: Experimental Investigation of Inlet Distortion in a Multistage Axial Compressor
Major Professor: Dr. Nicole L. Key

The primary objective of this research is to present results and methodologies used to study total pressure inlet distortion in a multi-stage axial compressor environment. The study was performed at the Purdue 3-Stage Axial Compressor Facility (P3S) which models the final three stages of a production turbofan engine's high-pressure compressor (HPC). The goal of this study was twofold; first, to design, implement, and validate a circumferentially traversable total pressure inlet distortion generation system, and second, to demonstrate data acquisition methods to characterize the inter-stage total pressure flow fields to study the propagation and attenuation of a one-per-rev total pressure distortion. The datasets acquired for this study are intended to support the development and validation of novel computational tools and flow physics models for turbomachinery flow analysis.

Total pressure inlet distortion was generated using a series of low-porosity wire gauze screens placed upstream of the compressor in the inlet duct. The screens are mounted to a rotatable duct section that can be precisely controlled. The P3S compressor features fixed instrumentation stations located at the aerodynamic interface plane (AIP) and downstream and upstream of each vane row. Furthermore, the compressor features individually indexable stator vanes which can be traverse by up to two vane passages. Using a series of coordinated distortion and vane traverses, the total pressure flow field at the AIP and subsequent inter-stage stations was characterized with a high circumferential resolution.

The uniformity of the honeycomb carrier was demonstrated by characterizing the flow field at the AIP while no distortion screens where installed. Next, the distortion screen used for this study was selected following three iterations of porosity reduction. The selected screen consisted of a series of layered screens with a 100% radial extent and a 120° circumferential

extent. A detailed total pressure flow field characterization of the AIP was performed using the selected screen at nominal, low, and high compressor loading. Thermal anemometry was used to characterize the spatial variation in turbulence intensity at the AIP in an effort to further define inlet boundary conditions for future computational investigations.

Two data acquisition methods for the study of distortion propagation and attenuation were utilized in this study. The first method approximated the bulk flow through each vane passage using a single rake measurement positioned near the center of the passage. All vane passages were measured virtually by rotating the distortion upstream by an increment equal to one vane passage. This method proved successful in tracking the distortion propagation and attenuation from the AIP up until the compressor exit. A second, more detailed, inter-stage flow field characterization method was used that generated a total pressure field with a circumferential resolution of 880 increments, or one every 0.41°. The resulting fields demonstrated the importance of secondary flows in the propagation of a total pressure distortion at the different loading conditions investigated.

A second objective of this research was to document proposals and design efforts to outfit the existing P3S research compressor with a strain gage telemetry system. The purpose of this system is to validate and supplement existing blade tip timing data on the embedded rotor stage to support the development and validation of novel aeromechanical analysis tools. Integration strategies and telemetry considerations are discussed based on proposals and consultation provided by suppliers.

CHAPTER 1. INTRODUCTION

1.1 Motivation

Gas turbine engines are essential to aerospace propulsion and power generation applications and have reached an extraordinary level of performance, reliability, and design maturity due to almost a century of research, development, and refinement. To arrive at this level of maturity, engine designers rely on well-tested analytical models, experimental correlations, and increasingly more on computational methods. As a result, gas turbines are among some of the most efficient and dependable means of power generation reaching efficiencies in excess of 90% (Logan & Roy, 2003).

However, there is continued pressure to further improve engine efficiency, cut-back on greenhouse gas emissions, reduce engine noise, and provide additional cost savings to operators by reducing maintenance costs (Neumann et al., 2015). Much attention is paid to improving engine efficiency by further detailed studies on flow phenomena and aerodynamic losses, but equally important are studies of factors relating to engine safety, reliability, and robustness (Hamed & Numbers, 1997). Engine manufacturers are, therefore, looking to achieve significant weight savings and performance improvements by taking advantage of new lightweight materials and advances in manufacturing techniques to design more complex and more optimized blade geometries while also reducing the number of stages. This trend to decrease the weight of components while simultaneously increasing stage loading renders them increasingly susceptible to dangerous vibrations, high component stresses, and reduced stability margins (Holzinger, Wartzek, Schiffer, Leichtfuss, & Nestle, 2016).

For a typical life of a machine or component, the highest probability of failure occurs either at the beginning of life or near then end (Rao, 2011). The most common mechanisms of blade failure in turbomachinery are pre-existing defects, fatigue, creep, stress rupture, corrosion, malfunction, and FOD in decreasing order of significance (Logan & Roy, 2003). The highest percentages of failures occur either due to preexisting defects or end-of-life

fatigue. In either case, vibrations are the primary driver for the resulting failure modes which are typically due to crack growth propagation (Beauseroy & Lengellé, 2007; Reinhardt, Kadambi, & Quinn, 1995).

Design for vibration is even more critical for new compressor rotor designs called blade integrated disks (Blisks) (Neumann et al., 2015). A comparison between conventional dovetail connections and more modern blisk rotors is shown in Figure 1-1 and Figure 1-2. Blisks are up to 20% lighter than conventional rotor designs and are also able to withstand higher maximum rotational velocities which results in higher pressure ratios and efficiency factors (Holzinger et al., 2016; Klauke, Kühhorn, Beirow, & Golze, 2009). Although there are numerous advantages from a performance standpoint, blisks are more susceptible to vibration. In conventional designs, the dovetail or fir-tree interface provides friction between the blades and the hub which aided in damping out vibration. Blisks, which are machined from a single block of material, have greatly reduced structural damping and must rely on material damping properties for mechanical damping and aerodynamic damping (Holzinger et al., 2016). Furthermore, blisks are especially prone to a phenomenon referred to as mistuning which results from small manufacturing differences between individual blades (Beirow, Kühhorn, Figaschewsky, & Nipkau, 2015; Klauke et al., 2009). Mistuning makes it more difficult to accurately predict the vibrational characteristics of a blisk and also has the potential to dramatically increase the forced response (Beauseroy & Lengellé, 2007; Lim, Pierre, & Castanier, 2006).

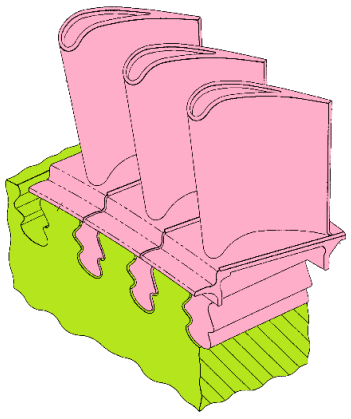

Figure 1-1. Conventional Dovetail Assembly (EP1288440 A2, 2003)

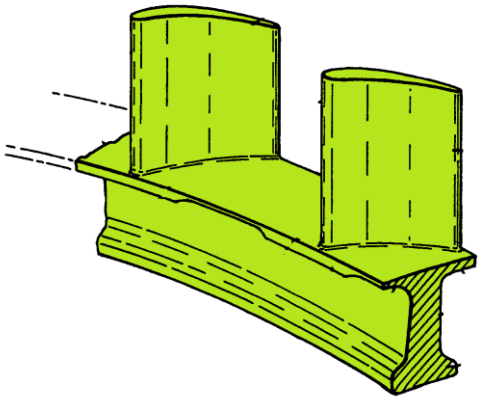

Figure 1-2. Integrally Bladed Disc Rotor (Blisk) (US7445433 B2, 2008)

Dangerous operating conditions also arise due to the effect of inlet flow distortion on engine performance and stability (Breuer & Bissinger, 2010; William T. Cousins, 2004; Hamed & Numbers, 1997). Inlet distortion can also be a significant contributor to engine vibrations and high cycle fatigue (HCF), which is why it is an ongoing topic of research and a critical area for engine certification (William T. Cousins, Georges, & Rezaei, 2003; Hamed & Numbers, 1997). During the early stages of gas turbine engine design, engineers typically use ideal operating assumptions such as uniform inlet flow (William T. Cousins, 2004). Furthermore, the engine and inlet have traditionally been designed in isolation by the engine manufacturer and airframer, respectively, using previously agreed upon flow conditions at an interface plane. For early aircraft designs, this method has been adequate because it was supported by extensive experimental and flight testing coupled with conservative surge margins. Modern aircraft designs feature more complex inlet geometries, and military aircraft are required to reliably undergo increasingly demanding flight maneuvers, which makes engine/inlet integration a more critical design parameter earlier in the design process (William T. Cousins et al., 2003).

It is important to consider true inlet conditions experienced during all stages of a flight mission since the presence of distortion typically deteriorates performance and stability characteristics (Breuer & Bissinger, 2010; Johnsen & Bullock, 1965). As a result, inlet distortion is a major factor when selecting a compressor's operating line to assure that a sufficient instability margin is maintained during all stages of flight. As previously mentioned, newer designs are trending towards fewer, more highly loaded compressor stages, which means setting the operating line closer to the surge line. Developing analysis tools and a comprehensive understanding of inlet distortion effects early in the design process can prevent the need for costly redesign.

1.2 GUIde V Consortium

The GUIde V Consortium is composed of universities, industry and government agency partners working together to sponsor research projects in structures and fluid mechanics in turbomachinery. The mission of the GUIde V Consortium's research efforts is twofold. First, they strive to further the understanding and control of turbomachinery blade response to improve engine reliability and reduce the time and cost of aeromechanical related design activities. Second, by promoting international cooperation between academia, industry, and government agencies, they hope to increase the technology transfer rate to industry ("GUIde 5 Consortium," n.d.).

Purdue University is involved in a joint project with Duke University titled, "Grand Challenges in Turbomachinery Forced Response and Non-Synchronous Vibration (NSV)". This project combines experimental and computational approaches to study topics in aeromechanics and unsteady aerodynamics. Studies include the effects of stator asymmetry on the forced response of the embedded stage in a three-stage axial compressor and the effects of inlet distortion. Purdue has provided the majority of the experimental results while Duke has been responsible for the computational effort.

1.3 Inlet Distortion

1.3.1 Overview

Inlet distortion is defined as any flow property deviation from uniform ideal conditions, which can include variations in pressure, temperature, or flow angle (Ariga, Kasai, Masuda, Watanabe, & Watanabe, 1983). For the first couple of decades of gas turbine engine design, engineers did not concern themselves with inlet distortion effects since the majority of the research and development efforts at the time were focused on the design of the engines themselves. In the 1960's, engineers began to realize that total pressure non-uniformity in the inlet flow had significant effects on compressor performance and stability. Soon after, temperature inlet distortion issues were brought to light due to rocket exhaust and gun gas ingestion in military aircraft. The final form of inlet distortion studied was swirl distortion as that found mainly in more complex inlet (William T. Cousins, 2004). Decades of

experimental and analytical studies have demonstrated that inlet distortion generally contributes to a reduction in stability margin, degrades engine performance, and amplifies vibrational modes that contribute to high cycle fatigue (Ariga et al., 1983; Greitzer, 1980; Hamed & Numbers, 1997; Logan & Roy, 2003).

The effect of inlet distortion on engine performance is different depending on the type of distortion present. Inlet distortions are typically categorized according the spatial distribution, intensity, and temporal variation (Breuer & Bissinger, 2010). Distortion can be either steady or unsteady. A distortion is considered to be steady if the following condition is satisfied in the range of 0 to 1000Hz frequency (SAE, 2013):

$$\left(\frac{\Delta P}{P}\right)_{RMS} = \frac{P_{\max} - P_{\min}}{P_{avg}} < 0.01 = 1\% \tag{1.1}$$

where P_{max}, P_{min}, and P_{avg} are the maximum, minimum, and average pressure readings, respectively, in a series of pressure readings at any given point in the inlet. Furthermore, inlet distortions can be divided based on their spatial distribution into radial, circumferential, or some combination of the two (Ariga et al., 1983). Figure 1-3 illustrates idealized inlet distortion shapes, which are typically used during experimental investigations. These classical inlet distortion shapes are used during testing to establish engine sensitivity characteristics.

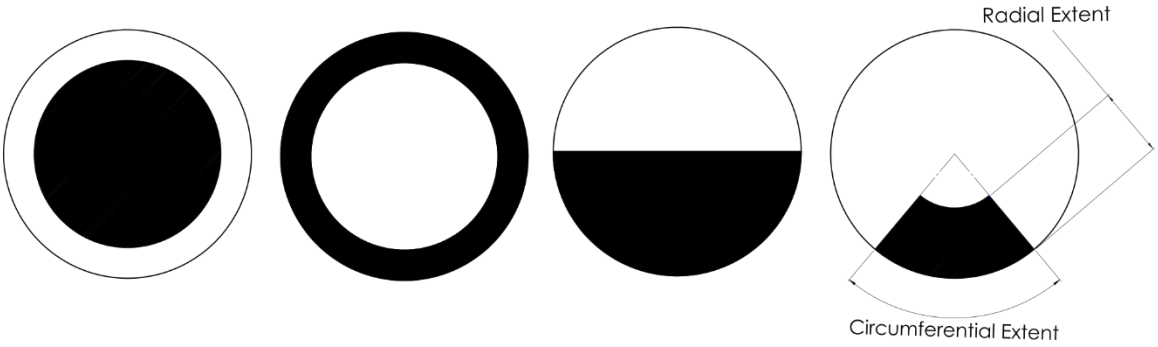

Figure 1-3. Classical Inlet Distortion Shapes

The most common type of distortion observed in aircraft engines is total pressure distortion. There are numerous sources of pressure distortion upstream of an aircraft engine inlet including inlet shape, turbulence, and aircraft maneuvers among others. Pressure distortion is most often attributed to the inlet geometry that causes non-axisymmetric local boundary layer growth, streamwise vorticity, and possible separation zones that may occur frequently during high angle of attack (AoA) flight or in the presence of a strong crosswind (W. T. Cousins, Dalton, Andersen, & Bobula, 1994; Greitzer, 1980; Johnsen & Bullock, 1965).

Temperature distortion mainly concerns military aircraft and helicopters. It is not often tested experimentally due to the high degree of difficulty and cost involved in adding or removing fixed amounts of energy to the inlet flow in a repeatable manner. Temperature distortion has a greater effect on engine stability than a pressure distortion (W. T. Cousins et al., 1994; Kurzke, 2008). Studies by Cousins et. al and Braithwaite and Soeder have experimentally shown that compressor performance is further complicated by the presence of both temperature and pressure inlet distortions (Braithwaite & Soeder, 1980; W. T. Cousins et al., 1994). The change in compressor performance is driven by both the intensity and the pattern of the combined temperature and pressure distortion, and therefore, it is important that they be modelled or tested together.

The final category of inlet distortions is swirl, or flow angle distortion. There are three types of swirl including bulk, peak, and vortex swirl (William T. Cousins, 2004). Bulk swirl describes a uniformly rotating inlet flow field. This type of distortion may appear to have a uniform pressure profile, but the non-axial inlet flow angle will affect blade incidence angle. When the swirl is opposite to the rotation of the rotor, it is referred to as pre-swirl resulting in a reduction in incidence and, thus, a decreased loading and vice versa for counter-swirl, which increases the rotor loading. Peak Swirl is most common in helicopter side inlets where each side will have swirl in opposite directions. The final type of swirl distortion is vortex swirl. Vortex swirl is defined by a local vortex in a concentrated region, which creates both pre-swirl and counter swirl on one sector of the rotor. Vortex

swirl, for example, may be experienced when an engine close to the ground ingests a vortex that is created by a wake shed from the forward part of the fuselage.

1.3.2 Distortion Descriptors and Industry Standards

Historically, each engine manufacturer studied inlet distortion in complete isolation, and thus, each developed their own unique form of characterizing and describing results. This caused a lot of confusion in the gas turbine community when trying to communicate and compare inlet distortion data. The Society of Automotive Engineers (SAE) commissioned a committee composed of different members from the gas turbine community to devise a unified, agreed upon industry standard for reporting inlet distortion data. The result was an aerospace recommended practice (ARP) document titled "Gas Turbines Inlet Flow Distortion Guidelines", more commonly referred to by its designation of ARP-1420 (William T. Cousins, 2004; SAE, 2011).

Results are often reported in a non-dimensional form via distortion descriptors or indices, which define the distortion and change in compressor performance. Despite the publishing of ARP-1420, it is still common to find results published in multiple standards. Work done by Campbell (1981) compared a dozen different inlet distortion descriptors including those defined in ARP-1420 and concluded that there was no single method that proved ideal for all cases, but the ARP-1420 indices provided the most consistent results (Campbell, 1981; William T. Cousins, 2004). In 1983, a more comprehensive companion document to ARP-1420 was published. The Aerospace Information Report (AIR) 1419 discusses in greater detail the standards of inlet distortion reporting, engine stability analysis and even recommended instrumentation (William T. Cousins, 2004; SAE, 2013). A similar standards document exists for inlet temperature distortion titled Aerospace Resource Document (ARD) 50015; however, this is beyond the scope of this study and is, therefore, not discussed.

All inlet distortion descriptors are measured and defined at the Aerodynamic Interface Plane (AIP) which is typically set by the engine manufacturer as a reference plane where the inlet flow to the engine is defined. The AIP should be located close to the engine face

plane is defined as the leading edge of the first strut, vane or blade row. Typically, engine manufacturers set the AIP at the location of the most upstream flange of the engine which interfaces with the engine inlet. It is important to define and agree upon the location early on in the design of an engine or experiment to assure repeatability of flow measurements and analyses. The AIP must remain the same for the entire design life of the engine from analysis to flight testing. Finally, the location of the AIP must be such that all engine airflow passes through it including any auxiliary bleed that may influence the inlet distortion (SAE, 2011).

The location of the AIP is also the location of the instrumentation plane where flow properties are captured via a rake or probe array. There is no minimum number or recommended configuration for AIP probes. ARP-1420 provides a typical array as consisting of eight equally spaced rakes each with five probes located at the centroids of equal areas (SAE, 2011). Cousins warns that this configuration is not applicable to all cases, but rather, the number and probe configuration should be selected such that it adequately captures the flow patterns of interest while also being mindful to not introduce excessive blockage (William T. Cousins, 2004). For consistency, ARP-1420 states that only linear interpolation must be used between all data points taken at the AIP.

1.3.3 Effect on Compressor Performance and Stability

Axial compressors increase the static pressure by adding kinetic energy to the flow via the rotor and converting that kinetic energy to an increase in static pressure via diffusion. Work input by the rotors is achieved by changing the angular momentum of the flow while the static pressure rise is a result of diffusion occurring within each blade passage. A rotor-stator pair is referred to as a stage and most axial compressors utilize multiple stages to achieve the desired pressure rise.

Compressor blades are sensitive to the incidence angle of the incoming flow much like airfoils on aircraft wings. Similar to wings, compressor blades can stall if a critical incidence angle (analogous to angle-of-attack) is exceeded. An increase in rotor blade incidence angle results in more work being done on the flow and hence a greater increase

in pressure. Once the critical incidence angle is exceeded, the flow over the blades will separate which is a phenomenon referred to as compressor stall or surge. At this point, the flow is extremely unsteady and further pressure rise is impossible and there is often a significant amount of reversed flow within the compressor.

Compressor surge is defined by large global fluctuations in mass flow rate while rotating stall is defined by circumferential pockets of flow separation and reduced local mass flow rate that may rotate around the annulus (Greitzer, 1980). Surge and stall may happen in isolation or simultaneously, and the exact instability mechanism typically varies between different compressor designs. Figure 1-4 illustrates the differences between rotating stall and surge instabilities.

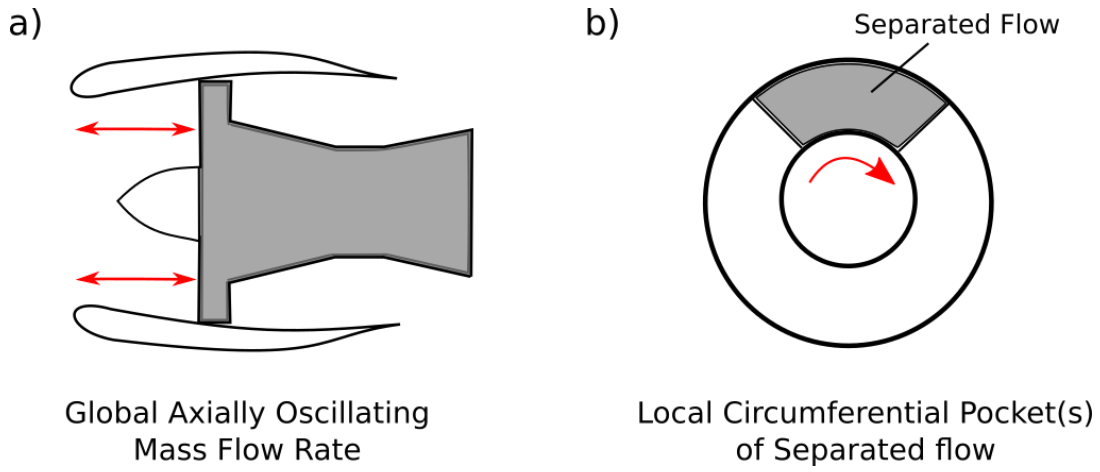

Figure 1-4. a) Surge Instability vs. b) Rotating Stall in a Gas Turbine Engine

Regardless of which type of instability occurs, the stall line or surge line on a compressor map represents the upper limit of safe and useful compressor operational range (Greitzer, 1980). Knowledge of the exact location of this line at all speedlines is important for the engine designer. Inlet distortion can greatly affect this line, and therefore, it is crucial that its effects are understood and quantified to maintain an acceptable stability margin during all phases of operation.

Central to the discussion of the flow mechanics surrounding inlet distortion is an understanding the boundary conditions imposed on a compressor. Regardless of compressor inlet conditions, the boundary conditions downstream are typically impose a constant exit pressure demand either by aerodynamic chocking or exhausting to a uniform back pressure. Therefore, both the distorted and undistorted segments of the compressor must ultimately reach the same exit static pressure regardless of the state at the inlet (Breuer & Bissinger, 2010).

The velocity triangles for an undistorted and distorted flow compressor segment are shown in the Figure 1-5. Total pressure distortion causes a velocity deficit. A region of lower velocity inlet flow corresponds to a lower total pressure. For a given wheel speed, *U*, a lower inlet velocity will result in a lower absolute velocity, *V*, leading to an increase in incidence angle, β versus the undistorted case. Figure 1-5 also shows the effect of pressure distortion on the operating point. The distorted segment operates at a higher loading compared to the undistorted segment and the weighted average operating point which takes into account the overall effect of the distortion lies between the two points. Because inlet temperature is constant, the points will all lie on the same corrected speed line (Breuer & Bissinger, 2010).

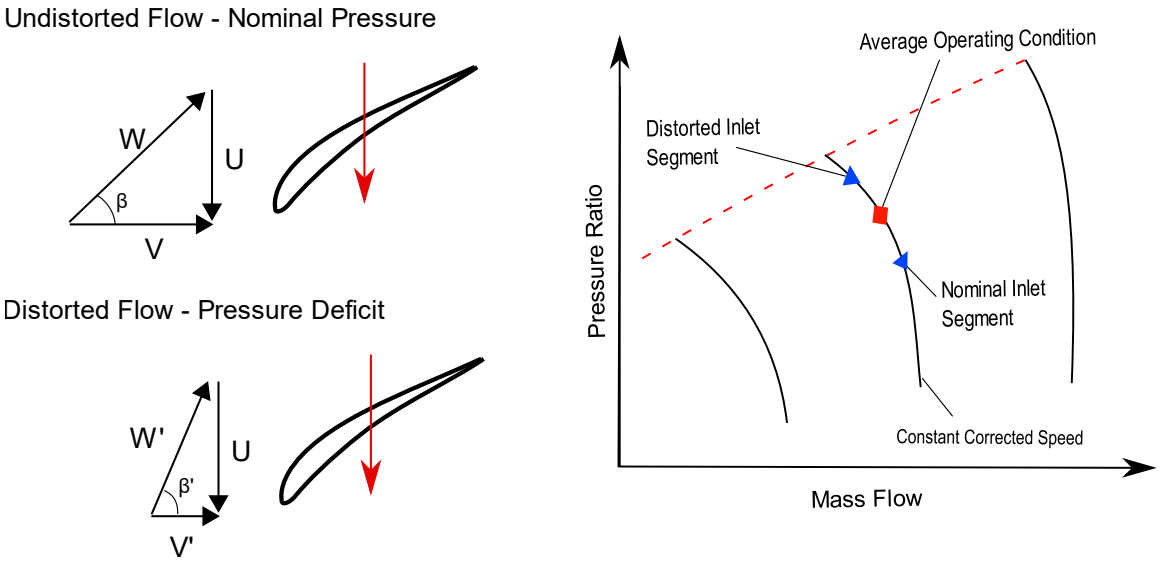

Figure 1-5. Effect of Total Pressure Distortion Compressor Performance

Temperature distortion effects are best understood when discussed in relation to compressor enthalpy rise. Enthalpy rise in compressors is dependent on pressure rise and temperature as illustrated in Figure 1-6a. An increase in temperature at the inlet corresponds to an increase in enthalpy at inlet pressure, P_1. Because lines of constant pressure diverge on an enthalpy-entropy (h-s) diagram, the consequence of increasing flow temperature is that a larger enthalpy rise is required to reach the compressor exit pressure, P_2. Therefore, a greater work input is required to achieve a given pressure ratio at increased inlet flow temperature. The effect of temperature distortion on a compressor map is shown in Figure 1-6b. The distorted segment's operating point will be at a lower corrected speed versus the nominal segment for a given compressor mechanical speed. The pressure remains largely unaffected, but the overall effect is that the combined operating point is shifted to a lower corrected speed line. This nearly horizontal translation of the operating point brings the operating point closer to the surge line, and therefore, temperature distortion tends to have destabilizing effect on compressors (Breuer & Bissinger, 2010).

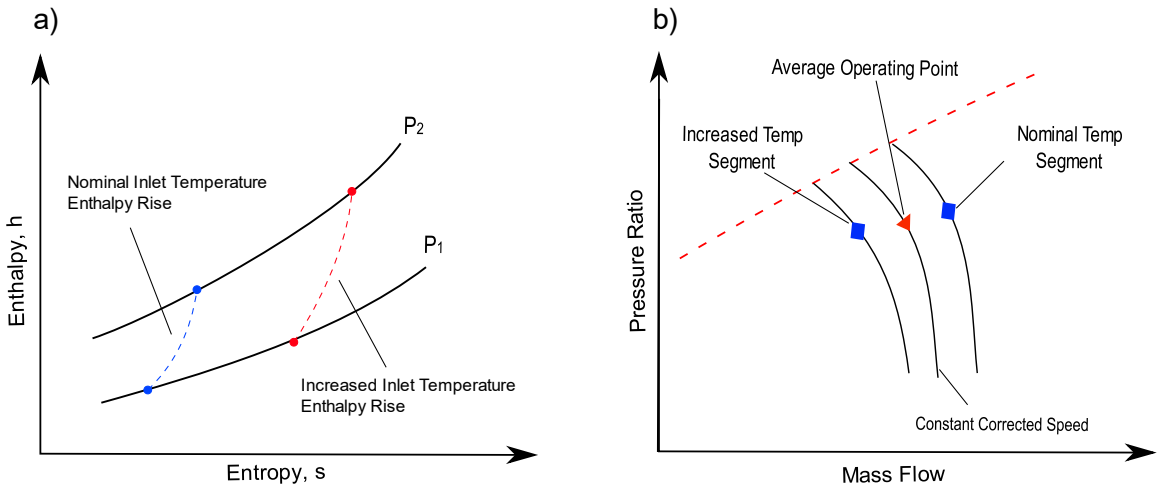

Figure 1-6. Effect of Temperature Distortion on Compressor Performance

Swirl distortion affects compressors in a manner similar to an inlet guide vane (IGV) stator row (Breuer & Bissinger, 2010). IGVs are typically used to turn the absolute flow velocity away from axial so that the compressor can accommodate an increased mass flow rate for a given limit Mach number at the blade tip. The effect of the swirl depends on whether the

swirl is co-rotating (pre-swirl) or counter-rotating (counter-swirl). Figure 1-7 shows the effect of each type of swirl on the blade velocity triangles. For a given rotor speed, pre-swirl acts to reduce the incidence angle and mass flow rate by reducing the magnitude of the axial component of the absolute velocity. Counter-swirl increases the incidence and mass flow rate. Swirl shifts the speed line with an accompanying slight change in pressure ratio (William T. Cousins & Davis, 2011). Most compressors have an IGV to condition the flow going into the first blade row. This typically eliminates most of the inlet bulk swirl.

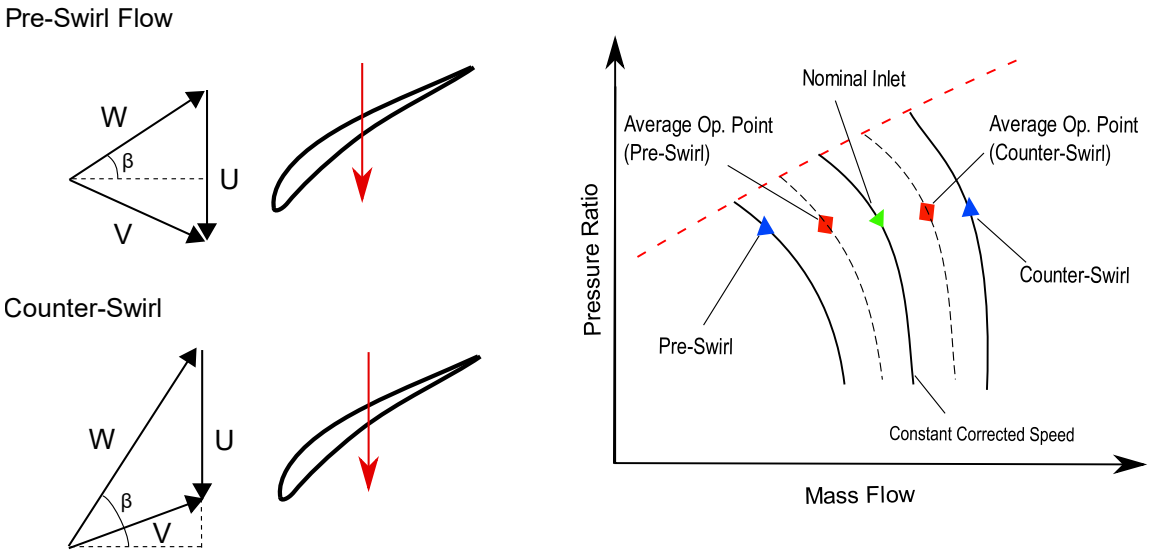

Figure 1-7. Effect of Swirl Distortion on Compressor Performance

The circumferential extent of an inlet distortion is an important parameter in assessing the degree to which it will affect compressor performance and stability. There is a lower limit beyond which the compressor is unlikely to react to a flow distortion. ARP-1420 suggests that this critical angle must be determined experimentally or, in the absence of data, taken to be 25° (SAE, 2011). Cousins et al. demonstrated that the time for a flow particle to travel from the leading edge of the blade to the blade passage throat can be used predict the sensitivity of the rotor to inlet distortion (W. T. Cousins et al., 1994). As a rule of thumb for axial compressors, Cousins quotes that at least 4-5 blades must be simultaneously affected to produce an observable change in stability (William T. Cousins, 2004; Greitzer,

1980). Therefore, the minimum circumferential extent required at a given rotational speed can be calculated angle that the rotor rotates during 4-5 blade time constants.

The blade time constant explains why axial compressors are less tolerant to inlet flow distortion than centrifugal compressors. The aerodynamic time constant associated with blade stalling and recovery is a function of blade chord, hand ence, the time constant of a centrifugal compressor is much larger than that of an axial compressor meaning that an impeller blade is more desensitized to short duration flow defects (W. T. Cousins et al., 1994).

There is no consensus in the literature as to the extent to which compressor efficiency is influenced by inlet distortion. Theoretical and experimental results in literature have claimed a reduction in efficiency of anywhere from 1-5% (Kurzke, 2008). This relatively small change in efficiency can be explained with reference to a typical compressor map shown in Figure 1-8. The contour lines define the regions of constant efficiency which are commonly referred to as efficiency islands. The greater the intensity of the inlet distortion, the farther apart will be the operating points of the distorted and undistorted compressor segments and hence the resultant operating point will be shifted by a greater amount from the clean inlet case. Therefore, the magnitude of efficiency loss is said to be proportional to the distortion intensity. However, because efficiency islands are relatively flat in shape, the loss in efficiency will never be very large (Kurzke, 2008).

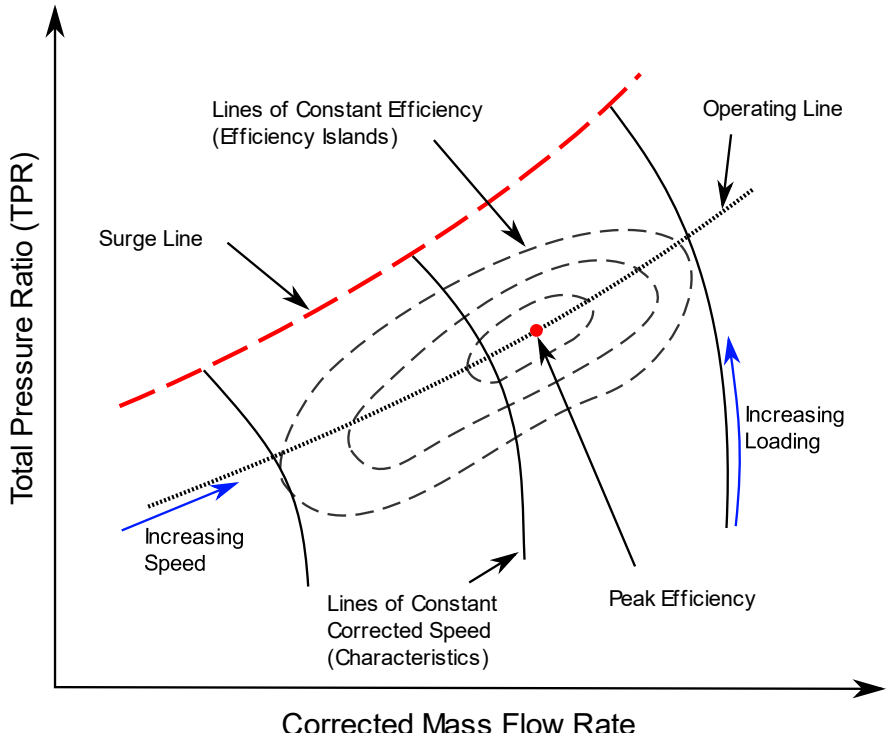

Figure 1-8. Typical Compressor Map

1.3.4 Propagation and Attenuation in a Multistage Axial Compressor

The majority of propulsion gas turbine engines feature multi-stage compressors, therefore, knowledge of how inlet distortion propagates and attenuates is beneficial during the early design stages. Distortion propagation is also important for defining the flow conditions entering the combustor downstream of the compressor where non-uniformities can contribute to flame instabilities. Few experimental inlet distortion studies found in literature have performed detailed inter-stage flow measurements on multi-stage compressors, however, there is a general consensus that the degree of attenuation varies depending on the type of inlet distortion and number of stages.

A total pressure distortion at the inlet will result in a combined total pressure and total temperature distortion following the non-uniform work input across each stage (Breuer & Bissinger, 2010). Varying rotor incidence due to the total pressure distortion, as illustrated earlier in Figure 1-5, results in different work input across the rotor, and hence, the

associated temperature rise will be different. Braithwaite (1973) investigated the propagation of total pressure distortion in an eight-stage single spool turbojet engine and observed that the total pressure distortion was almost entirely attenuated at the compressor exit (Braithwaite, Graber, & Mehalic, 1973). Further experimental studies by Braithwaite and Soeder (1979) measured flow conditions after every third stage in a 16-stage compressor of a turbofan engine and observed that total pressure distortion decreased nearly linearly to the compressor exit where it was almost entire attenuated (Braithwaite & Soeder, 1980). Investigations by Roberts et al. (1968) concluded that the attenuation per stage decreases as the number of compressor stages is increased (Roberts, Plourde, & Smakula, 1968).

The same studies mentioned above by Braithwaite and Soeder also investigated the propagation of total temperature inlet distortion. Braithwaite (1973) measured a partial attenuation of the total temperature distortion of only 29% at the exit of the 8-stage compressor with an accompanying 45° rotation (Braithwaite et al., 1973). Braithwaite and Soeder (1979) observed a similar linear decrease in total temperature through the 16-stage compressor with approximately 22% attenuation at the exit of the final stage.

As previously discussed, the presence of an IGV typically removes the majority of bulk swirl present in the inlet flow. Davis (2002) presented numerical results simulating bulk swirl distortion that showed that bulk swirl, regardless of direction, is almost entirely eliminated after passing through the first rotor (Davis, Hale, & Beale, 2002). Therefore, in the absence of an IGV, swirl distortion typically has a significant impact on the first stage only.

1.3.5 Effect on Turbomachinery Vibrations

Inlet distortion is a major contributor to both synchronous and non-synchronous flow induced vibrations. A steady distortion can lead to a forced vibration condition in manner similar to the effect caused by wakes and potential fields. The change in blade loading as it passes through pockets of distortion over one revolution results in a synchronous forcing function. The engine order excitation can be related to the multiple-per-rev descriptor of

the circumferential inlet distortion (William T. Cousins, 2004). Furthermore, blade vibration amplitude is directly proportional to distortion intensity (Danforth, 1975). If the shape of the inlet distortion is known, designers can typically account for forced response using reference to past experimentally determined inlet distortion correlations and a Campbell diagram to aid in selecting a safe operating line. (Hamed & Numbers, 1997). The resonant crossings can be avoided by selecting a different operating speed if possible, or alternatively, by changing the resonant crossing. The resonant crossing may be altered by changing the synchronous forcing function or via a change in the modal frequency of the part. The forcing function can be altered through aerodynamic changes to eliminate or alleviate the inlet distortion while the modal frequency curves can be changed via changes in material or part geometry. It is preferable to resolve these types of issues through aerodynamic changes as opposed to geometry changes to avoid increasing the engine weight.

Unsteady inlet distortions include oscillatory and turbulent flows which may be caused by phenomena such as vortex shedding, acoustic resonance, or separated flow. This category of inlet distortion results in non-synchronous vibrations such as flutter or operating point excursions due to large fluctuations in incidence angle (Danforth, 1975). Conditions leading to non-synchronous vibrations are more difficult to replicate in a test lab environment, and therefore, much of the literature on unsteady inlet distortions is based on flight test data. Hamed and Numbers provide an overview of relevant studies on turbulent and oscillatory inlet flows (Hamed & Numbers, 1997). They point to studies that showed how random turbulence could, under certain conditions, cohere around duct acoustic resonances and have the potential to produce a blade forcing function.

As previously discussed, all forms of inlet distortion have the effect of altering the operating point of the compressor and translating the instability lines (SAE, 2013). Figure 1-9 shows various operating limits on a typical compressor map. Considerations of operating point excursions allow proper selection the operating line of a compressor so that the ingestion of distorted flow does not cause the compressor to enter a region of instability (Logan & Roy, 2003; SAE, 2013).

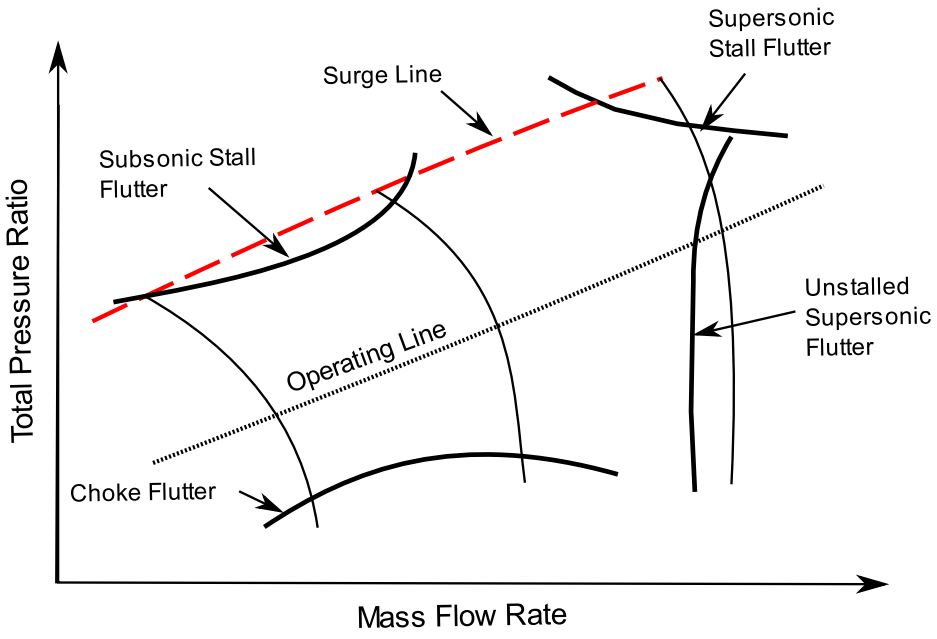

Figure 1-9. Flutter Instability Regions

1.3.6 Computational Methods

Analytical models are extremely important in reducing the amount of experimental validation required and, therefore, can significantly reduce both cost and time to market of new gas turbine engines (Braithwaite & Soeder, 1980). According to the authors of ARP-1420, analytical models alone should not be used to certify a new compressor design, but rather, computational techniques can facilitate early design phase trade studies by trends and comparative data (SAE, 2011). Numerous analytical and computational tools have been developed to model inlet distortion effects ranging from low fidelity 1D codes to complex three-dimensional Navier-Stokes numerical solvers of entire compressors.

The earliest and most widely used model is the parallel compressor theory. It was first suggested by Pearson and Mckenzie (1959) to predict the effects of total pressure inlet distortion (William T. Cousins, 2004; Kurzke, 2008). This theory is applicable with reasonable accuracy to steady state circumferential distortion, as demonstrated in studies by Longley (1990) (Longley, 1990) and Mazzawy (1977) (Mazzawy, 1977). Using this

model, two identical compressors are analyzed with uniform inlet flow and are exhausting to the same back pressure boundary condition. One is analyzed at the undistorted inlet condition while the other is analyzed at the distorted inlet condition. Each compressor is analyzed using tradition one-dimensional dynamic models (SAE, 2013). This results in two different operating points on the map, as illustrated in Figure 1-10. The effect of each sector is combined by computing a weighted average to find the distorted operating point and efficiency (Breuer & Bissinger, 2010; William T. Cousins, 2004; Greitzer, 1980; Kurzke, 2008). In regards to stability prediction, the entire compressor is assumed to become unstable as soon as any one of the segments stalls, regardless of where the combined operating point is the map (SAE, 2013).

Reid (1969) showed that there are some limitations to the model, depending on the circumferential extent. There exists some non-zero critical angle of circumferential extent at which the loss in performance is a maximum (William T. Cousins, 2004). Parallel compressor theory also loses accuracy beyond the point where either of the sections reaches peak pressure rise. Further increase in loading results in flow separation and the rotor can no longer be treated in a quasi-steady manner. Furthermore, near the stall line, interaction between the distorted and undistorted segments of the compressor become significant (Breuer & Bissinger, 2010; Greitzer, 1980). More recent developments to this model include unsteady effects that account for the effect of time-varying flow fields as well as cross flow between the segments. This improves the prediction by relaxing the assumption that the two compressor segments are entirely independent (Breuer & Bissinger, 2010). This theory has also been extended to more than two segments which permits the modelling of more complex inlet distortions (Kurzke, 2008).

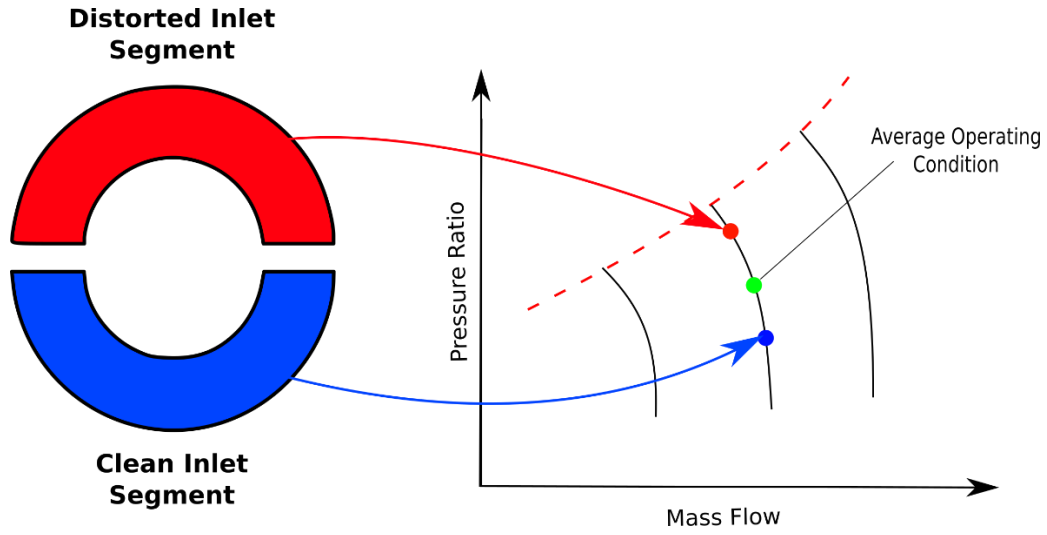

Figure 1-10. Parallel Compressor Model

If the distortion is purely radial in nature, the performance can be predicted using traditional streamline curvature codes, SLCC, or meanline codes, MLC. The distorted inlet flow is treated in the same manner as an off-design condition (Greitzer, 1980). For these codes to be accurate in predicting highly distorted inlet conditions, loss and deviation coefficients for the compressor geometry must well established (Breuer & Bissinger, 2010).

Under real world conditions, distortions are rarely entirely radial or entirely circumferential, but rather a combination of the two. Recent efforts in analytical methods are trying to account for more realistic and complex distortion patterns. Examples of such codes are the Turbine Engine Analysis Compressor Code (TEACC) and Dynamic Turbine Engine Compressor Code (DYNTECC) (Breuer & Bissinger, 2010; William T. Cousins et al., 2003; Hale, Davis, & Sirbaugh, 2004). The goal of these codes is to improve on the basic parallel compressor theory and provide a simple tool with reasonable accuracy and fast computation time. Traditionally, engines and inlets are designed in isolation from one another, whereas Hale et al. have demonstrated that TEACC can allow engine designers to analyze the two components simultaneously and gain greater insight into their interaction even during early design stages (Hale et al., 2004).

Presently, there are many research efforts to develop design methods using computational fluid dynamics (CFD) codes to account for inlet distortion. CFD studies in this area are complicated by the fact that the entire compressor annulus needs to be modelled as opposed to a single blade passage which increases the computational demand significantly compared to traditional turbomachinery CFD runs. Computational investigations by Yao, Gorrell, and Wadia have demonstrated that Reynolds Averaged Navier-Stokes (RANS) CFD can accurately capture the flow physics due to inlet distortion in a multistage compressor. However, there is still work to be done to improve the accuracy of performance and loss predictions (Yao, Gorrell, & Wadia, 2010a, 2010b). Despite the recent advancements in numerical methods and computing power, such a study remains extremely time intensive and, therefore, impractical to perform in early design stages (Breuer & Bissinger, 2010).

1.4 Methods of Simulating Inlet Distortion

1.4.1 Overview

Due to the difficulty of simulating the real world conditions that create inlet distortion, such as high angle of attack flight or fuselage interactions, test engineers try to replicate expected distortion patterns in a subscale, component, or engine direct-connect test (Beale, Cramer, & King, 2002). The most common method of generating inlet total pressure distortion is to use wire gauze screens (Logan & Roy, 2003). Other studies have also successfully used metallic protrusions/fingers (William T. Cousins, 2004) and perforated sheets (Breuer & Bissinger, 2010). A more complicated method is to utilize an air jet distortion generator. A total pressure drop is achieved as a result of the decreased momentum caused by the interaction of the jet and the freestream. These generators are typically installed in a circular section upstream of the AIP. To avoid interaction between the compressor and the distortion generator, Breuer and Bissinger recommend at least 1.5-2 pipe diameters separation (Breuer & Bissinger, 2010). Finally, many studies utilize a rotating distortion generator which allows for greater circumferential resolution in AIP measurements with fewer probes.

Experimental techniques of replicating temperature distortion are typically more challenging than pressure or swirl distortion techniques. Methods of accurately adding or removing energy from the inlet flow require expensive and complicated hardware. Past studies have utilized steam injection, rocket grain burners and hydrogen or propane burners. The most common method is the hydrogen gas burner developed by NASA. It is the most accurate energy addition method and allows for a high degree of control of both spatial and time variant distortion (Beale et al., 2002). Numerous studies have also combined burners with screens to study the effects of combine total pressure and temperature distortion (W. T. Cousins et al., 1994).

Bulk swirl distortion is often introduced via inlet guide vanes whereas more localized swirl distortion patterns require complex arrangements of vortex shedding bodies in the upstream flow. For increased accuracy, it is also common to install the actual inlet geometry to the face of the engine or compressor. In-flight distortion patterns can be more accurately replicated if the incoming flow angle and Mach number can be replicated.

1.4.2 Pressure Drop Across a Wire Gauze Screen

Wire gauze screens introduce a blockage in the duct that reduces the velocity and hence the total pressure of flow. With careful tailoring of the shape and porosity of screens placed normal to the flow in an inlet duct, a specified total pressure profile may be generated which is why screens are so useful for inlet distortion generation. The exact shape and porosity of the screen is typically found via iteration however test engineers often use simplified analytical models as a starting point (SAE, 2013).

Simplified models typically treat the screen as a finite discontinuity which can be modelled using actuator-sheet theory. This theory stipulates that momentum is conserved and therefore, the drag force is equal to the pressure drop across the screen. Numerous models have been developed based on experimental correlations and a through discussion is included in a review by Laws & Lively (Laws & Livesey, 2003). A detailed discussion of select models is included in subsequent chapters. It is important to note that wire gauze screens are inherently anisotropic due to the nature of the manufacturing process which can

lead to variations in wire diameter and spacing. There are more involved analytical models such as those developed by Jackson (1972) which take into account the effect of screen non-uniformities on resistance coefficient (Jackson, 1972; Laws & Livesey, 2003).

Another cause of downstream profile non-uniformity is the bulge effect first observed by Owen and Zienkiewicz (1957) with screens with $K > 1$ (Laws & Livesey, 2003). The bulge effect is a term used to described the non-linear profile that results in the boundary layer due to the difference in pressure drop between the bulk flow and the slower moving boundary layer flow. Furthermore, the flow downstream of the screens is also significantly affected by presences of bugs, dirt, or dust and therefore upstream air filters and frequent inspection are recommended. Despite the relatively good agreement between analytical models and experimental data, it is still common practice to iterate screen parameters experimentally for increased accuracy. Experienced test labs are capable of replicating a given inlet distortion intensity and pattern with 3-4 screen iterations (SAE, 2013).

Screen variations are also responsible for downstream flow instability. Baines and Peterson (1951) identified local differences between measured and expected downstream pressure and velocity profiles in low porosity screens ($\beta < 0.5$) (Laws & Livesey, 2003). They attributed these differences to be the result of randomly coalescing or diverging jet flows caused by small non-uniformities in the screen geometry. Bradshaw (1963) showed that interaction between jet flows results in vortices that persist for a significant length downstream and recommended that individual screen porosities not be lower than 0.57 (Laws & Livesey, 2003).

Oftentimes, a greater pressure drop is required which would necessitate the use of screens with a lower porosity than the recommended limit above. Bradshaw (1964) suggest that lower porosities may be achieved by overlaying multiple screens of higher porosity and Patel (1966) recommends that a deep-cell honeycomb located downstream could alleviate some of the unsteadiness (Laws & Livesey, 2003). Jackson (1972) extends his non-uniform model to multiple screen applications as well as combinations of screens and honeycomb

(Jackson, 1972). His model points to the fact that the flow quality of the downstream flow will depend on the quality of the most downstream screen.

1.5 Turbomachinery Aeromechanics

1.5.1 Overview

Flow-induced vibration in turbomachinery can be categorized as either synchronous or non-synchronous vibration, also sometimes referred to as integral and non-integral vibrations respectively (Heath & Imregun, 1998). Figure 1-11 illustrates a breakdown of flow induced vibrations; however, the exact terminology and even categorization of turbomachinery vibrations may vary among different authors.

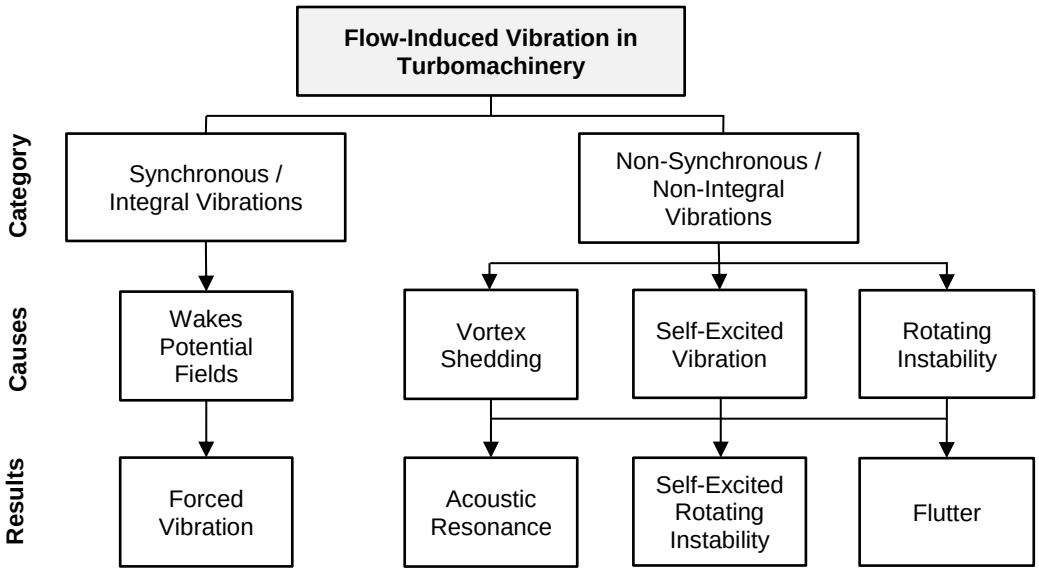

Figure 1-11. Categorization of Flow Induced Vibration

1.5.1.1 Synchronous Vibrations

Synchronous vibrations occur at frequencies which are integer multiples of the rotational frequency of the rotor, Ω, also referred to as engine order, EO. The synchronous excitation frequency, f_{sync}, can be defined by (Reinhardt et al., 1995)

$$f_{sync} = EO \times \Omega \tag{1.2}$$

The engine order is determined by the number of generated wakes upstream, by the potential fields of downstream vanes, and even the number of blades in adjacent compressor stages (Klauke et al., 2009). Therefore, a rotor blade will experience resonance when the non-uniform but periodic interaction with wakes and potential fields coincides with some integer multiple of its natural frequency (Holzinger et al., 2016). The amplitudes of synchronous vibrations are more severe at higher mass flow rates since it is a flow-induced force acting on the blades.

A common tool utilized by designers when considering synchronous vibrations is a Campbell diagram, shown in Figure 1-12. A Campbell diagram plots EO excitation lines and blade mode vibration curves as they vary with mechanical rotational speed. At every point where two lines intersect, there exists a risk of synchronous vibration (Hamed & Numbers, 1997). Typically, designers choose the design point to be in a region where no such risk is present, which is why synchronous vibrations are mainly of concern at off-design conditions (Logan & Roy, 2003; Thomassin, Vo, & Mureithi, 2011).

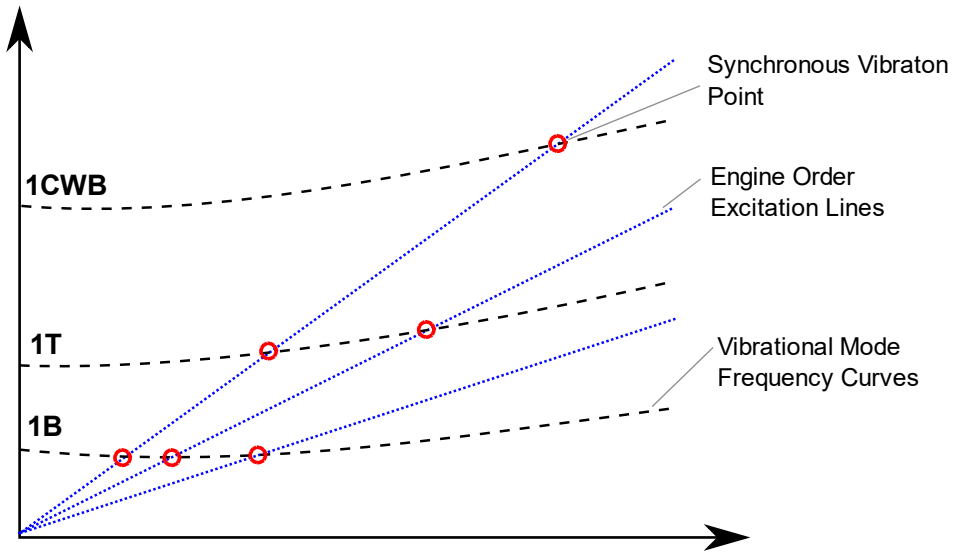

Figure 1-12. Sample Campbell Diagram

In addition to blade vibration, the entire blisk can also experience modes of vibration and the categorization of these modes is referred to by the nodal diameter (ND) pattern, which depends on the number of nodes occurring circumferentially in the mode shape. A source of difficulty for blade vibration measurement systems is identifying whether a synchronous vibration is due to a disk dominated mode, blade dominated mode, or a combination of the two (Klauke et al., 2009). Figure 1-13 and Figure 1-14 illustrate the differences between blade dominated vibratory modes and disk dominated modes from a modal finite element analysis (FEA) conducted in ANSYS Mechanical. The displacement plots illustrate areas of high displacement in red.

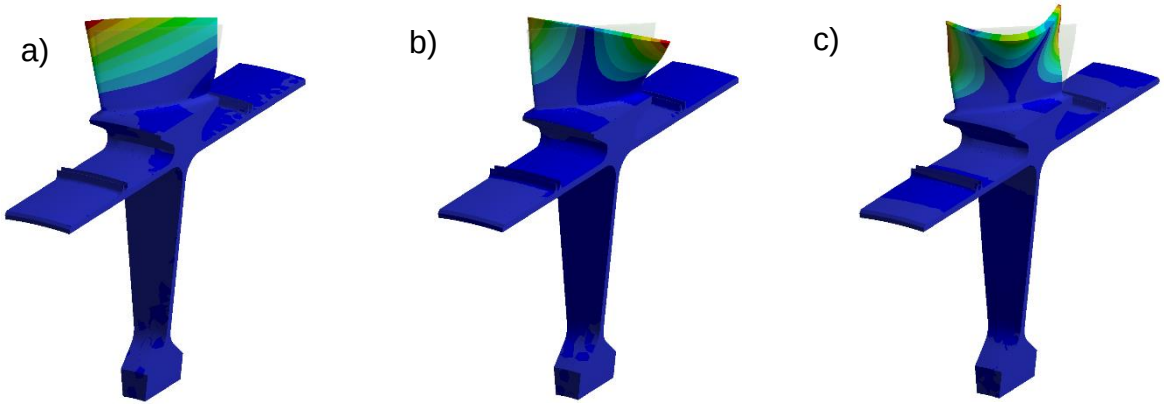

Figure 1-13. Blade Dominated Modes – a) 1st Bending, b) 1st Torsion, c) 1st Chordwise Bending

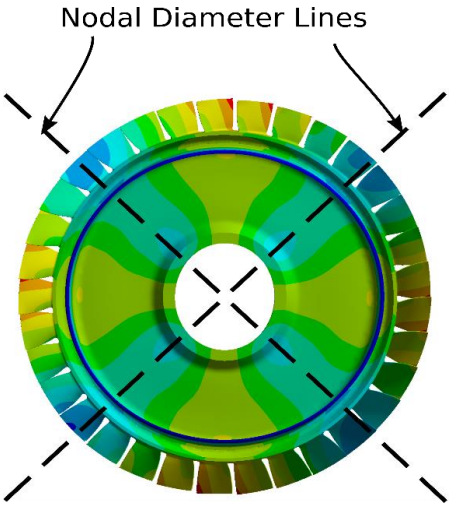

Figure 1-14. Disk Dominated Mode

Another important factor to consider when evaluating blade measurement techniques is the actual mode shape of the vibration, which is often a key factor in interpreting raw vibration data as well as in deciding the placement of the sensors. Typical blade vibration modes include bending or flap modes (B), torsion (T) and chord wise bending (CWB). The direction and location of maximum displacement depends on the type of mode in resonance, which is why knowledge of blade vibration mode shapes is typically a prerequisite for many measurement techniques (Lim et al., 2006).

1.5.1.2 Non-Synchronous Vibrations

Non-synchronous vibrations are not directly related to engine orders or the rotational speed, meaning that they can occur at any frequency. They are typically caused by aerodynamic instabilities, which through aeroelastic effects can develop into self-excited vibration. Additionally, the prediction of these vibrations is highly dependent on the quality of aeroelastic results, which are dependent on the fidelity of combined aerodynamic and structural models (Holzinger et al., 2016). As shown in Figure 1-2, non-synchronous vibrations can be divided according to the driving mechanism for the vibration which include vortex shedding, rotating instabilities and self-excited vibrations. Of these, vibration only occurs once the instabilities develop into self-excited vibration, most commonly referred to as flutter. As opposed to forced vibrations, self-excited vibrations are distinguished by the fact that the alternating force disappears once the motion of the blade ceases (Möller et al., 2017; Thomassin et al., 2011).

The instabilities responsible for non-synchronous vibrations have been studied since the early 1960's and remain a focus today. Rotating instabilities occur close to the aerodynamic stability limit of axial compressors, and therefore, designers have typically employed a conservative approach using high margins of safety when selecting the design point of compressors. If these instabilities can be reliably predicted and validated experimentally, then there is a potential to improve compressor efficiency by reducing safety factors applied to instability margins.

1.5.2 Blade Vibration Measurement Techniques

The need for accurate vibration measurement techniques on rotating blades arose in the early 1930's due to a large number of aircraft propeller failures which resulted in numerous aircraft losses and pilot deaths every year. Aircraft manufacturers sought to measure and properly understand rotor vibrations to redesign propellers so that they did not operate under severe resonant conditions (Russhard, 2015). As a result, strain gage technology was adapted to measure dynamic rotor vibrations and has been the industry standard for rotor vibration measurement ever since. With advances in computing and sensor technology in the past couple of decades, cheaper and more effective vibration measurement methods have been introduced, which address some of the many shortcomings of the conventional strain gage method.

Blade vibration measurement techniques can be divided into two categories: intrusive and non-intrusive. Strain gauge telemetry methods fall under intrusive measurements since they are attached directly to the blade while non-intrusive methods use sensors mounted in or around the casing which measure the vibration of the blades from a distance (Kadambi, Quinn, & Adams, 1989). Non-intrusive methods utilize a wide range of sensors such as optical, capacitive, inductive and magnetic. In summary, contact methods provide greater accuracy while non-intrusive methods provide more information without affecting either the flow or the structural damping characteristics (Heath & Imregun, 1998).

1.5.2.1 Strain Gages

Strain gauge transducers are affixed to the surface of interest and convert a change in strain to a change in resistance which can be measured, digitized and converted back into strain data (Beauseroy & Lengellé, 2007). The most common type of strain gauge is the bonded metallic foil. The strain experienced by the specimen is transferred directly to the strain in the foil gauge, which changes the electrical resistance.

Because strain gauges are mounted on rotating blades and the data acquisition system is in a stationary reference frame, excitation and signals between the strain gauge and external stationary hardware must be transmitted through either a slip ring or a wireless radio

telemetry system (Jones, 1996). Slip ring telemetry systems generate a significant amount of noise compared to the signal from the strain gauges, which results in a poor signal-to-noise ratio (SNR) (Di Maio & Ewins, 2012; Gwashavanhu, Oberholster, & Heyns, 2016). To compensate for the noise, most strain gauge telemetry systems typically use some sort of filter and/or pre-amplification of the signal prior to passing through the slip ring towards the data acquisition system. Alternatively, if the signal is not pre-amplified, the signal must be fed through an expensive post-processing filter to extract the original strain gauge signal. Oftentimes, the noise generated by the slip ring is so significant that the strain gauge signal cannot be accurately interpreted, especial for small amplitude deflections.

It is evident that strain gauge telemetry systems are fairly complex and require a lot of hardware and preparation, which can be very time consuming compared to other methods (Beauseroy & Lengellé, 2007). These systems often require short interval maintenance, and components such as the slip rings have high failure rates and very short lifespans, especially in the harsh environments experienced in turbomachinery (Heath & Imregun, 1998; Kadambi et al., 1989; Procházka & Vaněk, 2011). Furthermore, because most of the components are located on the rotating side of the assembly, any maintenance or troubleshooting usually requires an extensive disassembly of the machine which can result in significant additional costs and delays for a testing program (Beauseroy & Lengellé, 2007). Due to their short life in turbomachinery applications, strain gauge telemetry systems have not had much success as in-service blade health monitoring systems (Dreier, Gunther, Pfister, Czarske, & Fischer, 2013).

The intrusive nature of strain gauges, combined with a limited number of blades that can be simultaneously monitored, makes them a very unattractive option for many researchers. For strain gauges to capture a particular vibratory response, gauges must be small in comparison to the blade and must be attached in the proper location and orientation, as determined from an FEA analysis (Heath & Imregun, 1998). As previously mentioned, blisk vibrational modes can be significantly more complicated than traditional rotors. Therefore, strain gauges placed on a select number of blades provide a very poor resolution of the complex vibratory modes experienced by a blisk (Heath & Imregun, 1998).

Despite the many drawbacks, strain gauge telemetry systems are still used for research due to the accuracy of the measurements they provide, which can be used as a benchmark for calibration of alternative measurement techniques (Kadambi et al., 1989). Furthermore, they are the only method which can directly measure the stress experienced by the structure.

1.5.2.2 Blade Tip Timing

Blade tip timing methods are a category of non-intrusive measurements which determine the vibrational characteristics using blade tip sensors mounted around the casing (Jones, 1996). Tip timing systems are also commonly referred to as Nonintrusive Stress Measurement Systems (NSMS), Arrival Time Analysis (ATA) or Blade Vibration Measurement (BVM) in literature. The main components of a typical tip timing system are a time reference sensor typically mounted near the shaft, blade tip sensors mounted around the casing, and the data acquisition system (Beauseroy & Lengellé, 2007; Jones, 1996).

As the names suggest, the fundamental principle of the method is that vibration properties can be deduced from the difference between the expected and actual arrival times of the blades at each sensor location. The expected, or theoretical, arrival time refers to the time at which the tip of a particular blade would pass each sensor in the absence of any structural vibration. A blade tip's location at any time can be calculated based on knowledge of time, rotational speed, sensor location, and the blade's position relative to a reference blade. Under real conditions, the blade will be vibrating causing the arrival time to be slightly sooner or later than the expected arrival time at each sensor location (Beauseroy & Lengellé, 2007).

This principle is better illustrated visually in Figure 1-15 which shows a typical sensor signal for a single blade only. The upper figure shows the expected signal of an idealized non-vibrating blade, and the bottom shows a realistic signal from a blade experiencing vibration, where the time between successive pulses is not uniform. By overlaying the two plots, the difference between expected and actual arrival time can be determined for each

blade passage event. A tip timing system does this for every single blade at each sensor location.

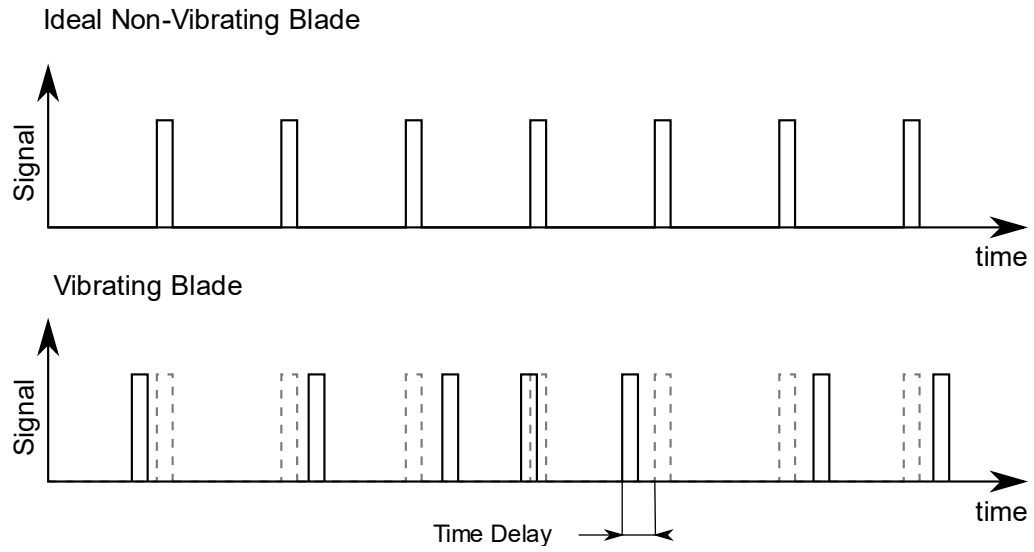

Figure 1-15. Blade Tip Timing Sensor Signal Output Sample

In summary, blade tip timing systems are cheaper, simpler to implement, monitor all blades as opposed to just a few, and most importantly, do not alter the flow or structural stiffness properties of the blades. This makes them a more attractive option for research and blade health monitoring systems versus the conventional strain gauge technique (Dimitriadis, Carrington, Wright, & Cooper, 2002). Although the system is simple and fairly reliable, converting the raw signal into blade vibration data is significantly more challenging than conventional strain gauge methods, and the circumferential measurements may not capture effects due to circular non-uniformity.

Interpreting non-synchronous data is usually a straightforward process requiring only a small number of probes. For synchronous vibrations, the vibration frequency occurs at integer multiples of rotational frequency, and a single probe will always detect the same deflection amplitude. This does not provide enough information to deduce any vibration properties, and therefore, additional sensors mounted at uneven intervals around the casing

are required. Interpretation of the signal is further complicated by the effects of mistuning, disk-blade mode coupling, excitation at multiple engine orders, and the potential for synchronous and non-synchronous vibrations occurring simultaneously (Dimitriadis et al., 2002). Therefore, tip timing analysis methods continue to be an active area of interest and are oftentimes proprietary. Finally, unlike strain gauge data, tip timing data cannot be directly converted to blade stress. The accuracy of the stress predictions relies not only on the accuracy of the deflection amplitude measurement but also on the correlation of the deflection to a blade stress using either finite element analysis or strain gauge correlations. For this reason, it is common that strain gage data are still necessary to supplement or calibrate NSMS data for an engine test program.

1.6 Research Objectives

The primary focus of this work is surrounding the experimental study of an inlet total pressure distortion in a multi-stage axial compressor environment. The majority of studies found in open literature have looked at inlet distortion from the perspective of the entire gas turbine engine and the effect on overall performance and stability. Few studies to date have concentrated on characterizing, in detail, the inter-stage propagation and attenuation of a total pressure distortion in an axial compressor. The Purdue 3-Stage Axial Compressor Research facility (P3S) provides a multi-stage environment equipped with inter-stage instrumentation capabilities that permit detailed total pressure field characterization with a high level of spatial resolution.

This research is divided into two parts. The first part focuses on the design and implementation of a circumferentially traversable inlet total pressure distortion generation system. The inlet distortion is generated by a series of low porosity wire gauze screens located in the inlet duct upstream of the P3S compressor. The second part of this study focuses on the demonstration of data acquisition methods of high resolution inter-stage total pressure field characterization. An iterative method was used to select a suitable distortion screen and detailed total pressure and turbulence intensity measurements at the compressor inlet were performed to define the boundary conditions necessary for future computational models. Using the inter-stage total pressure rakes, along with a series of

coordinated vane and distortion traverses, the total pressure field downstream of each stage was captured to study the attenuation and propagation of the total pressure distortion from compressor inlet to exit.

The objective of this work to twofold: first, to establish and validate a flexible testbed for studying total pressure distortions with a high degree of circumferential resolution, and second, to provide an experimental dataset consisting of flow measurements characterizing the propagation and attenuation of a total pressure distortion in a multi-stage axial compressor. This dataset is intended to support the development and validation of novel computational tools aimed at modelling the flow physics inside gas turbine compression systems subjected to a total pressure distortion. Currently, such models are very computationally expensive and impractical to utilize during early design stages. However, advancements in computational power as well as decreasing cost has spawned an increased effort to develop high fidelity computational models for turbomachinery flow analysis and this study is meant to support these efforts.

The second aspect of this study was to document efforts surrounding the integration of a strain gage telemetry system. Two proposals from two suppliers were presented; an electromechanical slip ring and a wireless telemetry system. The motivation for this proposal was to supplement and validate forced response data on the embedded rotor in the P3S research compressor. The data was previously acquired by a past student using Non-Intrusive Stress Measurement System (NSMS) as part of GUIde V research efforts. The activity and discussions surrounding this project are documented in this work to aid future investigators who may resume efforts acquire a strain gage telemetry system.

CHAPTER 2. FACILITY AND EXPERIMENTAL METHODS

2.1 Overview

This chapter presents an overview of the experimental compressor research facility used for this study including discussion of functionality, hardware, instrumentation, and data acquisition methods. The PAX-1100 research compressor is introduced and discussed along with a detailed discussion on the design of the inlet distortion traverse hardware and distortion screens. Finally, the experimental methods and data processing techniques for the inlet distortion study are discussed in detail.

2.2 Purdue 3-Stage Axial Compressor Research Facility

2.2.1 Facility Overview

The research presented in this work was performed at Purdue University's High-Speed Compressor Lab located at Maurice J. Zucrow Laboratories. The inlet distortion hardware was adapted to the open-loop Purdue 3-Stage Axial Compressor Research facility (P3S) shown in Figure 2-1. The compressor test section is driven by a 1400HP AC induction motor from ABB which is controlled by a liquid-cooled variable frequency drive (VFD). A magnetic encoder located on the motor shaft provides feedback to maintain shaft speed to within 0.01% of the desired speed. The motor shaft drives a 29:133 (approximately 1:4.6) speed increasing gearbox to attain a nominal design shaft speed of 5000 RPM for the compressor utilized in this study. The gearbox oil is passively cooled using an external heat exchanger. Following the gearbox, the compressor driveline consists of two flex couplings flanking a Honeywell torque meter (model 1805-10K) followed a spline joint mating to the compressor shaft. A laser encoder mounted above the output shaft of the gearbox generates a once-per-rev signal that provides a highly accurate compressor shaft speed necessary for many high-frequency measurements.

Atmospheric air is drawn from outside the facility through an 8ft diameter screen into a 20ft long settling chamber. The settling chamber alleviates atmospheric variations resulting

from cross-winds. Details on the design and analysis of the inlet settling chamber can found in (Ball, 2013). Air passes through two MERV 8 standard filters: one spanning the diameter of the settling chamber and the other spanning the bellmouth. Immediately downstream of the bellmouth, an aluminum honeycomb screen used for flow conditioning followed by an ASME standard (PTC-19.5) long-form venturi that provides compressor mass flow rate measurements. The inlet flow travels approximately 40ft, or 20 duct diameters, between the bellmouth and compressor test section. A removable 4ft pipe section is located approximately 10ft upstream of the compressor face where inlet flow conditioning hardware, such as the inlet distortion traverse used in this study, can be mounted.

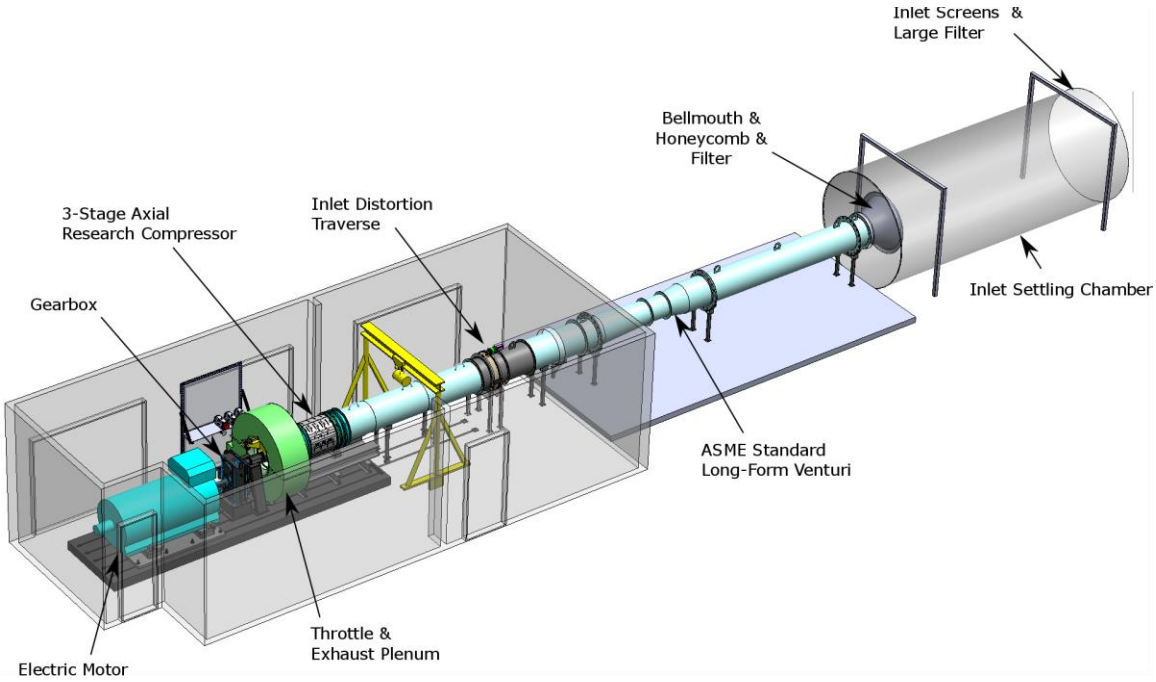

Figure 2-1. Purdue 3-Stage Axial Research Compressor Research Facility

An elliptical nosecone gradually transitions the inlet duct flow to a 2in annular area with 24in outer diameter as shown in a cutaway view in Figure 2-2. Following the compressor test section, the flow exhausts into a large cylindrical scroll collector which directs the flow outside the facility. The exhaust flow is throttled via a sliding ring which constricts the area of the flow as it enters the collector. An electromechanical actuator located outside of the collector translates the throttle ring along two linear guides. The facility also features a

back-up throttle by-pass system that allows unloading of the compressor in the event of a throttle system malfunction. Three pneumatically actuated ball valves can be opened to vent air through a secondary flow path upstream of the throttle ring. Additional discussion on facility layout and systems can be found in (Talalayev, 2011) and (Ball, 2013).

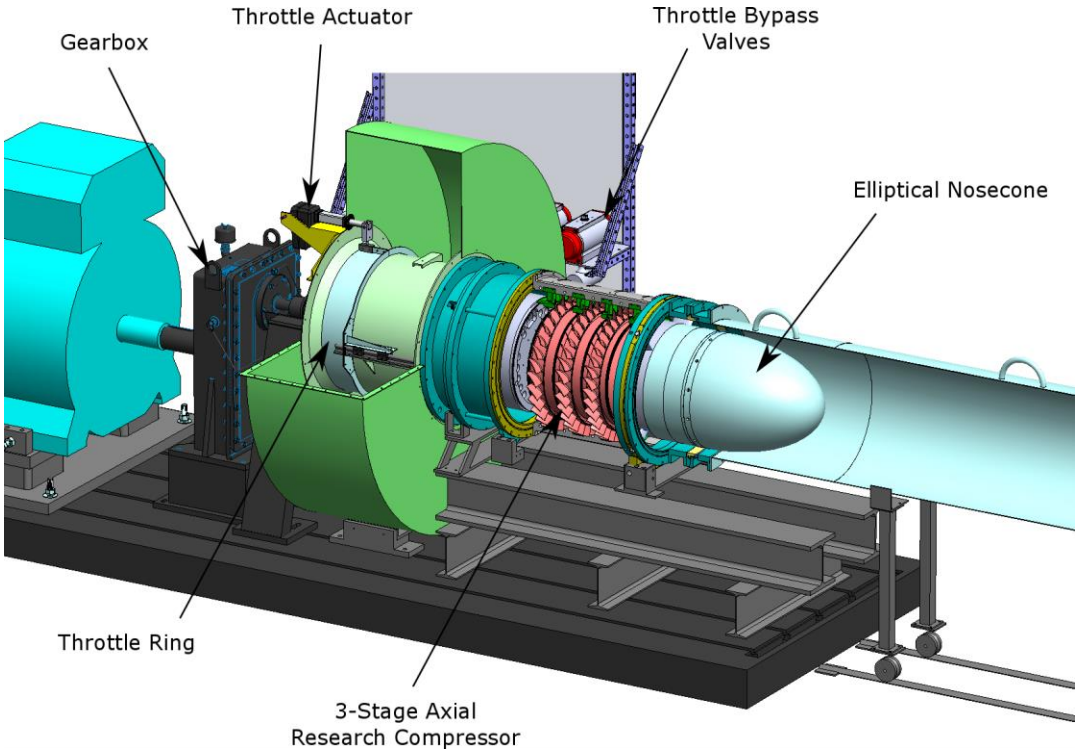

Figure 2-2. Cutaway View of 3-Stage Axial Compressor Research Facility

2.2.2 PAX100 Research Compressor Test Section

The Purdue 3-Stage (P3S) Axial Compressor Facility was designed to accommodate multiple research compressor configurations. The research presented in this work was conducted on the PAX100 research compressor, whose geometry models the rear stages of a Rolls Royce production turbofan engine's high-pressure compressor (HPC). The stages are geometrically scaled up to facilitate increased detail in flow measurements and are operated at engine-representative Reynolds and Mach numbers to replicate real engine flow physics. The capability to perform detailed flow measurements and aeromechanics studies

on high speed multi-stage compressors makes this facility applicable to high Technology Readiness Level (TRL) validation studies.

The flow path of the PAX100 3-stage compressor is shown in Figure 2-3. It consists of an IGV followed by three stages comprising of rotor and stator pairs all machined from 17-4 stainless steel. The PAX100 compressor has a constant 2in height annulus with a 2ft outer diameter. The rotors and IGV are standard double circular arc design and the stators are NACA 65-series airfoils. The rotor drum is comprised of three individual blade integrated disks (blisks) which are compressed together using two endplates mounted to the shaft. The IGV and stators are shrouded both at the hub and tip, and each consist of two equal segments held together when installed in the compressor casing. The IGV and stators are all independently circumferentially traversable for approximately two stator passages, allowing for pitch-wise data to be captured by the stationary rakes. The vanes are rotated via a pair of electromechanical actuators located external to the casing and positional feedback is obtained from string pot potentiometers.

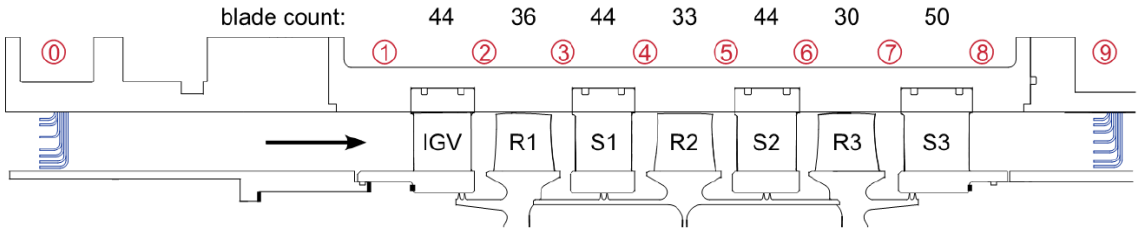

Figure 2-3. PAX100 Compressor Flow Path Cross Section and Axial Location of Instrumentation Stations

The compressor casing halves are machined from 6061 Aluminum and feature a wide assortment of instrumentation ports located before and after all blade rows as indicated by stations 1 through 8 in Figure 2-3. Station 0 marks the location of the AIP while station 9 is the exit rake location. The AIP has circumferentially distributed instrumentation ports that permit multiple rakes to be installed. Furthermore, the casing features six over-rotor multipurpose windows, two per rotor, that can be outfitted, for example, with specialized high frequency pressure transducers or quartz glass windows for laser studies.

2.2.3 Steady Compressor Performance Measurement and Instrumentation

The operating point of a compressor defines the location on a compressor map illustrated in Figure 1-8. By changing the rotational speed and mass flow rate, the performance, characterized by the total pressure ratio (TPR), is altered. The rotational speed and mass flow rate are typically corrected to standard day conditions to account for varying inlet conditions caused by changes in ambient temperature, pressure, or humidity. Doing so assures consistency in performance measurements obtained regardless of inlet conditions and facilitates a fair comparison with other experimental or computational data. Classical correction factors for speed and mass flow rate found in many turbomachinery textbooks account only for variations in temperature and pressure, thus, assuming a thermally and calorically perfect gas.

The Purdue 3-stage compressor facility is open-loop and is subjected to large fluctuations in humidity between seasons that can lead to errors if humidity effects are ignored. Correction for humidity for this study is implemented as per the methods outlined in (Berdanier, Smith, Fabian, & Key, 2015). In summary, the alternate formulation of correction factors utilizes the stagnation speed of sound, a_0, and stagnation density, ρ_0, instead of the stagnation temperature and pressure used in classical correction factors. The corrected mass flow rate, $\dot{m}_c$, is calculated via

$$\dot{m}_c = \dot{m}_{act}\left(\frac{\rho_{0,ref}}{\rho_{0,act}}\frac{a_{0,ref}}{a_{0,act}}\right) \tag{2.1}$$

where $\dot{m}_{act}$ is the actual mass flow rate, and the corrected speed, N_c, is calculated via

$$N_c = N_{mech}\left(\frac{a_{o,ref}}{a_{o,act}}\right). \tag{2.2}$$

The actual shaft speed is measured via the optical encoder discussed earlier and the actual mass flow rate is calculated using the differential pressure measurements across the venturi. The differential static pressures at the venturi are measured using two Rosemount 3051C high-accuracy pressure transmitters. Each transmitter is calibrated to a different pressure

range to ensure sufficient range (0-8 inH_2O) and low uncertainty near nominal loading (0-5 inH_2O). A pitot-static probe with an integrated T-type thermocouple is positioned upstream of the venturi and used to calculate local thermodynamic properties necessary for mass flow rate calculation.

This study uses the conditions measured at the AIP (station 0) to compute the correction factors outlined above. Seven-element Kiel-head total pressure and total temperature rakes are located at the AIP. The readings of the middle elements, located at 50% span, are used to approximate the bulk inlet flow conditions. The static pressure at the AIP is measured at 13 circumferential locations and averaged. An Omega HX94 Thermo-Hygrometer is installed near the bellmouth inlet and provides humidity readings with an uncertainty of ±2%. A thermodynamic equation program, REFPROP (Lemmon et al., 2013), is used to calculated stagnation conditions necessary for the correction factors outlined above. The corrected operating point is calculated on-the-fly and is verified prior to collecting data.

Instrumentation ports located in the casing provide the capability to capture flow measurements before and after each blade row. Static pressure ports are located at four circumferential locations at stations 1 through 8 and a single one at station 9. Additional seven-element Kiel-head total pressure and total temperature rakes are located at stations 1 through 9. The manufacturer, Aerodyn Engineering, quotes a recovery factor for the total pressure and temperature rakes of one, with three significant digits. The rakes have a quoted angular acceptance range of ±30° and are aligned with the representative mean absolute flow angle.

The inlet distortion standards document, ARP-1420, recommends that rake elements be distributed radially at the centroids of equal areas to simplify the area-averaging procedure (SAE, 2011). The rakes utilized in the PAX100 compressor, however, have radial probes which are biased towards the hub and tip to provide increased resolution in regions where secondary flows and boundary layers are more significant. This radial distribution is also better suited to capture the flow profile variations which readily lends itself to comparison

with CFD results. The radial distribution of probes and their associated area average multipliers are summarized in Table 2-1 for the rakes used in this investigation.

Table 2-1. Instrumentation Rake Radial Distribution and Area Average Multipliers

Probe	% Span	P_0 Station 0 Multiplier	% Span	P_0 Station 1-8 T_0 Station 0-9 Multiplier	% Span	P_0 Station 9 Multiplier
7 – Tip	88	0.172	88	0.172	88	0.172
6	80	0.147	80	0.095	80	0.121
5	60	0.204	70	0.155	65	0.154
4	40	0.148	50	0.200	50	0.150
3	30	0.096	35	0.145	35	0.146
2	20	0.085	20	0.085	20	0.109
1 - Hub	12	0.148	12	0.148	12	0.148

The rake locations indicated in Table 2-1 are typical for studies looking at inter-stage performance. Rakes from stations 1-8 will be utilized for AIP flow field characterization since they all have the same radial distribution. Figure 2-4 shows how the area sectors associated with each of the 7 probes on the kiel-head rakes. The boundary of each sector is located at the midpoint between each probe, or the hub and shroud for the first and last elements.

Although there is no physical foundation for area averaging of stagnation properties, ARP-1420 recommends that this method be utilized for inlet distortion studies. Cumpsty & Horlock, (2005), compared many flow averaging techniques for turbomachinery applications. They concluded that practical considerations for flow measurements conducted in turbomachinery typically necessitate the use of the area-averaging method. They also demonstrated that for most turbomachinery flows, the area-averaging method will agree remarkably well with other methods such as mass-, thrust-, or work-averaging. The area-averaging method is to be avoided only when characterizing flow where a large part of the cross-sectional area is occupied by separated flow.

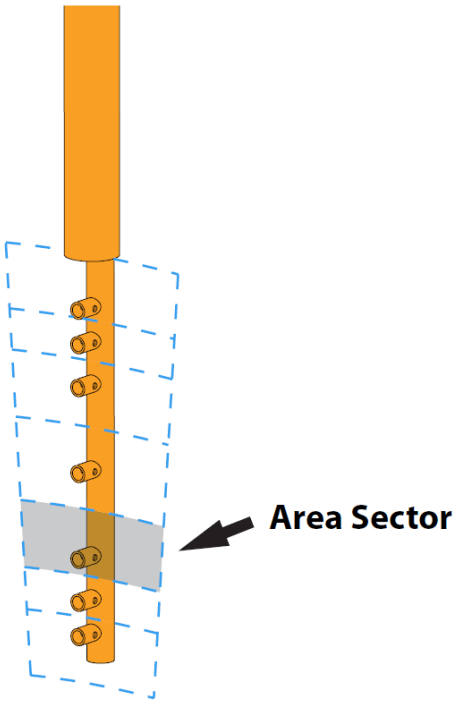

Figure 2-4. Kiel-Head Rake Area Sector Discretization (Talalayev, 2011)

Total and static pressure measurements are obtained using Scanivalve 3016 and 3217 Digital Sensor Arrays (DSA) pressure scanner modules. Each DSA contains 16 temperature-compensated piezo-resistive pressure sensors. The modules are rated for different gage pressure ranges to accommodate the wide range of pressures measured within the compressor. These include 1psid, 2.5psid, 5psid, and 15psid with full-scale accuracy ratings of 0.12%, 0.12%, 0.05%, and 0.05%, respectively. Atmospheric reference pressure is measured separately using a high-accuracy Setra 270 barometric pressure sensor that is rated for a range of 800-1100mbar with a full-scale accuracy of 0.03%. The reference pressure is measured from within a small sealed cylindrical enclosure to eliminate pressure fluctuations which could result from, for example, a suddenly open door to the facility or the air-conditioning turning on. To account for thermal drift effects, the DSAs are quick-zeroed prior to commencing an AIP traverse and approximately every 20 minutes thereafter to recalibrate the zero offset.

T-type thermocouples are used for total and static temperature measurements which are read by a Keysight Technologies (formerly Agilent) 35980A Multifunction Switch/Measure Unit equipped with 34921A 40 channel multiplexer with low thermal offset paired with 34921T terminal blocks. A liquid calibration bath performed by (Berdanier, 2015) demonstrated an overall conservative uncertainty of less than 0.45°F / 0.25°C and repeatability being an order of magnitude less. Thermocouple voltage measurements are integrated over five power line cycles and each temperature datum is obtained by taking the arithmetic mean of five independent measurements.

2.3 Inlet Distortion Traverse Hardware

2.3.1 Traverse Assembly

The purpose of the inlet distortion traverse hardware is to provide a rotatable section in the compressor inlet duct to which an inlet distortion screen may be mounted. As previously discussed, the PAX100 instrumentation is affixed to the casing. Therefore, the distortion screen traverse is designed to rotate the distortion screen relative to the instrumentation. A full 360° extent of circumferential data can be obtained with as little as one probe located at the AIP. Furthermore, by rotating the distortion, fewer rakes are required to measure conditions at the AIP which reduces blockage and instrumentation costs. The circumferential resolution of data obtained in the compressor is limited only by capabilities of the rotational system and the width of the probes. Consideration must also be given to testing time when selecting the traverse resolution. The smaller the increment, the longer will be the data acquisition time. Data acquisition and control of the hardware is integrated in LabVIEW to permit automation to reduce operator workload and facility operation time.

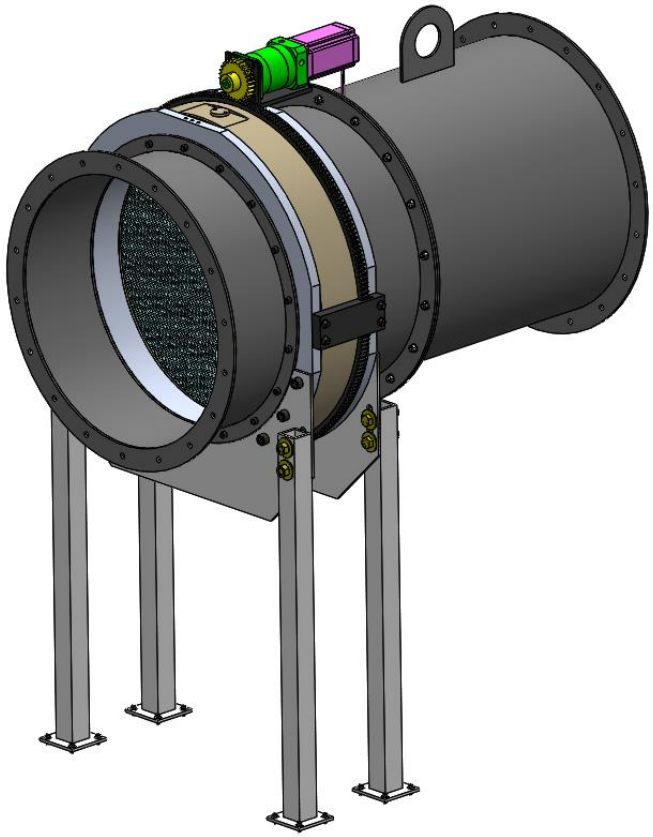

Figure 2-5. CAD View of Inlet Distortion Traverse Assembly

Figure 2-5 shows a CAD view of the inlet distortion traverse assembly. The assembly consists of a 3-piece circular duct section to interface with the existing inlet ducting. Four steel legs are secured directly to the test cell concrete floor and support the weight of the traverse assembly. The design of the traverse section is further illustrated in the section view shown in Figure 2-6. The traverse consists of a rotational nylon screen holder which is sandwiched between two aluminum flange sections. The nylon screen holder is designed to slide along smooth ridges machined into aluminum halves while two O-rings are used to seal the assembly and prevent leakage. Rubber gaskets are used at all pipe flange interfaces to minimize leakage.

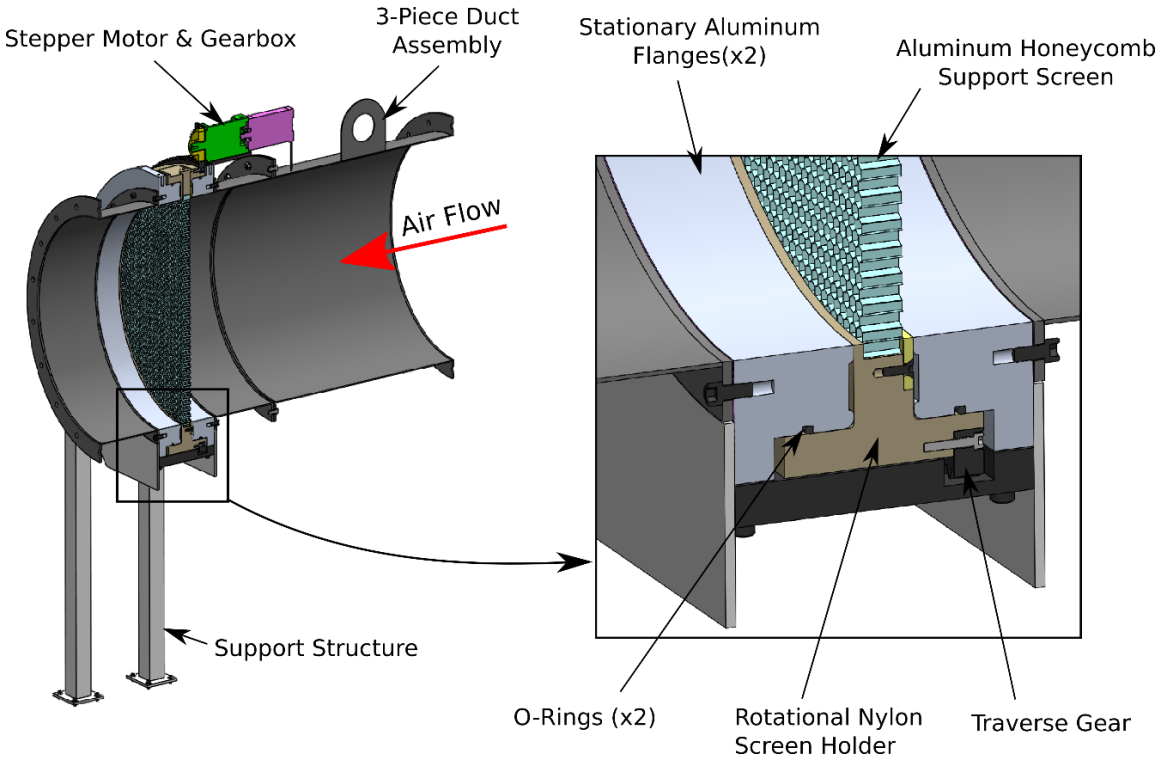

Figure 2-6. Cutaway View of the Inlet Distortion Traverse Assembly

A large gear is secured to the outer diameter of the rotational nylon screen holder and is driven by an Anaheim Automation stepper motor (Model 34Y207S-LW8) and gearbox (Model GBPH-0902-NS-020-AA341-500). The gearbox is secured to a steel support bracket mounted to one of the aluminum halves. The stepper motor has a step angle of 1.8° and is connected to a 20:1 reduction gearbox. The stepper motor permits precise positional control of the traverse since it rotates in fixed angular increments. Although the stepper motor is installed in an open-loop configuration, it has been oversized to assure that its torque capability exceeds the expected loading. In doing so, the likelihood of skipping a step (stalling) is reduced, and hence, the position of the motor can be accurately deduced by keeping track of the number of step commands sent to the motor.

The stepper motor is controlled by an Anaheim Automation Programmable Controller (Model DPLMLA601). LabVIEW 2016 is used to send commands to the controller via the RS485 protocol. The controller is connected to the computer using a B&B Electronics

RS485-to-USB adapter (Model 485USBTB-2W). The power supplied to the controller is first filtered to remove noise using a CORCOM power filter (Model 10EMC1). The stepper motor is connected in an 8-lead bipolar (Series) connection using a 16AWG 4-line shielded cable. Figure 2-7 shows a picture of the motor control hardware mounted to a panel. A detailed wiring diagram is included in Figure 2-8.

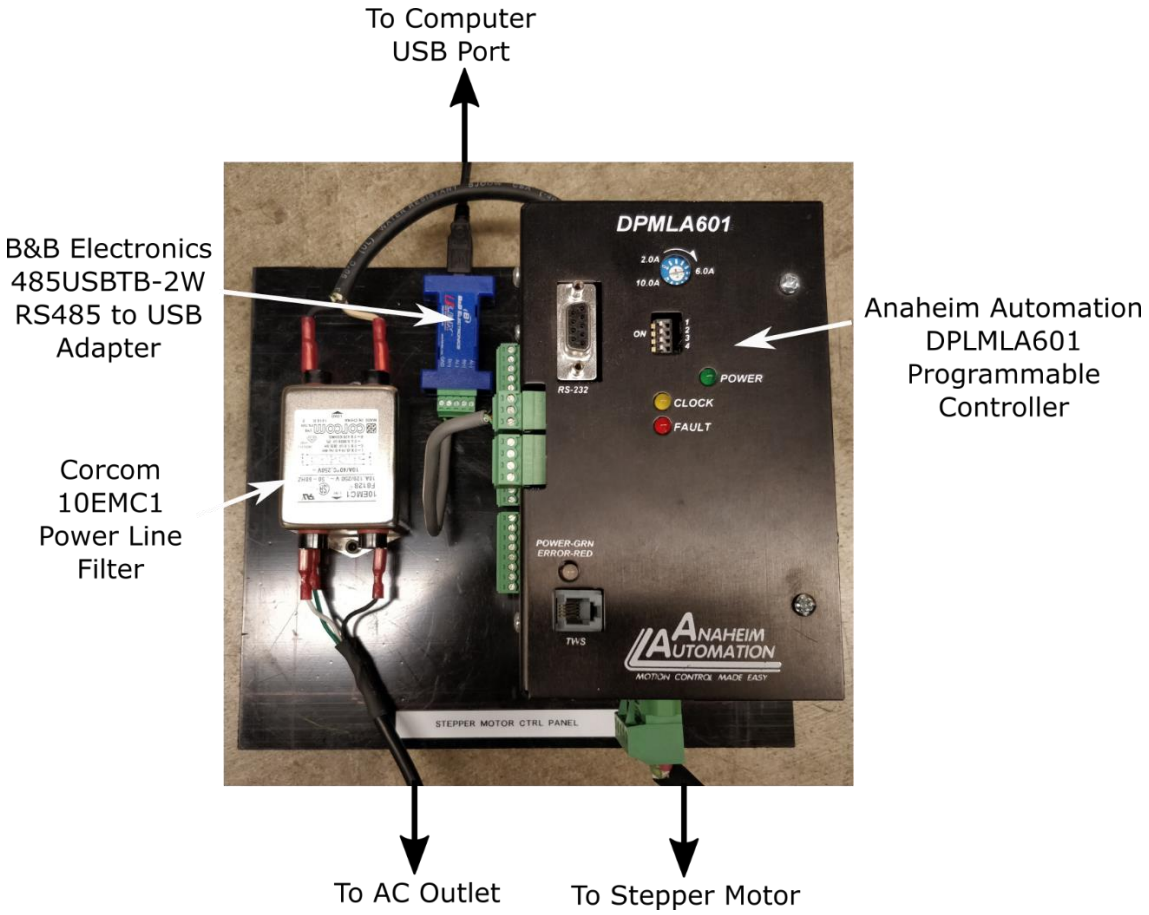

Figure 2-7. Stepper Motor Control Hardware

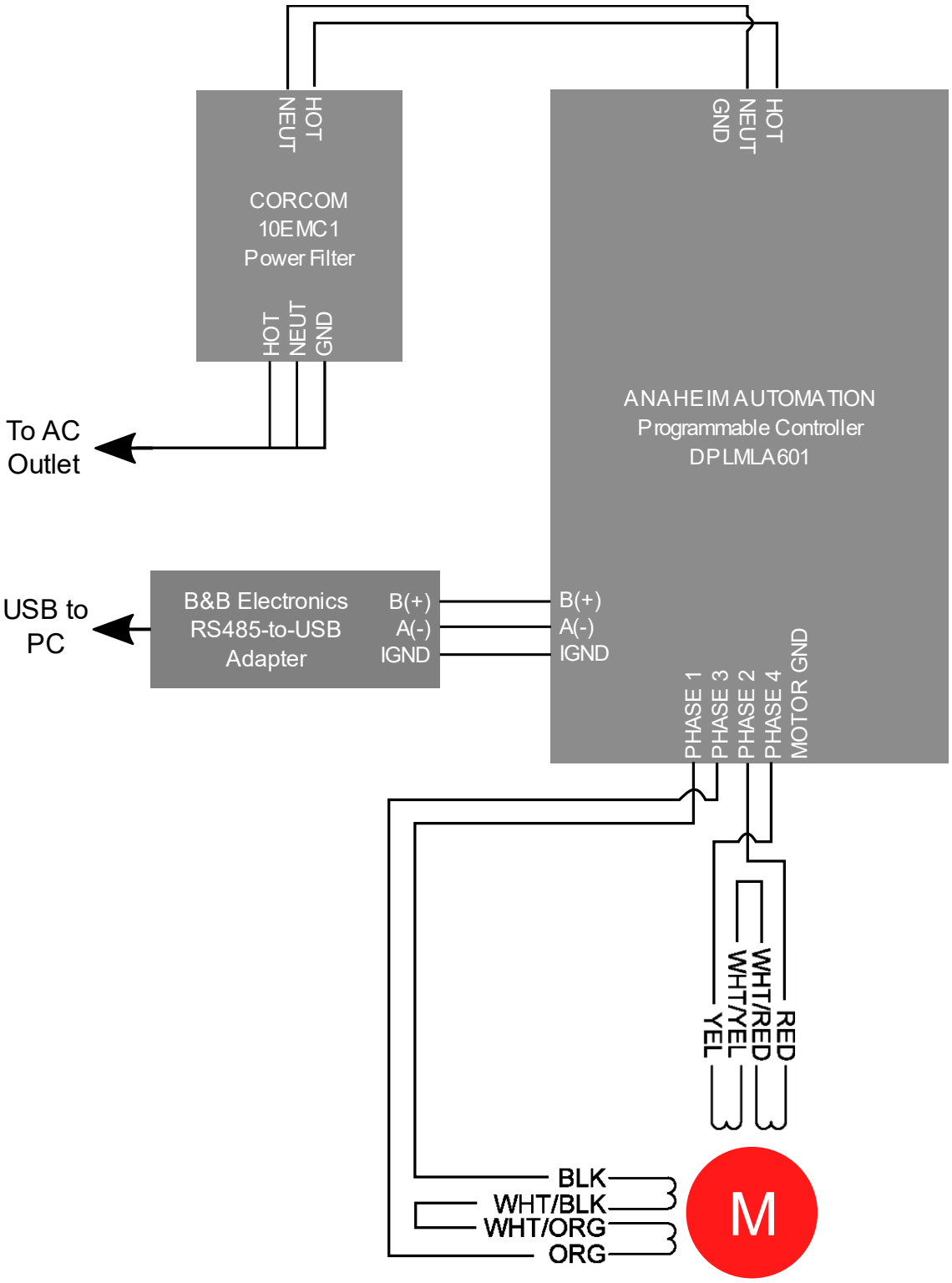

Figure 2-8. Stepper Motor Hardware Wiring Diagram

A test cell camera allows operators to visually verify the position of the traverse by using visual reference to external degree markings on the rotational section. Following a complete traverse, the top dead center (TDC) position should return to its initial position. A deviation in this final position indicates to the operator that the motor had stalled at some point during the traverse, and therefore, the expected motor position was inaccurate. The motor can be commanded to perform an automatic traverse, or, manually commanded to move by any degree increment to within 0.01° accuracy. As mentioned, the stepper motor does not have any absolute reference, and therefore, TDC is established manually by the operator. This is done by commanding the traverse to TDC prior to commencing a traverse and verifying its position using visual reference to external degree markings.

An Aluminum honeycomb screen is used as a structural support for the distortion-generating screens. The honeycomb is cut to an outer diameter that is ¾in. larger in diameter than the inlet ducting, and it sits recessed within a circumferential trench machined into the inner diameter of the rotational nylon screen holder. The honeycomb is held clamped into this recessed trench during assembly by a nylon filler ring section, shown in yellow in Figure 2-6. The aluminum halves, rotational screen holder, honeycomb, and filler ring are all stacked together during assembly, as shown in Figure 2-9. The entire assembly is held together by three steel clamps which bolt into the two aluminum halves. This stacking design minimizes the chance that the honeycomb screen could move downstream towards the compressor in the event that it become structurally compromised. Furthermore, the absence of a protrusion or ridge on the circumference of the honeycomb carrier assures a clean boundary that does not introduce blockage or disrupt the boundary layer flow.

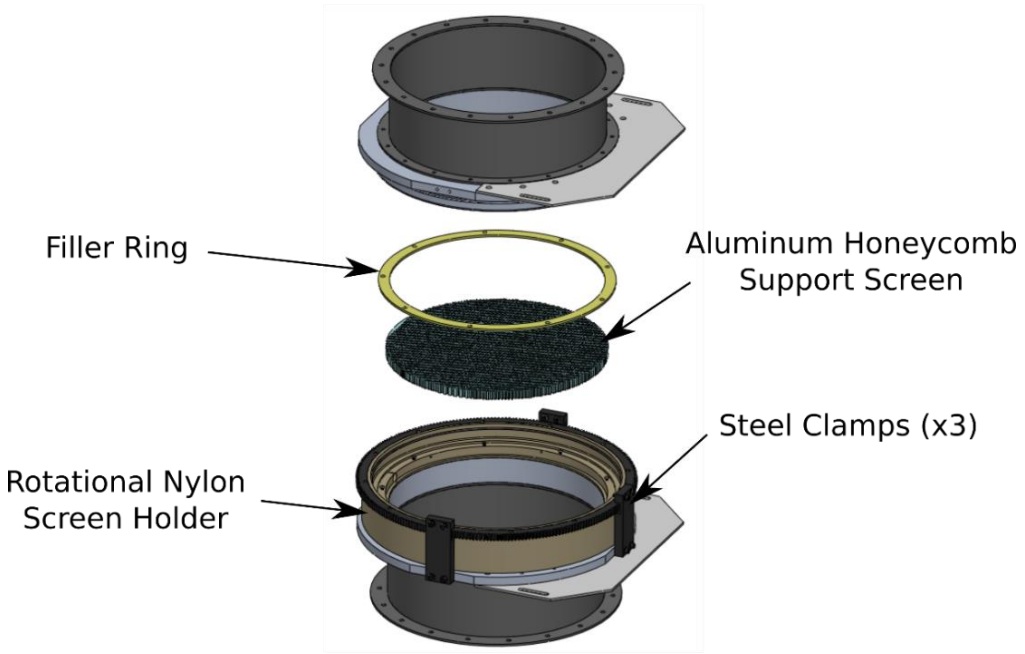

Figure 2-9. Installation of Honeycomb Support into Rotational Traverse

2.3.2 Distortion Screen Mounting Support

The total pressure distortion in this investigation is achieved using fine wire gauze screens. These screens are made of small gage wires interweaved to form a mesh which has very little structural rigidity. Since they cannot hold their shape or withstand loads imparted by the passing air, the distortion generating screens are secured to a more rigid honeycomb support screen or carrier. The screens are pre-cut to the required shape and size and are secured to the upstream face of the honeycomb support screen using three long size 8 fasteners. The fasteners pass through the honeycomb and gently apply pressure via two washers to clamp the screen to the honeycomb. An alternative mounting strategy using safety wire was also tested, however, the safety wire was found to damage the aluminum cells and was, therefore, abandoned.

Figure 2-10 shows a scale drawing of a distortion generating wire gauze screen attached to the honeycomb support screen. The flow passing through the honeycomb is considered to be clean, undistorted flow, while the flow passing through the gauze screen is distorted. In

reality, some total pressure loss also occurs across the honeycomb due mainly to skin friction.

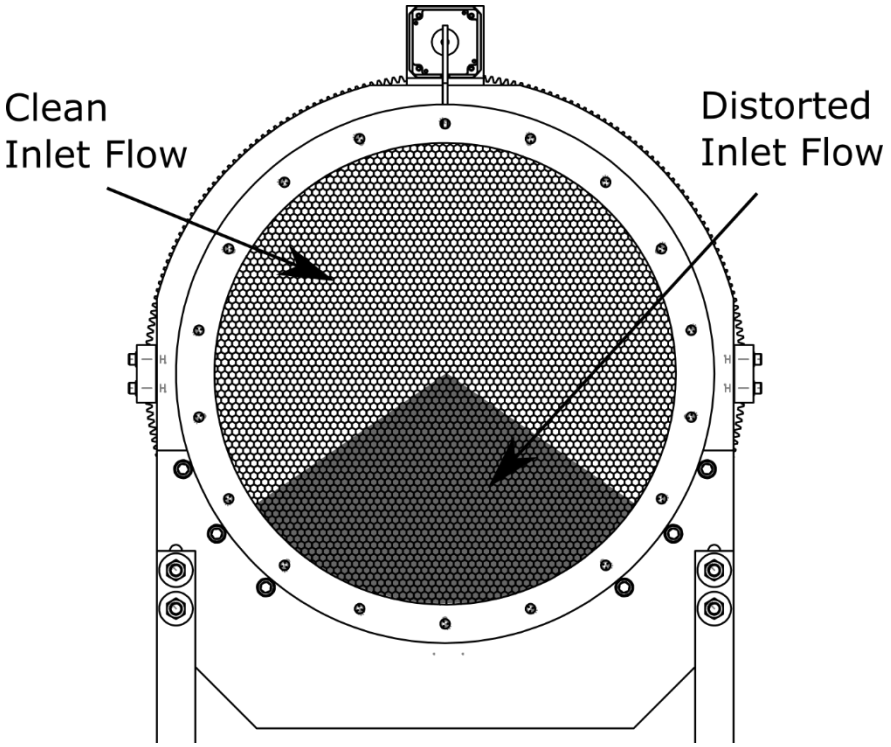

Figure 2-10. View of Wire Gauze Screen Attached to Honeycomb Support

As discussed in Chapter 1, the conventional approach has been to utilize a thicker gage wire screen as a support structure to which finer gage lower porosity screens are then secured. However, these support screens introduce additional pressure loss and increase the unsteadiness in the downstream flow due to inter-weaving of the thicker gage wire. In lieu of a conventional wire support screen, the carrier in this study is selected to be a 1" thick, 3/8" cell width honeycomb disk with a 0.003" foil thickness provided by Plascore (Model PCGA-XR2-3.6-3/8-30-N-3003). The honeycomb sheet is waterjet cut into a disk of the required diameter.

Honeycomb is typically utilized as a flow straightener with minimal pressure drop. In this application, the selected honeycomb contributes a blockage of less than 2% by area. This configuration does not contribute much to flow straightening since it has a relatively low

cell depth-to-width ratio of 2.7 whereas typical flow straighteners require much longer channels. However, an advantage to using honeycomb is that it introduces minimal unsteadiness and helps establish more uniform flow downstream of the distortion screens.

2.3.3 Integration to Research Facility

The inlet distortion traverse assembly is installed approximately 5.5 pipe diameters (L/D), or 11ft, upstream of the aerodynamic interface plane, as shown in Figure 2-12. The 3-piece duct of the traverse assembly was sized to fit in the place of an existing 4ft removable duct section located upstream of a 10ft inlet duct. The AIP for this study is selected at the existing instrumentation station 0 (previously described in Figure 2-3 and illustrated in Figure 2-12). Station 0 is located in the constant annular section immediately following the elliptical nosecone and upstream of the front bulkhead struts. It is approximately 6 blade chords upstream of the IGV. This selection is consistent with past GUIde studies conducted on the PAX100 compressor and satisfies the recommendations of ARP-1420 discussed previously in Chapter 1. Furthermore, station 0 features a variety of circumferentially distributed instrumentation ports which can be outfitted with up to 8 identical pressure and temperature probes to reduce data acquisition time for an AIP traverse.

Recall from Chapter 1 that Breuer and Bissinger recommend that the separation between the AIP and distortion generator be at least 1.5-2 pipe diameters (Breuer & Bissinger, 2010). As shown in Figure 2-12, the separation distance used in this study is approximately 5.5 pipe diameters, which is considerably greater. This distance was necessitated by practical considerations surrounding the outfitting of existing inlet ducting to accommodate the new inlet distortion traverse assembly.

Bailey and O'Brien experimentally studied the effects of varying the distance between the AIP and the distortion screen from 0.28 to 9 pipe diameters (O'Brien & Bailey, 2013). It was found that mixing between high and low total pressure regions increases with increasing distance. They showed that mixing is greatest near the annulus center in both circumferential and radial directions. The effect of increasing boundary layer thickness with increasing separation was shown to further reduce the total pressure near the tunnel

walls. Furthermore, increasing separation also introduces additional unsteadiness which increases turbulence intensity of the inlet flow. Although the distortion is attenuated at larger distances, the difference in pressure peaks and troughs between the 0.28 and 9 pipe diameters is no more than 2% in their study. Based on the findings and recommendations of Bailey and O'Brien, it is expected that a low porosity, high circumferential extent screen would generate a sufficiently large distortion to yield an appreciable distortion at the AIP.

Figure 2-11. Photograph of the Inlet Distortion Traverse Installed on the P3S Facility

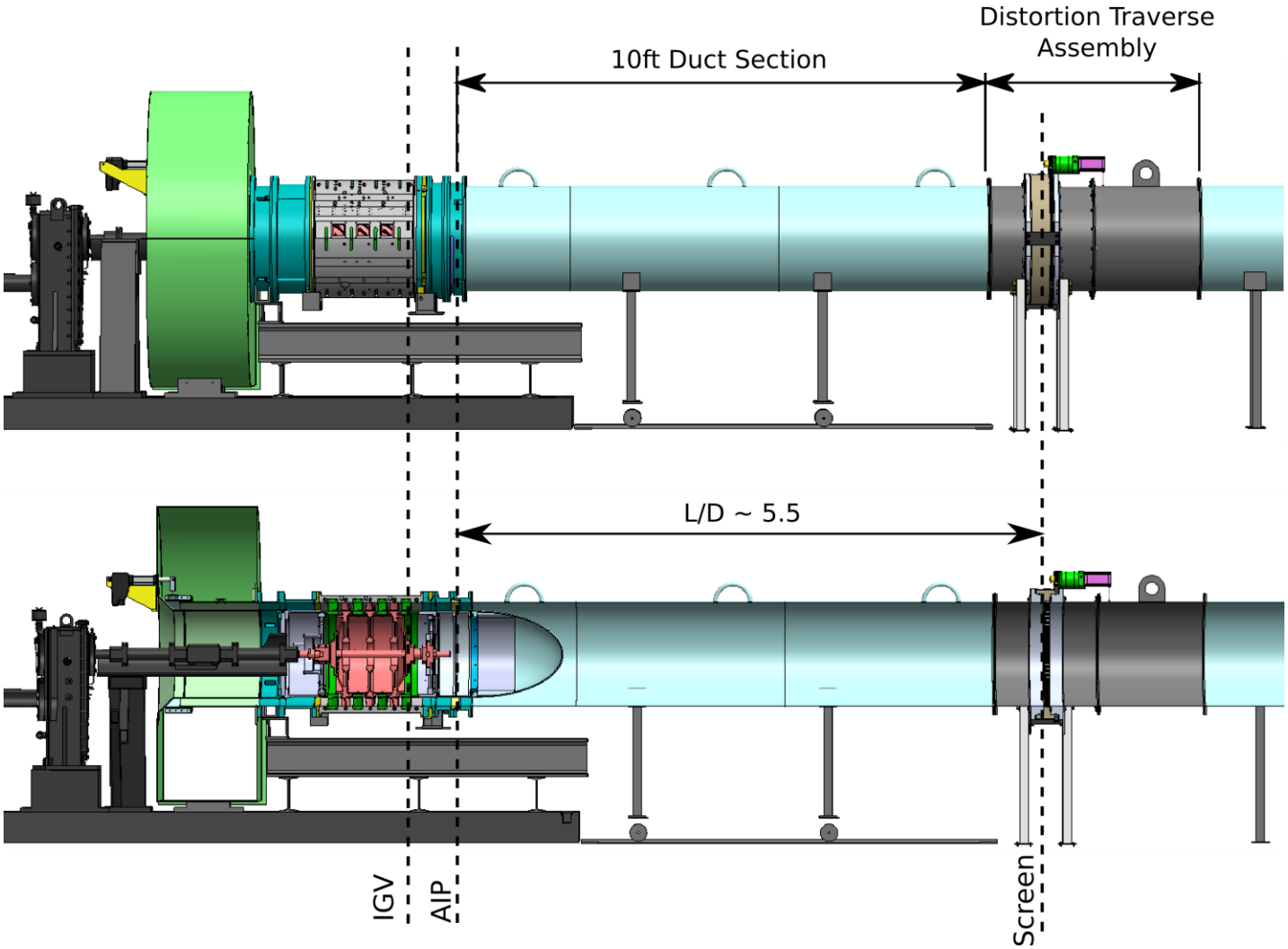

Figure 2-12. Integration of Inlet Distortion Traverse Assembly to Purdue 3-Stage Compressor Research Facility

2.4 Distortion Screen Design Process

The distortion-generating wire gauze screens used in this study were determined iteratively. The focus of this study was not on the distortion parameters, but rather on the acquisition of detailed multi-stage flow measurements for a generic one-per-rev total pressure inlet distortion to be used for validation of advanced computational techniques. Therefore, the goal of the screen design is to select a screen intensity that creates a significant pressure drop that is one that be measured accurately and consistently at the AIP and to select a screen shape that generates a distortion of sufficient extent to have noticeable effect on compressor performance. The effects of screen parameter variation, such as circumferential and radial extents or the porosity, is beyond the scope of the present study. Rather, only a single screen is required to study the attenuation and propagation in a multi-stage compressor environment.

Classical analytical models for the prediction pressure drop through a wire gauze screen were used in the early stages of designing this experiment to guide the preliminary selection of screen porosity. Recall from Chapter 1 that simplified relations model the screen using actuator-sheet theory whereby the pressure drop, ΔP_{screen}, may be calculated for a given dynamic pressure, q_∞, and screen resistance coefficient, K_0, via

$$\Delta P_{screen} = q_\infty K_0 \ . \tag{2.3}$$

The dynamic pressure may be found using the freestream velocity, U_∞, normal to the screen using

$$q_\infty = \frac{1}{2}\rho U_\infty^2 . \tag{2.4}$$

The screen resistance coefficient, K_0, is a function of screen porosity, β, freestream, Reynolds number, *Re*, and Mach number, *Ma* (Karnik & Tavoularis, 1987; Laws & Livesey, 2003). A literature review conducted by Pinker and Herbert (1967) compared various theoretical correlations for K_0 with published experimental data (Herbert & Pinker, 1967). They showed that a model proposed by Annand (1953) best predicted the experimental

findings. The expression for K_0 as a function of Reynold's number for incompressible flow ($Ma = 0$) is

$$K_0 = A_1(\mathrm{Re})\frac{\left(1-\beta^2\right)}{\beta^2}\,, \tag{2.5}$$

where $A_1(Re)$ is a scaling coefficient that is a function of Reynolds number. For $Re > 250$, A_1 approaches a constant value of 0.52 which reduces equation (2.5) to:

$$K_0 = 0.52\frac{\left(1-\beta^2\right)}{\beta^2}\,. \tag{2.6}$$

The porosity, β, is defined as the ratio of open area to gauze area. For simple square-mesh screens, the porosity may be approximated via

$$\beta = \left(1-\frac{d}{l}\right)^2\,, \tag{2.7}$$

where d is the wire diameter, and l is the wire spacing. A more accurate relation was suggested by Pinker and Herbert (1967), which takes into account the sinusoidal shape of the wire (Herbert & Pinker, 1967). Porosity is calculated via

$$\beta = 1-\frac{2}{\pi^2}\left[\left(1+2N^2\right)\left(\frac{\pi}{2}-\cos^{-1}N\right)+3N\sqrt{1-N^2}\right], \tag{2.8}$$

where the parameter N is calculated using

$$N = \pi m d / 2\,, \tag{2.9}$$

where d is the wire diameter and m is the number of strands per unit length.

The inlet flow conditions of the PAX100 research compressor at the location of the distortion screen are outlined in Table 2-2 for a range of inlet mass flow rates. The design mass flow rate at 100%Nc is approximately 20lbm/s, which corresponds to an inlet velocity of 83ft/s. All values shown are calculated at standard day conditions. Since the Reynolds

number is well above 250, relation (2.6) can be used to estimate the screen resistance coefficient, K_0. The pressure drop across the screen can then be estimated using equation (2.3).

The predicted total pressure loss across the screen for a reasonable screen porosity of 50% is tabulated in the rightmost column of Table 2-2. The total pressure loss is a function of the inlet velocity, and hence, the dynamic pressure. Thus, the total pressure loss across a screen of constant porosity changes at different mass flow rates. For this study, the porosity of the screen is held constant, and therefore, the generated distortion will change depending on the mass flow rate condition. Furthermore, the uncertainty of the total pressure rakes used in this study are approximately +/-0.0016 psi, which is an order of magnitude less than the total pressure losses indicated below. This gives reassurance that the instrumentation can measure the magnitudes expected for a reasonable screen porosity of 50%.

Table 2-2. Summary Inlet Flow Conditions for Select Mass Flow Rates

Mass Flow [lbm/s]	Velocity [ft/s]	Dynamic Pressure [psi]	Mach #	Reynolds #	ΔP_{screen} ($\beta = 0.5$) [psi]
16	66.6	0.037	0.06	8.5E5	0.057
18	74.9	0.046	0.07	9.5E5	0.072
20	83.2	0.057	0.07	1.1E6	0.089
22	91.6	0.069	0.08	1.2E6	0.108
24	99.9	0.082	0.09	1.3E6	0.128

2.5 Data Acquisition and Processing Methods

2.5.1 Compressor Operating Conditions

All data sets are acquired at three compressor loading conditions, which are summarized in Table 2-3. These operating conditions result in data sets for three different inlet duct velocities and blade loadings.

Table 2-3. Summary Relevant Compressor Operating Conditions

Condition	Compressor Speed[1] [RPM]	Mass Flow Rate[1] [lbm/s]	Inlet Duct Velocity[2] [ft/s]
Nominal Loading (NL)	5000	20.2	84.1
Low-Loading (LL)	5000	23.2	96.6
High-Loading (HL)	5000	17.7	73.7

[1] Corrected to standard day conditions
[2] Estimated based on corrected mass flow rate and standard day conditions

The compressor operating speed and mass flow rate are corrected using the procedure outlined in section 2.2.3. The compressor is first set to the corrected speed and then subsequently throttled to achieve the desired corrected mass flow rate. Once both corrected speed and corrected mass flow rate are achieved simultaneously, the throttle is fixed for the duration of the data acquisition and distortion traverse. Speed corrections are made before each measurement to account for changes in ambient conditions, primarily ambient temperature.

Because the distortion screen can influence the corrected mass flow rate calculation, the position of the distortion is always kept at bottom-dead-center (BDC) of the duct while setting the compressor operating conditions. This assures that the total and static pressure readings, located near top-dead-center, are measuring the undistorted region of the inlet flow. During post-processing, the corrected operating point is recalculated from raw data averaged across all measurements taken during a particular traverse. If there exists significant deviation from the expected speed and mass flow rate, the measurement is repeated.

2.5.2 Characterization of the Flow Field at the AIP

Characterizing the AIP consists of total pressure data measured using the seven-element Kiel-head rakes whose radial distribution was defined previously in Table 2-1. The radial resolution of the AIP characterization is dictated by the probe locations on the rake while the circumferential resolution is a modifiable parameter based on the selected increment of the distortion screen rotation. Figure 2-13 illustrates how a single rake is used as a virtual rake array at the AIP. The instrumentation rake is fixed while the distortion screen is rotated incrementally relative to the rake.

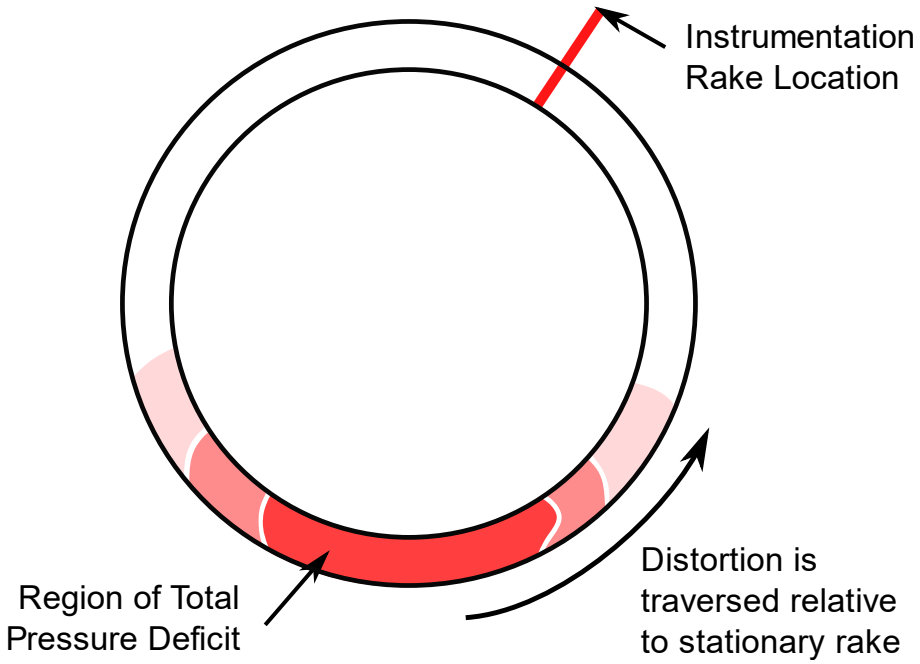

Figure 2-13. Circumferential Traverse Method for AIP Flow Field Characterization

Distortion descriptor elements are used to describe a given distortion at the AIP in terms of radial intensity, circumferential intensity, extent, and multiple-per-revolution elements. The distortion used in this study is a one-per-rev, that is, there is only one low-pressure region per revolution. A distortion having multiple low-pressure regions circumferentially is referred to as a multiple-per-rev distortion, however, these patterns are beyond the scope of this work.

Figure 2-14 defines the standard orientation of AIP contour plots which are oriented such that the flow is coming out of the page. Circumferential positions are referenced clockwise from the top dead center (TDC) position. Each radial probe location forms a complete ring which is referenced by its index number starting from the hub and moving outwards to the tip. Furthermore, Figure 2-14 shows a sample AIP contour plot with sample probe locations to aid in defining relevant AIP parameters.

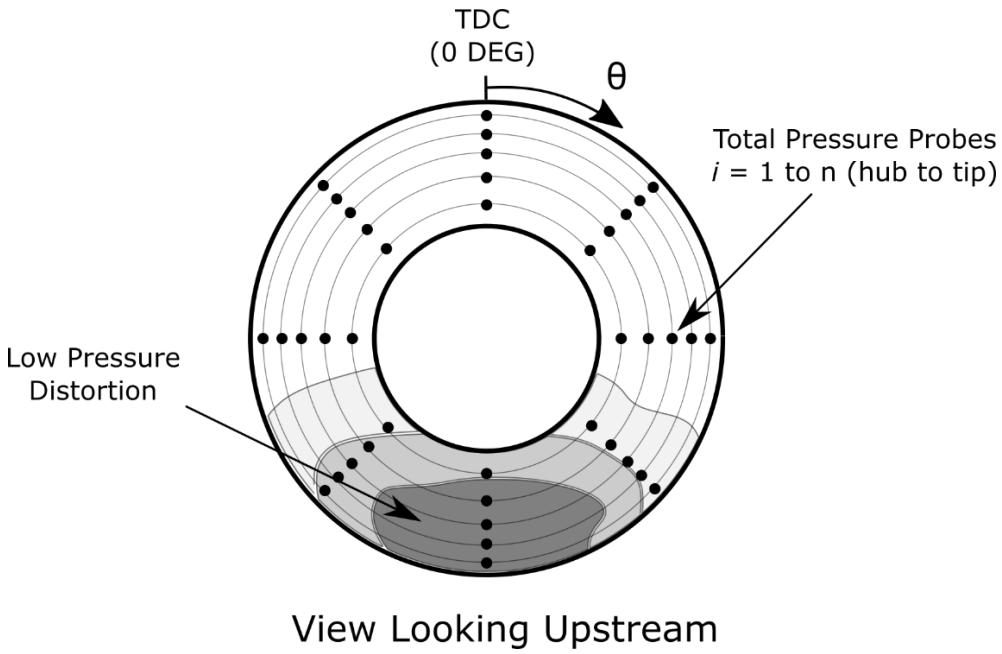

Figure 2-14. Sample Probe Arrangement and AIP Parameter Definitions

Figure 2-15 illustrates a typical circumferential distortion descriptor plot of the i^{th} ring of a one-per-rev total pressure distortion. It shows the measured total pressure at each circumferential location starting at the top dead center going clockwise, as defined in Figure 2-14. Processing techniques presented in ARP-1420 use absolute pressure readings which assumes that all data points were acquired simultaneously using an array of rakes.

Unlike the probe array shown in Figure 2-14, this study uses a virtual probe array by traversing the distortion relative to fixed instrumentation rake. Therefore, pressure readings cannot be directly compared without first considering the variation in ambient conditions

between different circumferential points. Although the time between subsequent measurements is approximately 15 seconds, an entire circumferential traverse can last from half an hour up to 6 hours for the higher resolution inter-stage flow characterization. Pressure readings are normalized by the upstream pitot-static probe total pressure readings at each point in time using

$$P_{0,norm} = \frac{P_0}{P_{0,ps}} \ , \tag{2.10}$$

where P_0 is the measured absolute total pressure and $P_{0,ps}$ is the absolute total pressure measured by the upstream pitot-static probe. Note that all subsequent relations presented in the is chapter utilized normalized pressure values.

As per ARP-1420, the circumferential intensity element, ΔPC/P, is defined as the magnitude of the pressure defect for each ring and is calculated via

$$\left(\frac{\Delta \mathrm{PC}}{\mathrm{P}}\right)_i = \left(\frac{\mathrm{PAV} - \mathrm{PAVLOW}}{\mathrm{PAV}}\right)_i \ . \tag{2.11}$$

The ring average pressure, PAV, is calculated using

$$\mathrm{PAV}_i = \frac{1}{360}\int_0^{360} P(\theta)_i \, d\theta \ , \tag{2.12}$$

and the average low pressure, PAVLOW, is found via

$$\mathrm{PAVLOW}_i = \frac{1}{\theta_i^-}\int_{\theta_{1,i}}^{\theta_{2,i}} P(\theta)_i \, d\theta \ . \tag{2.13}$$

$P(\theta)_i$ is the function defined by the linear interpolation between each total pressure measurement. Finally, the extent, θ_i^-, of the distortion is calculated using

$$\theta_i^- = \theta_{2,i} - \theta_{1,i} \ , \tag{2.14}$$

where θ_{1i} and θ_{2i} are the upper and lower limits, respectively, found from the intersection of the $P(\theta)_i$ and PAV as illustrated in Figure 2-15. Recall that $P(\theta)_i$ is a piece-wise linear function, not a continuous curve fit.

For this study, the circumferential resolution used for flow field characterization at the AIP is high (1°-3°), which permits some simplification of the above relations. Furthermore, because the traverse increments are constant circumferentially, equation (2.12) can be simplified to

$$\mathrm{PAV}_i = \frac{\sum_{i=1}^{N} P_i}{N}\ , \tag{2.15}$$

where N is the circumferential resolution equal to the number of measurements in each radial ring. For small degree increments, equation (2.13) can be approximated as

$$\mathrm{PAVLOW}_i = \frac{\sum_{i=1}^{N} P_i\left[P_i < PAV_i\right]}{\sum_{i=1}^{N}\left[P_i < PAV_i\right]}\ , \tag{2.16}$$

where $[P_i < PAV_i]$ is the Iverson bracket notation which is defined as

$$\left[P_i < PAV_i\right] = \begin{cases} 1 & true \\ 0 & false \end{cases}\ . \tag{2.17}$$

By extension, for a one-per-rev distortion, the extent, θ_i^-, of the distortion defined in equation (2.14) can be approximated via

$$\theta_i^- = \frac{360°}{N} \times \sum_{i=1}^{N}\left[P_i < PAV_i\right]\ . \tag{2.18}$$

The uncertainty in extent calculations introduced by this approximation is equal to at most twice the traverse degree increment. For high resolution circumferential traverses, such as those used in this investigation, this approximation is acceptable.

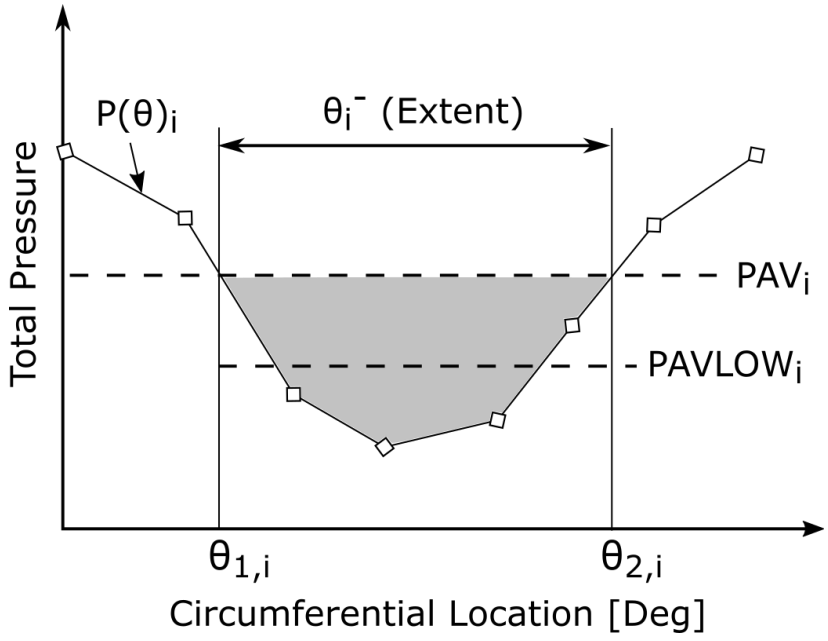

Figure 2-15. Definition of a One-Per-Rev Circumferential Distortion Descriptor Plot as per ARP-1420

The radial distortion element, ΔPR/P, is calculated for each ring from hub to tip. It is defined as the difference between the face-average pressure, PFAV, and ring-average pressure, PAV, normalized by the face-average pressure:

$$\left(\frac{\Delta PR}{P}\right)_i = \frac{PFAV \text{ - } PAV_i}{PFAV} \,. \tag{2.19}$$

The area weighted face average pressure is calculated via

$$PFAV = \sum_{k=1}^{7}\left(PAV_k \times \frac{A_k}{A_{total}}\right), \tag{2.20}$$

where A_k/A_{total} is the area fraction multiplier corresponding to the k^{th} rake element which is summarized in Table 2-1 for all rakes utilized in this investigation. A typical radial distortion descriptor plot from hub to tip for an AIP with 7 radial probe locations is shown in Figure 2-16.

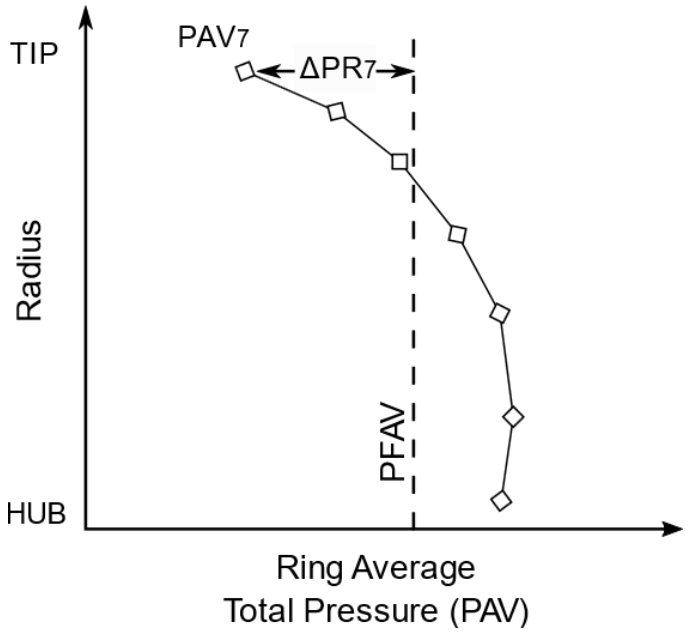

Figure 2-16. Definition of a Radial Distortion Descriptor Plot as per ARP-1420

The distortion descriptor elements provide a means of numerically describing both the magnitude and shape of any total pressure inlet distortion which readily lends itself to comparison and to the development of performance correlations. For this study, all AIP flow fields are reported using the distortion descriptors outlined in this section and via total pressure contour plots. The total pressure contour plots report the percent deviation from PFAV using

$$\%\ \text{Deviation} = \frac{P_0 - PFAV}{PFAV}\ . \tag{2.21}$$

In addition to the distortion descriptors, a maximum distortion percentage is also used for discussion purposes. For a one-per-rev distortion, this maximum distortion parameter provides a quick reference to the difference between the least and most distorted circumferential location. This parameter is defined as

$$\%Distortion = \frac{\max(PRAA) - \min(PRAA)}{PFAV} \tag{2.22}$$

where *PRAA* is the rake area averaged pressure at the i^{th} circumferential position calculated via

$$PRAA_i = \sum_{k=1}^{7} \left(P_{0,(i,k)} \times \frac{A_k}{A_{total}} \right) . \quad (2.23)$$

Again, A_k/A_{total} is the area fraction multiplier corresponding to the k^{th} rake element, which is summarized in Table 2-1. *PRAA*, therefore, offers a single pressure to represent the bulk flow at each circumferential location. It is also used to identify the circumferential location of the maximum average distortion.

The flow chart shown in Figure 2-17 illustrates the experimental procedure for AIP flow field characterization. The operator begins by selecting the desired circumferential increment by specifying the total number of circumferential divisions. The corrected speed at which the data are being collected is specified as a percentage of corrected design speed (100%Nc). This value is used for speed checks which are performed prior to acquiring every measurement to account for any changes in ambient conditions. Additional inputs include stepper motor settings and the quick zero frequency for the pressure transducers.

As mentioned previously, the stepper motor use to rotate the distortion is installed in an open-loop configuration, and therefore, it does not have any absolute positional feedback. Prior to commencing the test, the operator must confirm that the traverse is in the top dead center (TDC) position using the test cell cameras. The speed check takes a quick measurement of select thermocouples and pressure transducers at the AIP and at the venturi which are necessary to compute the corrected compressor operating speed. If the current corrected compressor speed is not within 0.1% (4 RPM) of the desired corrected compressor speed, then the user is prompted to adjust the compressor speed by a specified amount and the speed check is repeated. Once the speed check is satisfied, the measurements at the AIP are taken. Error checking of the data is performed by verifying that measured values are within a reasonable expected range. If there are measurements that are flagged as erroneous, the point may be retaken, or the test may be ended so that the issue can be troubleshooted. In the absence of any errors, the data are written to a file and the stepper motor is commanded to move to the next position where the procedure is repeated, starting again with a speed check.

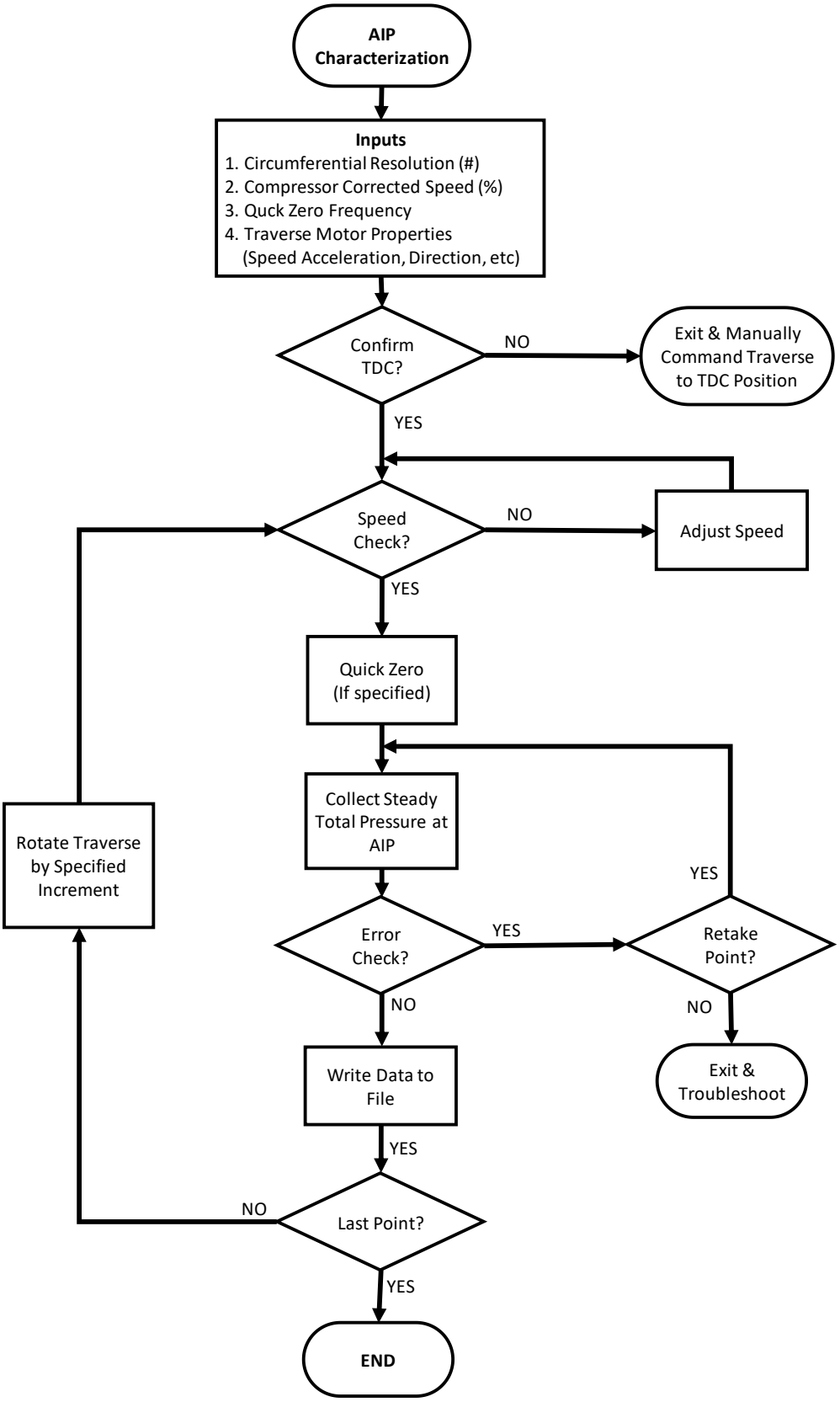

Figure 2-17. AIP Characterization Procedure Flowchart

2.5.3 Turbulence Measurements using Thermal Anemometry

To fully characterize the inlet flow boundary conditions, hot-wire anemometry was used to measure the turbulence intensity at the AIP. Turbulence intensity is an important boundary condition to improve the fidelity of CFD simulation. Turbulence levels have a significant effect on loss generation due to friction, which is especially important when trying to model flow in a multi-stage compressor environment. Turbulence intensity, I, characterizes the turbulence level as a percentage and is defined as

$$I = \frac{U_{rms}}{U_{mean}} \ . \tag{2.24}$$

The mean velocity, U_{mean}, is calculated from a series of discrete velocity measurements via

$$U_{mean} = \frac{1}{N}\sum_{i=1}^{n} u_i \ , \tag{2.25}$$

and the root-mean-squared of velocity, U_{rms}, also referred to as the turbulence strength is calculated via

$$U_{rms} = \sqrt{\frac{1}{N}\sum_{i=1}^{n} u_i^2} \ . \tag{2.26}$$

A constant temperature anemometer (CTA) can be used to measure the fluid velocity with very high frequencies. The velocity is calculated from the heat transfer rate, which is the physical property that is measured by the hot-wire. The heat transfer rate is governed by the fluid velocity, fluid properties, wire geometry, and by the difference in temperature between the wire and the surrounding fluid. For a flow at constant temperature and fluid properties, the only factor affecting the heat transfer rate is the fluid velocity. A hot-wire sensor is one of the resistors in a Wheatstone Bridge. A change in the fluid velocity will cause the wire to either cool or heat up, which will change its resistance. A feedback system instantaneously adjusts the current through the bridge to maintain the wire at a constant temperature. These small changes in sensor resistance can be correlated to the fluid velocity with proper sensor calibration at the given flow conditions.

For this study, all CTA measurements were conducted using a slant-wire probe (TSI 1213-20). It is assumed that that flow at the AIP is 1-dimensional and there is little or no radial or swirl components. Although a slant wire probe can be used as a virtual two-wire probe, for this study, it is used only as a single-wire probe. The probe is connected to a TSI IFA-100 Flow Analyzer that provides the sensor excitation and signal filtering. The sensor voltage signal is output to an NI BNC-2110 connector block that connects to an NI PXIe-1073 chassis where the signal is digitized by an eight-channel NI PXIe-6356 multifunction I/O module. Finally, the signal is recorded onto a computer using a custom LabVIEW interface. The probe orientation relative to the flow and radial position in the annular duct at the AIP is controlled via the L. C. Smith precision probe positioner. Radial turbulence variation is measured by plunging the probe from tip to hub while circumferential variation is measured by rotating the distortion screen traverse relative to the probe. Figure 2-18 shows a block diagram of the hardware involved in this set-up.

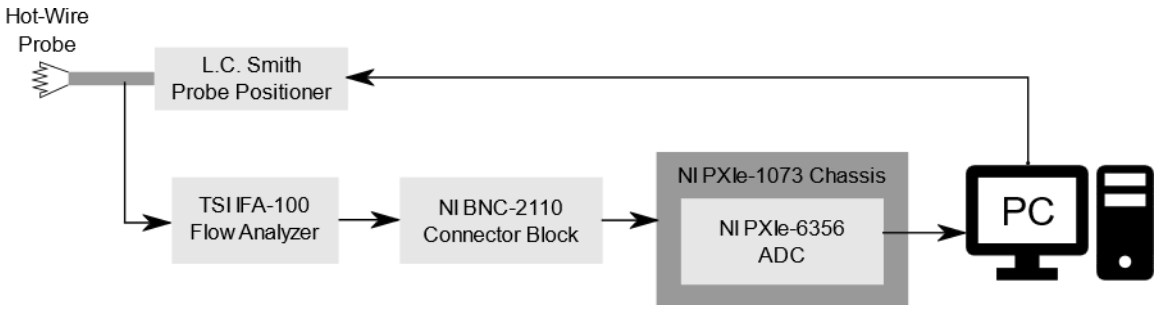

Figure 2-18. Hot-Wire Anemometry Set-Up Block Diagram

The slant-wire probe was calibrated at the Purdue Compressible Hotwire Calibration Facility (Morrison, 2013). This facility provides a low-turbulence jet flow whose temperature and velocity can be accurately controlled. A schematic of the calibration facility is shown in Figure 2-19. A feedback controller can maintain the temperature of the jet to within 0.5°F using two flow heaters installed upstream in series. The temperature of the jet is accurately measured using a total temperature probe located just upstream of the nozzle. Similarly, the jet velocity can be maintained to within 0.2% of desired. Flow speed is measured using a total pressure probe located just upstream of the nozzle and a static

pressure measurement located at the nozzle exit. A detailed discussion on the design and validation of the calibration facility can be found in Morrison (2013).

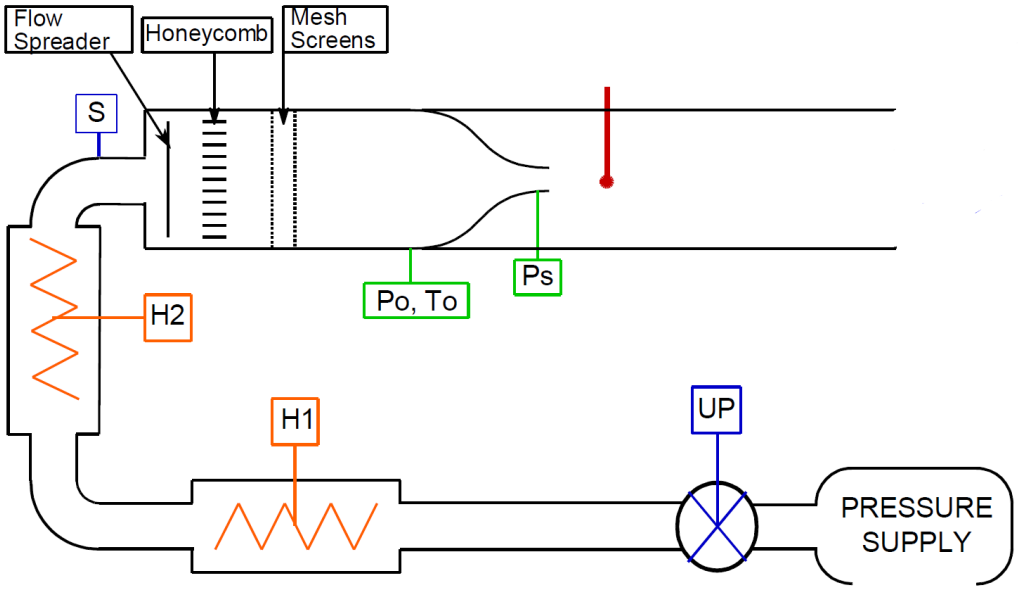

Figure 2-19. Purdue Compressible Hotwire Calibration Facility (Caljet) (Morrison, 2013)

The hot-wire measurement occurs at the AIP where the temperature and density are equal to ambient conditions. Therefore, the calibration of the sensor was performed during a period where the ambient conditions were comparable to those experienced during data acquisition. The sensor was configured using a 20:1 CTA bridge mode with a measured cold resistance of 4.580**Ω** and a manufacturer specified operating resistance of 10.58**Ω**. The probe was subjected to the upper limit of the expected inlet velocity (~300ft/s) while a square wave test was used to optimize the frequency response to approximately 80 kHz. The probe was calibrated over a velocity range typical of what is expected to be encountered at the AIP. To maximize the resolution of the measurement, the gain and offset were adjusted to make full use of the -5V to 5V range (Gain = 20, Offset = 3). The temperature of the calibration jet was constant and equal to 77°F throughout the duration of the calibration.

The calibration jet velocity was incremented by 25ft/s from 325ft/s down to 150ft/s. Multiple hot-wire measurements were taken at each increment and are plotted in Figure 2-20. A quadratic curve fit was used to model the trend with a resulting R^2 value of 0.9989.

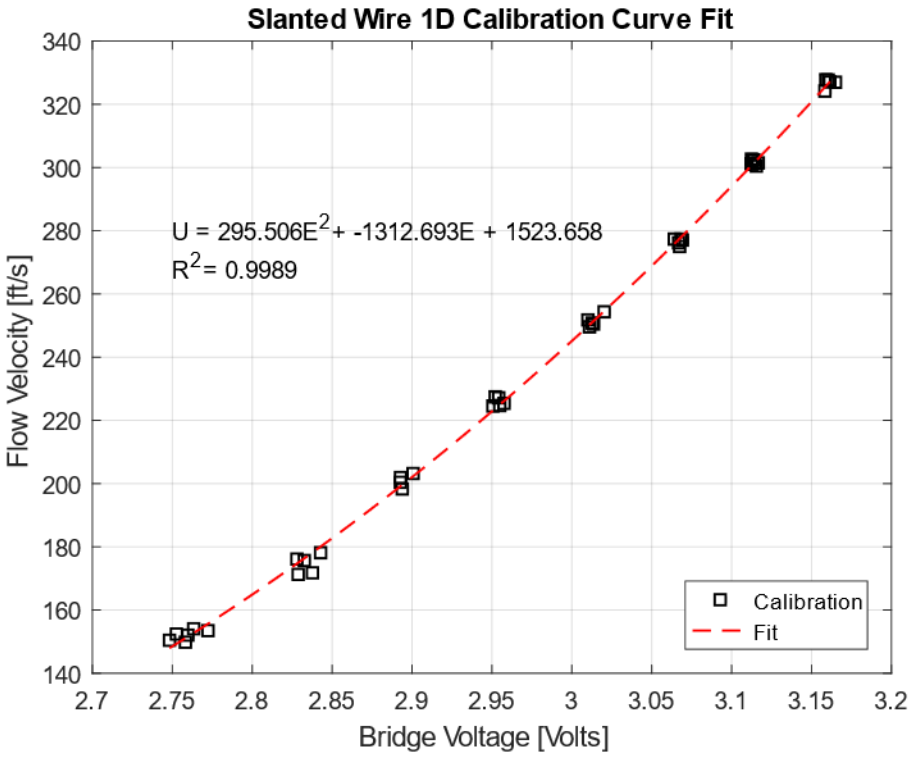

Figure 2-20. Hot-Wire Velocity Calibration Curve

To account for small variations in temperature between test conditions and calibration conditions, the measured voltage, E, was corrected using

$$E_{corr} = E\sqrt{\frac{T_w - T_0}{T_w - T_a}}, \tag{2.27}$$

where E_{corr} is the corrected bridge voltage, T_w is the manufacturer prescribed constant wire temperature, T_a is the stagnation temperature at the measurement location, and T_0 is the ambient temperature at the time of calibration. The correct form of the above correction utilizes static temperatures, however, at low Mach numbers, the difference between stagnation and static temperature is minimal.

Prior to applying the temperature correction using equation (2.27), the actual bridge voltage must be reconstructed. Using the acquired voltage, E_a, and the known signal conditioning parameters, the bridge voltage, E, is calculated from

$$E = \frac{E_a}{Gain} + E_{Offset} \ . \tag{2.28}$$

Once the actual bridge voltage is corrected using relation (2.27), a flow velocity can be calculated from the calibration curve shown in Figure 2-20. In summary, the calibration curve is

$$U = 295.506E^2 - 1312.693E + 1523.658 \ , \tag{2.29}$$

where U is the flow velocity in ft/s and E is the bridge voltage in Volts.

2.5.4 Multi-Stage Distortion Propagation Measurements

The section details the methodology used to acquire total pressure measurements before and after each blade row. These measurements aim to provide insight on the propagation and attenuation of the total pressure inlet distortion as it passes through a multi-stage compressor using a single rake measurement to approximate the flow through each vane passage. Although the PAX100 research compressor is representative of the rear stages of an HPC, which are typically not subjected to large magnitude flow distortion, this dataset is valuable for the validation of novel computational methods and to the study of distortion propagation and attenuation flow physics.

For this portion of the study, the PAX100 research compressor is outfitted with total pressure rakes in ports 0 to 9, as discussed previously in Figure 2-3. The probes are positioned outside of the stator wakes to approximate the bulk flow properties. The flow through the passages is relatively uniform except when the probe is located in the wake. Although the probes are not all located at mid-passage, they are all located outside of the wakes. Therefore, it can be assumed that the rake measurements approximate the bulk flow through the passage.

Figure 2-21 shows an illustration of stator 1 (S1) with a sample region of total pressure deficit overlaid in red. The rake shown is positioned roughly mid passage which measures the nearly constant bulk properties of the flow passing through that vane passage. To capture the flow properties in each of the stator passages using one fixed rake, the distortion is traversed by an increment corresponding to the pitch of a vane passage. Therefore, a full traverse will consist of as many increments as there are stator vanes. Once the total pressure is measured in all vane passages, the circumferential location and magnitude of the distortion can be approximated as it propagates through each stage.

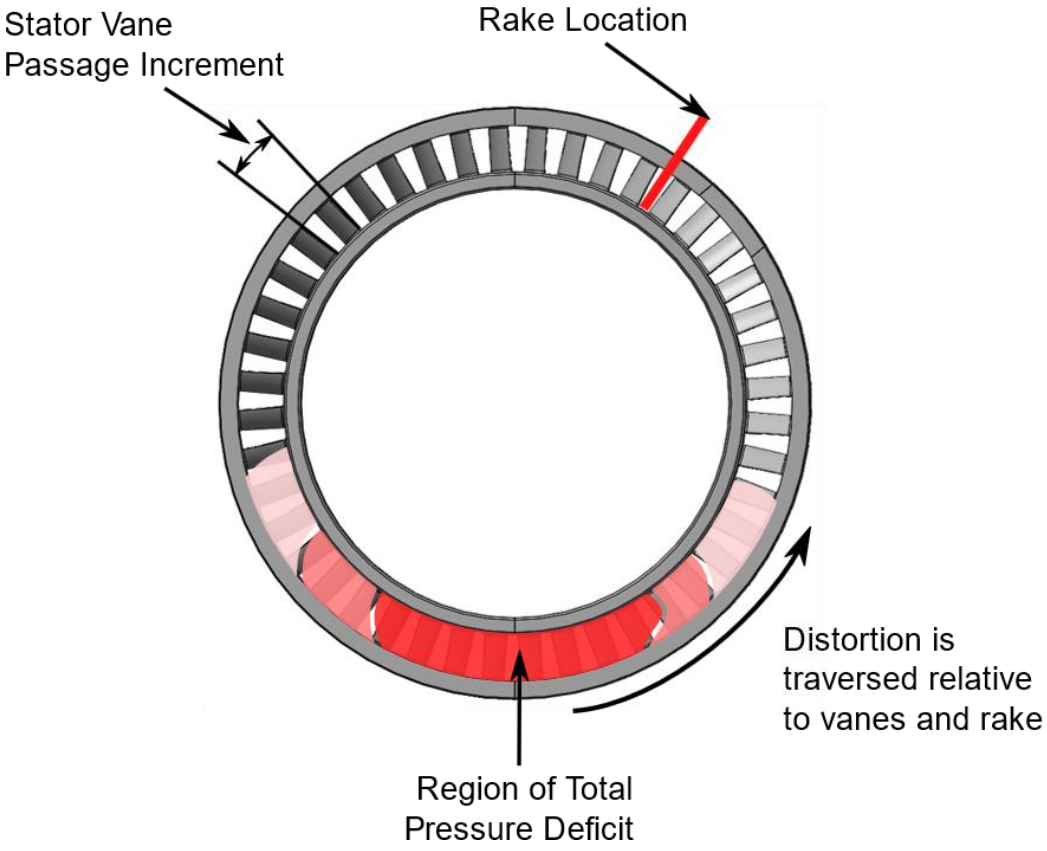

Figure 2-21. Rake Location Relative to Vane Passages

The experimental procedure is similar to that described for AIP flow field characterization in Figure 2-17. The difference is that the total pressure rakes are measuring the inter-stage flow properties at stations 0 to 9 as discussed previously. Furthermore, because the IGV, S1, and S2 have 44 vanes, and stator 3 has 50 vanes, the traverse must be carried out twice;

first with 44 increments, and again with 50 increments. This procedure is repeated for low, design, and high-loading conditions at 100% corrected speed.

2.5.5 Inter-Stage Flow Field Characterization

The final study involves an improvement on the investigation discussed in the previous section. Instead of approximating the bulk flow through each passage using a single measurement in each passage. The vanes are also traversed such that measurements are obtained at 20 evenly spaced increments to capture 100% of each vane passage. In combination with a coordinated traverse of the distortion upstream, a high-resolution total pressure field can be acquired of the full annulus capturing all wakes and passage flows. Although the study duration is approximately 20 times longer than the approximate traverse method discussed in the previous section, this study can be completed in a reasonable time of approximately 6-7 hours.

Figure 2-22 shows a flow chart of the inter-stage flow field characterization procedure. In summary, all of the vanes are rotated in unison to the desired vane passage position. The vane passage position is defined as a percentage of one vane passage corresponding to IGV, S1, and S2 which all have 44 vanes. Data are acquired in a fashion identical to that outlined in the previous section whereby the distortion is traversed by 44 equal increments, and total pressure measurements are acquired for each passage corresponding the current vane passage position. Next, the vanes are rotated to the next vane position, and the distortion traverse is repeated until a distortion traverse has been performed at all vane position. The measurements are then combined to produce a continuous total pressure field.

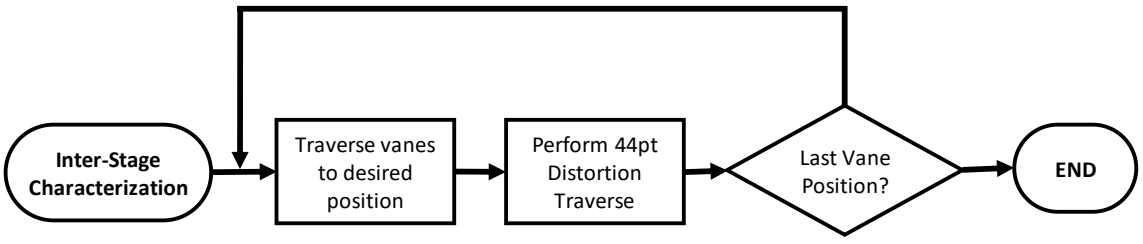

Figure 2-22. Inter-Stage Flow Field Characterization Procedure

CHAPTER 3. TOTAL PRESSURE INLET DISTORTION RESULTS

3.1 Overview

This chapter presents the results of the total pressure inlet distortion investigations carried out on the PAX100 3-stage axial research compressor. As this is the first time that the inlet distortion traverse system was implemented in this facility, the first investigation characterized the effect of honeycomb carrier alone on the inlet flow at the AIP. Next, results from the iteration of the distortion screen shape and porosity are presented. Using the final selected screen candidate, detailed total pressure field characterization, along with turbulence intensity spatial variation, are presented at the AIP to fully describe the inlet boundary conditions for future CFD investigations. The final investigations present measurements showing the propagation and attenuation of the total pressure distortion through each of the three stages of the compressor.

3.2 Carrier-Only Inlet Flow Uniformity Results

Prior to introducing distortion screens at the inlet, the distortion traverse system was installed with the honeycomb carrier only. The primary objective of this investigation was to study the effect of the carrier alone on the total pressure profile at the AIP compared to the clean inlet condition with no carrier. Both circumferential and radial total pressure variation was captured by rotating the honeycomb relative to the fixed AIP instrumentation rakes, as described in section 2.5.2. The resulting data set reveals if there are any non-uniformities introduced into the flow by carrier.

The individual cells of the aluminum honeycomb carrier are quite fragile, and it is very difficult to achieve a perfectly uniform cell shape and size when installed. Although these minor variations are of no concern for structural considerations, they may introduce some non-uniformity into the flow which may manifest itself as circumferential or radial distortion at the AIP. Therefore, it was important to quantify this effect prior to introducing the distortion screens.

The compressor speed was set to 100% corrected speed and the compressor was throttled to the nominal loading (NL). The exact compressor operating point is not important since the only thing affecting the total pressure losses at the AIP is the mass flow rate. The AIP instrumentation is also sufficiently far upstream that it should be isolated from any potential effects downstream. For consistency, all data was acquired at the same compressor operating points for all investigations.

The distortion screen was rotated in 3° increments for a total of 120 circumferential rake positions. The total pressure measurements are normalized to account for temporal fluctuations in ambient conditions using the method outlined in section 2.5.2. Figure 3-1 shows the resulting total pressure field at the AIP with only the honeycomb carrier installed upstream. Recall that contour plots are plotted in accordance to the coordinate frame outline earlier in Figure 2-14.

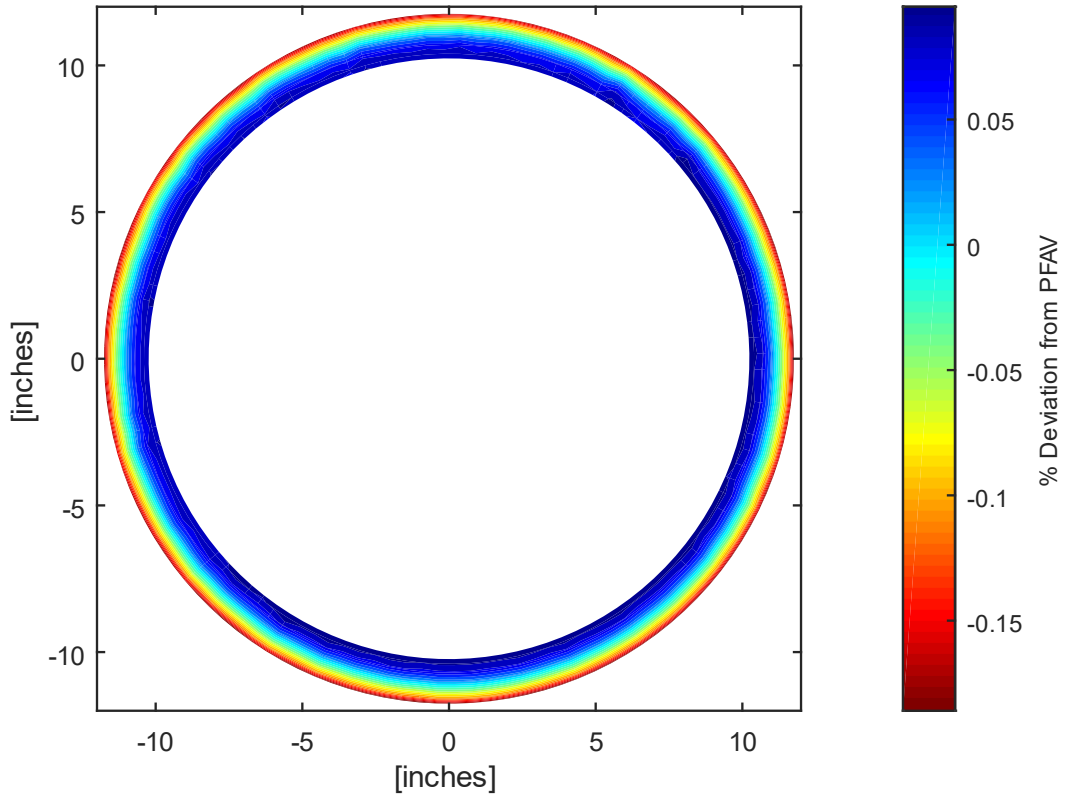

Figure 3-1. Total Pressure Field at AIP – Carrier Only - NL

The total pressure contour plot at the AIP shows that there are no significant circumferential non-uniformities introduced by the honeycomb carrier. This finding is further supported by Figure 3-2 which shows the normalized total pressure variation circumferentially at each radial location. The radial location is indicated in the legend as the percentage of span or annulus height from hub to shroud.

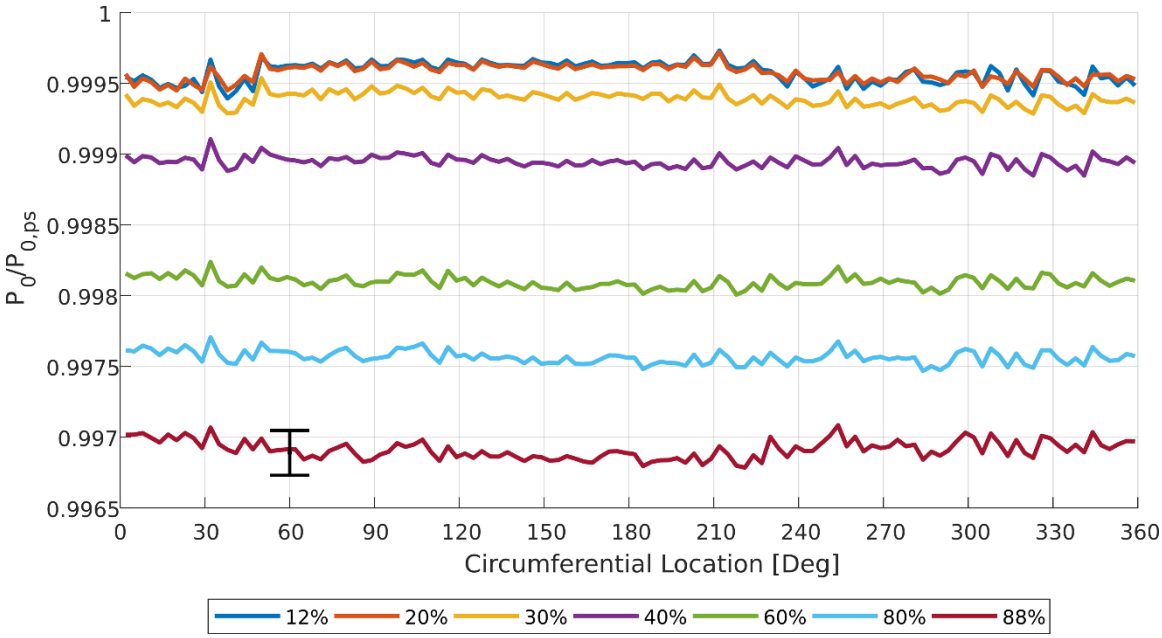

Figure 3-2. Circumferential Variation in Total Pressure at AIP – Carrier Only - NL

Error bars are included for a single point on the 88% span line to provide a sense of scale. Although there is some fluctuation, it remains within the uncertainty of the total pressure measurement. Furthermore, the data were constructed from two separate pressure rakes located 180° apart. Multiple, evenly space probes reduce the time required for inlet flow field characterization. However, there is some error introduced into the measurement due to limitations in accuracy on probe depth positioning and variations arising from the inherent differences between the rakes and pressure transducer channels.

These differences can be seen in the small discontinuities occurring at 50° and 230° in the peripheral rake elements (12% and 88%). This is most likely due to slight variations in radial position of the rakes in the annulus. For the rake elements in the middle of the

passage, the pressure gradient is smaller, and therefore, small changes in probe positions do not yield large changes in measure total pressure. For the peripheral rake elements, small changes in radial location yield more significant changes in the total pressure measurements due to the proximity to the boundary layer where the pressure gradient is large.

Despite this small variation between the rakes, the multiple rake total pressure field measurement method was deemed acceptable since the variations fell within the uncertainty of the probes. This investigation also demonstrated that the automated inlet distortion traverse and data acquisition control systems were capable completing detailed traverse in a shorter time frame than initially predicted. Therefore, the need for multiple probes at the AIP was deemed unnecessary for further investigations since the data acquisition time with a single rake was reasonable. Furthermore, using a single rake eliminated any uncertainty associated with the issues discussed above.

To further characterize the AIP inlet flow, the radial distortion is shown in Figure 3-3 as per the methods outlined in section 2.5.2. In addition to the ring average pressure curve shown in red, the maximum and minimum measurement envelope is also shown. The error bars represent the total pressure measurement uncertainty normalized by the average upstream pitot-static total pressure measurement for all points. The maximum variation in measurements at all circumferential location, represented by the max/min envelope, largely falls within the extent of the error bars. Therefore, it can be concluded that all circumferential non-uniformities at the AIP fall within the measurement uncertainty and that the honeycomb carrier does not introduce any circumferential distortion.

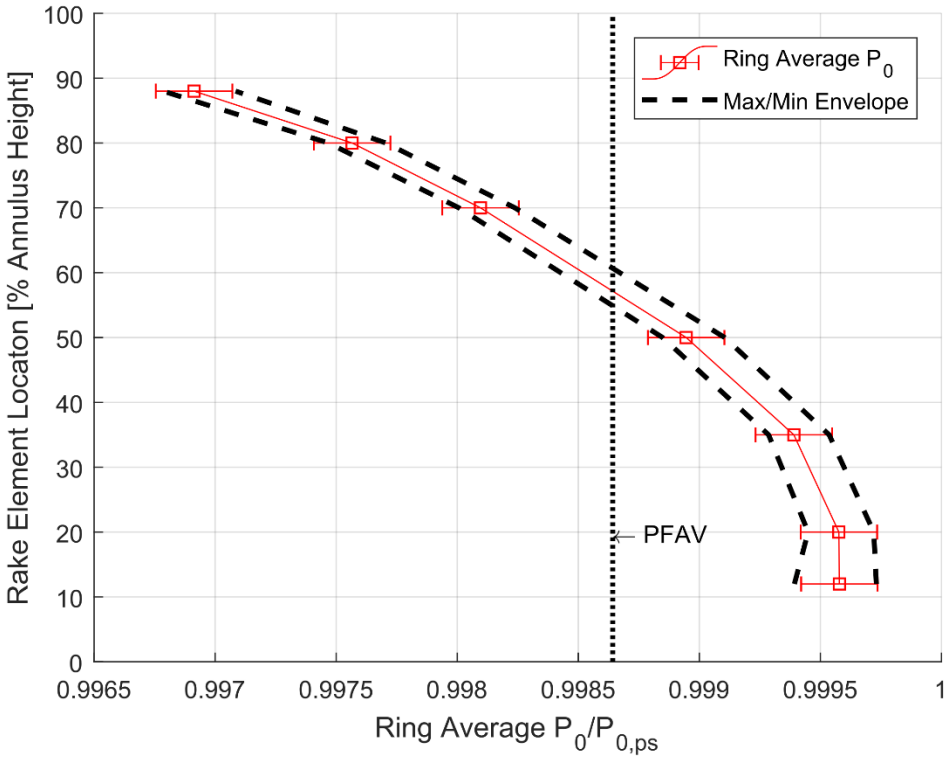

Figure 3-3. Radial Variation in Total Pressure at AIP – Carrier Only - NL

Honeycomb was selected as the distortion screen carrier because it offered good structural integrity without introducing excessive blockage or distortion, as do traditional carriers made of thicker gage wire. The AIP total pressure profile measured with the carrier installed is compared to the clean inlet configuration of PAX100 compressor at nominal loading mass flow rate in Figure 3-4. As expected, there is some additional pressure drop caused by the honeycomb which varies based on radial location. The area averaged pressure of the entire AIP (PFAV) for both profiles is also shown. The average total pressure loss introduced by the carrier is calculated to be 0.04%, which is approximately 3 times larger than the uncertainty of the measurement.

Although the average pressure loss is minimal, the honeycomb carrier introduces some radial distortion compared to the clean inlet profile. There is a greater pressure loss near the hub and shroud compared to the mid-passage flow. As a result, the profile has a more curved appearance whereas the clean inlet flow is nearly linear from hub to shroud. Note

the difference in uncertainty between the two curves is due to the large number of measurements available for the carrier-only curve whereas the clean inlet curve is only a single measurement.

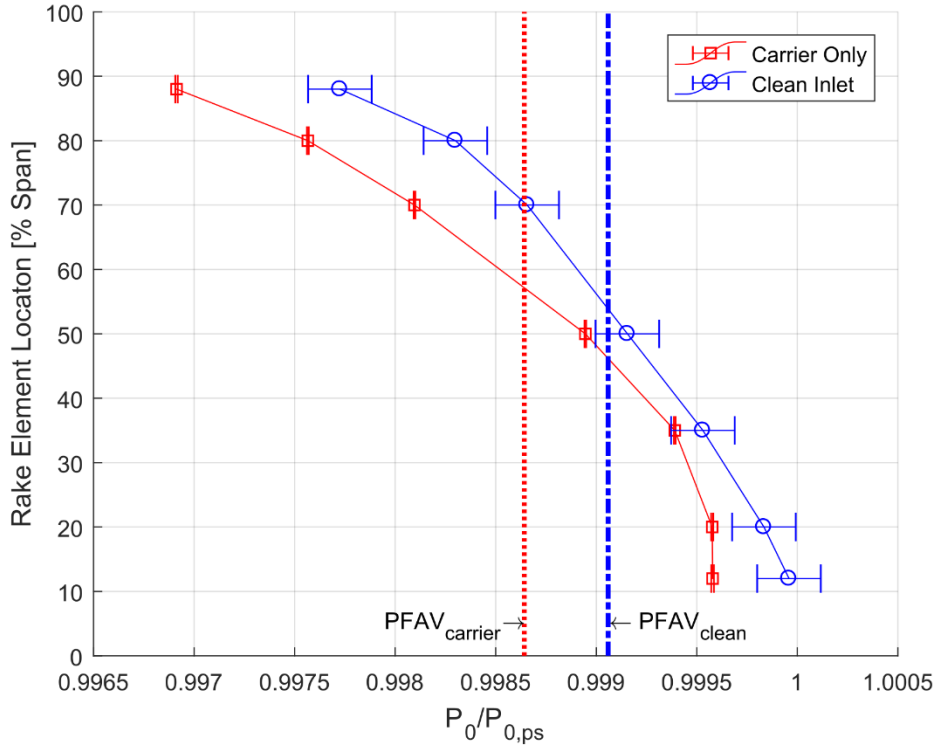

Figure 3-4. Inlet Total Pressure Profile Comparison with Clean Inlet - NL

In conclusion, this study has demonstrated that the honeycomb carrier alone does not introduce any circumferential distortion, and the additional pressure drop introduced is minimal. Despite the slight change in inlet profile shape, it is an order of magnitude smaller than the expected pressure drop introduced by the distortion screens, and therefore, it is of no concern.

3.3 Distortion Screen Selection Process

As previously discussed, the focus of this investigation was not to replicate some prescribed distortion or to study the effect of different distortion parameters, rather, the only criteria guiding the selection of a distortion screen was that it be one-per-rev and be sufficiently strong that it can be measured at the AIP. Since the PAX100 compressor is a

model of the final three stages of an HPC, they typical distortion levels present in these stages would be attenuated compared to the fan inlet distortion levels.

The first screen shape had 100% radial extent and 120° circumferential extent. The screen consisted of two identical screens overlaid with the strand orientation at 45° to one another. The porosity of the individual screen was calculate to be approximately 74% using relation (2.8) discussed in section 2.4. The porosity of the two identical screens overlaid at 45° can be estimated by the product of the individual porosity. Therefore, the approximate porosity of the first screen candidate was calculated to be 54%.

Following recommended practices from literature, rather than reducing the porosity of a single screen for subsequent iterations, additional screens were added to avoid introducing excessive unsteadiness associated with single low porosity screens (Laws & Livesey, 2003). A total of three screen iterations were tested for this investigation. For the second screen iteration, two additional screens were added to the first screen candidate. The added screens had a similar calculated porosity to the initial screens but consisted of different wire gage and spacing. For the third screen iteration, another 2 screens were added; one of the fine wire gage and one of the thicker wire gage. The exact porosity of 2nd and 3rd screen candidates is difficult to estimate. However, the exact porosity is not important for this study, as long as it produces the an appreciable one-per-rev total pressure distortion at the AIP.

The AIP total pressure field was characterized using the procedure outlined in section 2.5.2. A quick low-resolution traverse was done for the purposes of screen evaluation at the nominal loading inlet mass flow rate. A low-resolution traverse was sufficient to capture the pressure drop at the AIP while reducing facility operating time. The operating mass flow was set to compressor nominal loading at 100%Nc for all screen iterations. The data were collected on similar days to minimize the change in the actual mass flow rate between tests. The circumferential variation in rake area-averaged pressure is shown in Figure 3-5 to compare the pressure drop caused by the different screens. A photograph of the final screen candidate is also included in Figure 4-6.

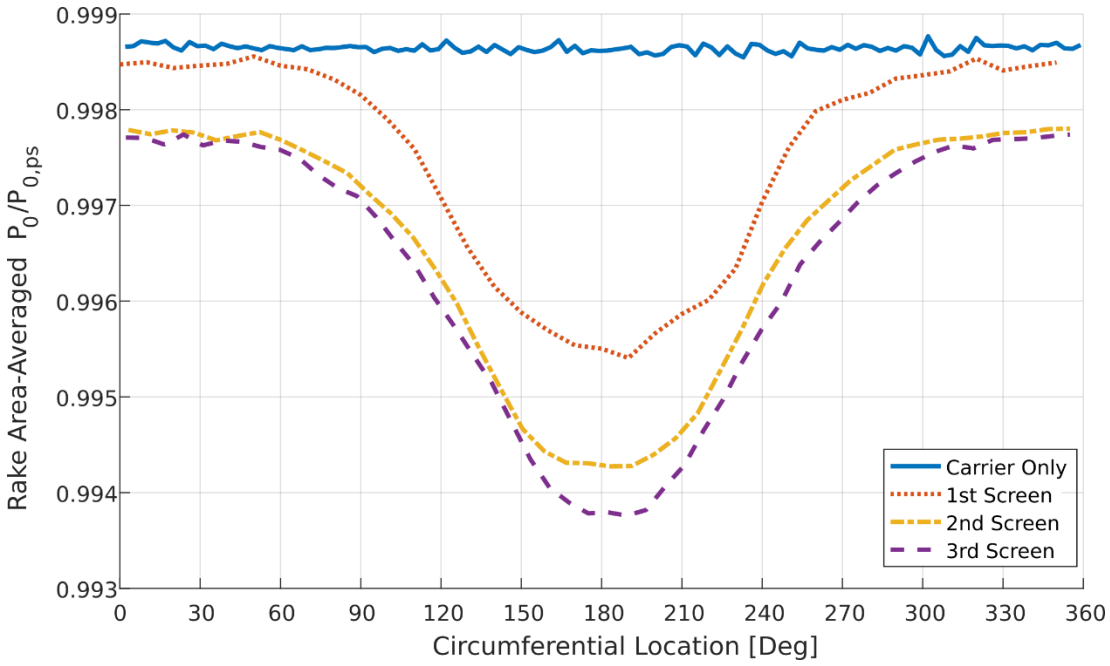

Figure 3-5. Comparison of Circumferential PRAA Variation at AIP – Nominal Loading

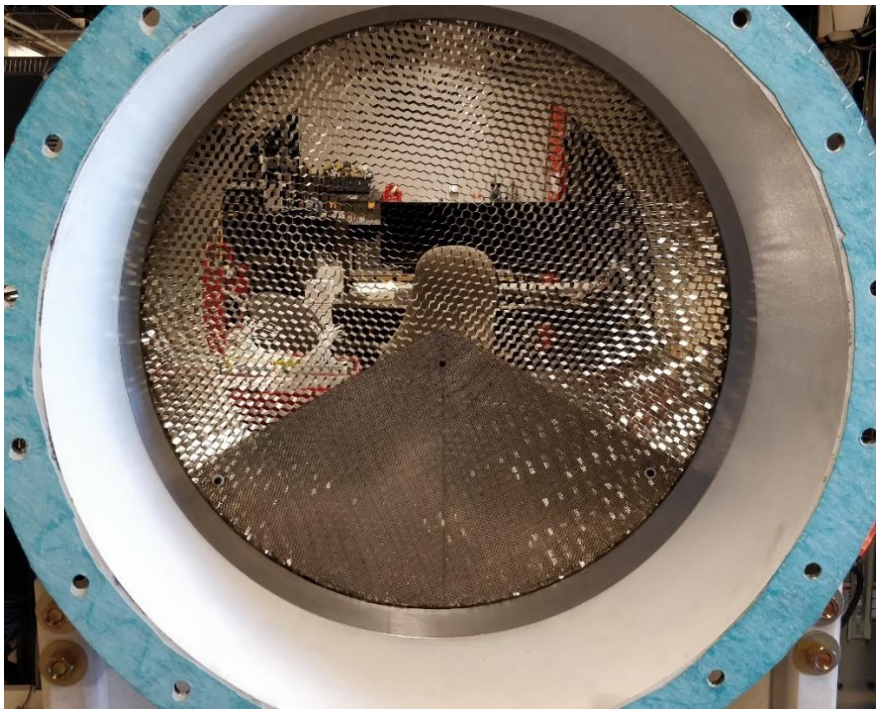

Figure 3-6. Photograph of Final Screen Candidate Installed in Traverse

Figure 3-5 shows that a noticeable pressure deficit exists with a minimum at 180°, which corresponds to the BDC position. The carrier-only rake area-averaged total pressure variation is also included for reference. With each reduction in screen porosity the pressure drop also increases as expected. A reduction in pressure is also observed in the region opposite the distortion where the flow is undistorted. This indicates that reduction in screen porosity leads to increased unsteadiness which expedites mixing between the low-pressure and high-pressure regions between the screen and the AIP.

The additional pressure drop between the 3rd and 2nd screen iteration is not as large as between the 2nd and the 1st. This indicates that a further reduction in screen porosity may not be very effective in achieving a higher magnitude of the distortion. Mixing effects begin to dominate which act to lower the face average pressure as opposed to increasing the peak magnitude of the circumferential distortion. Also, further reductions in porosity would risk introducing excessive blockage and unsteadiness into the inlet flow which is undesirable for this type of study. Therefore, the third screen iteration was utilized for the remainder of the study.

3.4 Detailed AIP Flow Field Characterization

Using the final screen candidate, the total pressure field at the AIP was characterized with high circumferential resolution. Three compressor loading conditions at 100% corrected speed were investigated (Table 2-3). The AIP total pressure field was characterized using the procedure discussed in section 2.5.2. For the nominal loading condition, the AIP was characterized with a circumferential resolution of 360 providing measurements at 1° increments.

Figure 3-7a shows the resulting total pressure field at the AIP for the nominal loading operating condition. The one-per-rev total pressure distortion occurs at the bottom-dead-center at the AIP. Figure 3-7b further illustrates the circumferential variation in total pressure for different radial positions. The dips in pressure are all symmetric about the 180° position indicating that there is no swirl present between the distortion screen and the AIP. Sample error bars are included for a single point on the 88% span line to provide a sense

of scale. Results for high loading and low loading conditions are shown in Figure 3-8 and Figure 3-9 respectively. Since the distortion transition was smooth a reduction in traverse resolution for AIP characterization is acceptable. Therefore, to reduce facility operation time, HL and LL were characterized with 180 points instead of 360.

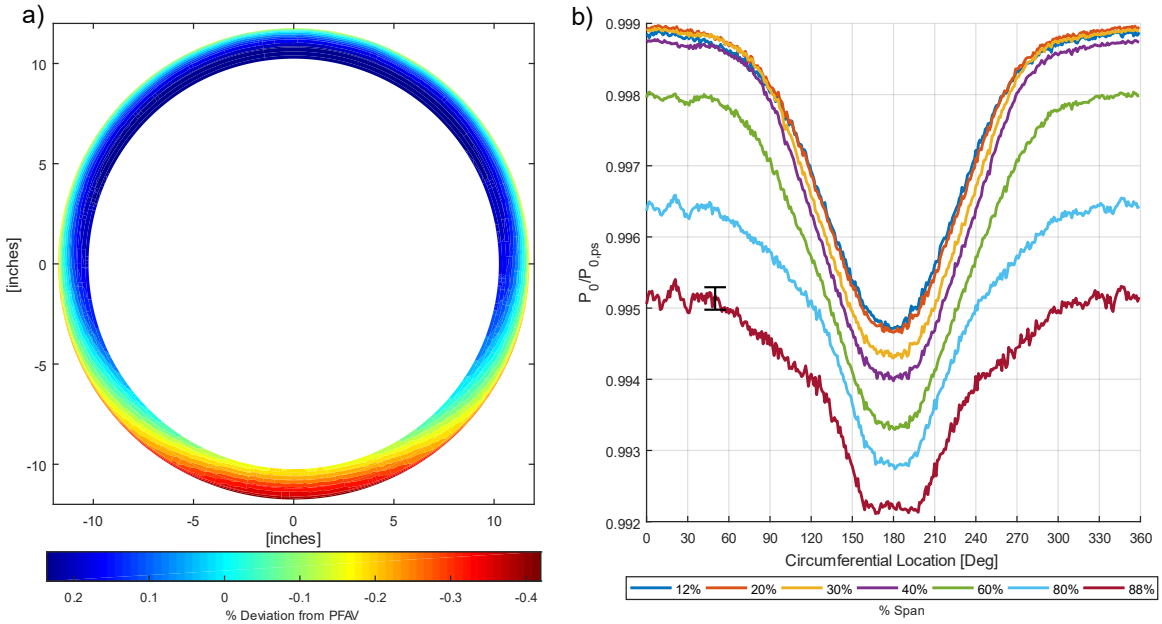

Figure 3-7. Total Pressure (a) Field and (b) Circumferential Variation at AIP – Nominal Loading

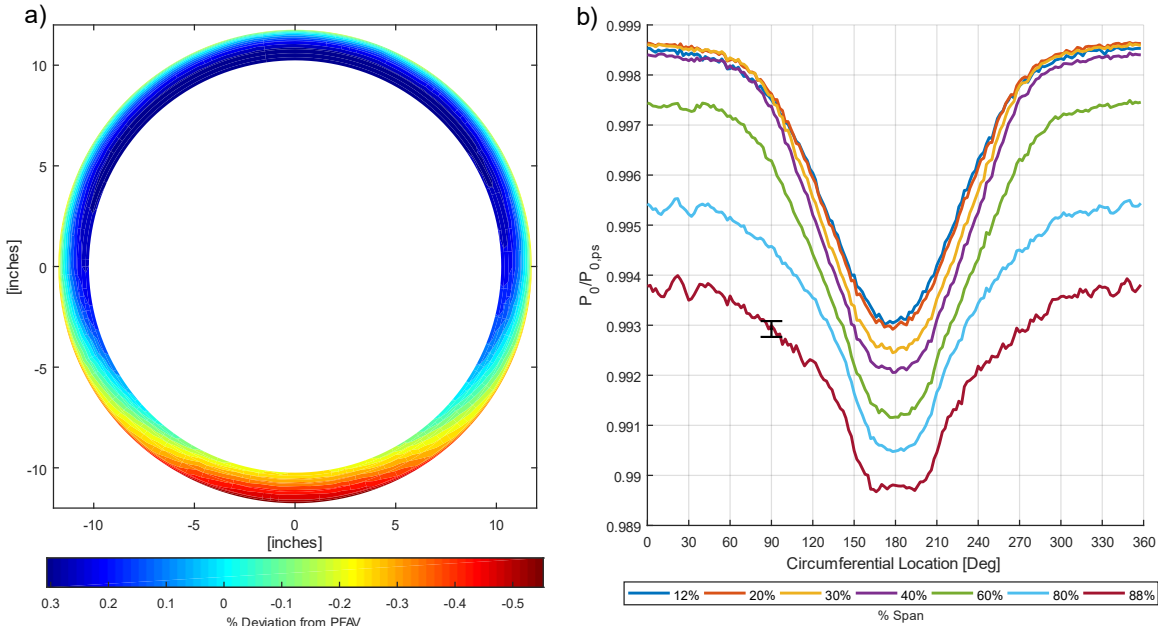

Figure 3-8. Total Pressure (a) Field and (b) Circumferential Variation at AIP – Low Loading

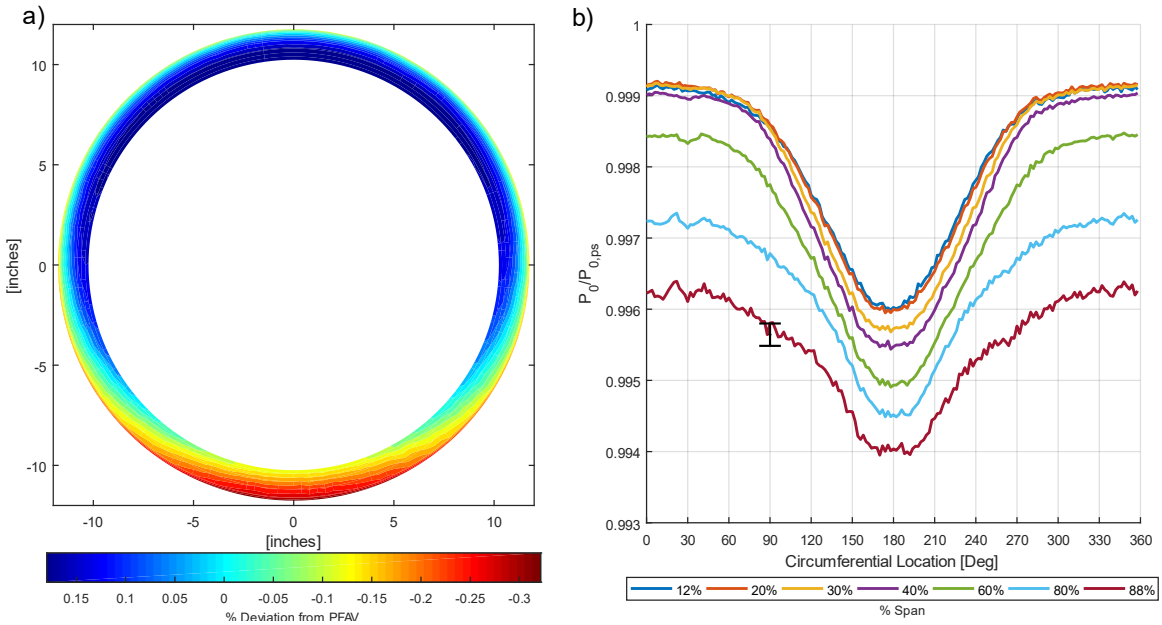

Figure 3-9. Total Pressure (a) Field and (b) Circumferential Variation at AIP – High Loading

The radial distortion at nominal loading is plotted in Figure 3-10a as per ARP-1420. The radial profile is comprised of the ring average pressure, PAV, at each radial location. The distortion screen used in this study has a 100% radial extent and should not introduce any significant radial distortion. To better illustrate the effect of the distortion on the radial distortion, the radial profile of the carrier alone is also included for reference.

Figure 3-10a shows an overall drop in the face average pressure, PFAV, caused by the distortion screen. To study the change in radial profile, Figure 3-10b shows the same radial profiles normalized by their respective PFAVs. Up until approximately 70% span, the profile shapes are nearly identical. In the tip region, however, there is a greater pressure drop observed.

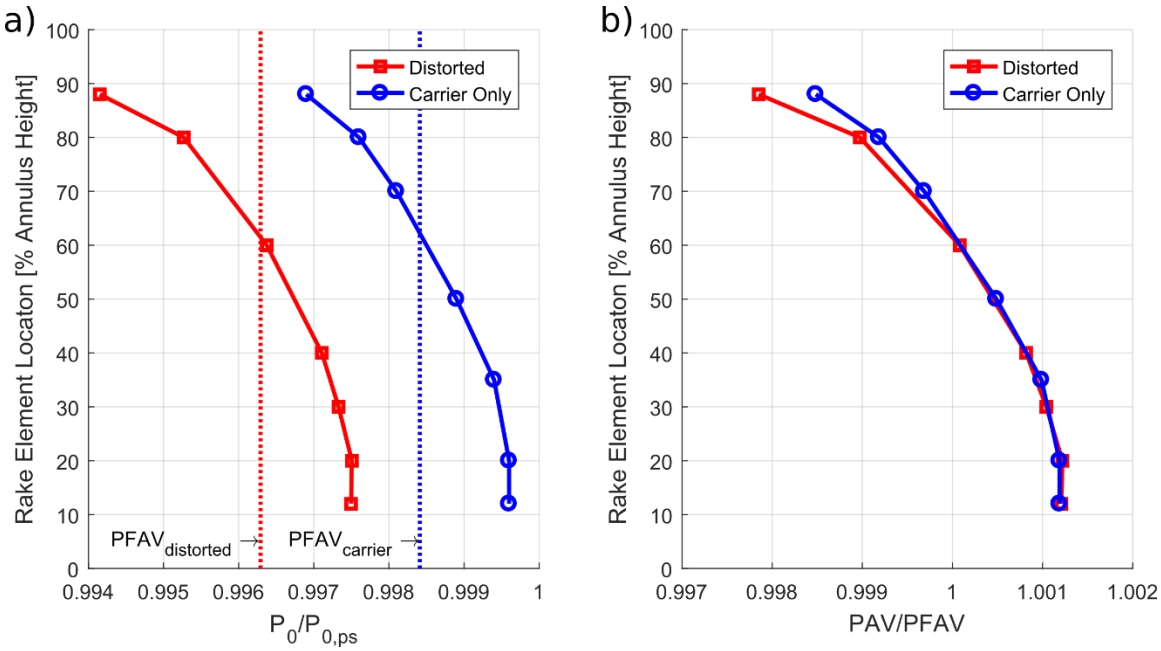

Figure 3-10. a) Radial Variation in Total Pressure, b) Profile Comparison at AIP – Nominal Loading

O'Brien & Bailey (2013) observed that mixing between low and high-pressure regions downstream of the distortion screen is greater in the center of a duct where the pressure gradient is high. The tip distortion observed in Figure 3-10b can be attributed to this non-uniform radial mixing which is accentuated by the large spacing between the screen and the AIP. The flow on the periphery of the duct has a shallower pressure gradient and experiences less attenuation compared to the flow in the center of the duct.

As the distance between the AIP and the distortion screen increases, the effect of the non-uniform mixing results in a radial distortion as observed in Figure 3-10. In the absence of any mixing, the circumferential distribution would have a step function-like appearance whereas mixing will try to equalize the difference between the low and high-pressure regions as illustrated in Figure 3-11. Immediately downstream of the distortion screen and in regions where there is less mixing, the circumferential pressure variation will have a more ideal appearance.

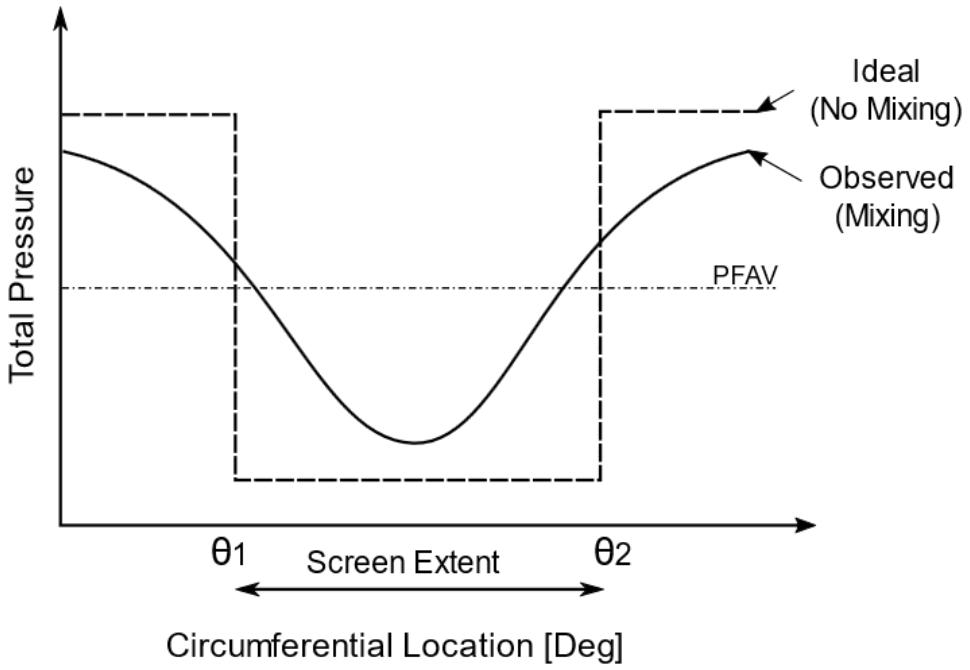

Figure 3-11. Ideal vs. Non-Ideal Pressure Drop Across Screen

This phenomenon is observed in the circumferential distortion plot shown in Figure 3-7. The 88% span curve shows a flat pressure drop in the distorted region whereas the other spans have a smoother, more continuous appearance, thereby indicating that there exists a difference in the mixing rate radially.

Figure 3-12a shows a comparison of the radial total pressure variation for nominal, low, and high loading conditions. As expected, the magnitude of the average total pressure drop increases with increasing mass flow rate. Since pressure drop across the screen varies with inlet flow velocity, nominal loading is shown to produce both the highest distortion magnitude and also the greatest drop in face average pressure. Therefore, when designing distortion screens, it is important to also consider the effect of the screen on the face average pressure as well as the distortion shape and magnitude. Furthermore, Figure 3-12b also shows that the radial profile distortion also varies for the different loading conditions. As the pressure drop across the screens increases, so too does the radial distortion. Again, this phenomenon can be explained by the non-uniform radial mixing resulting from spatial variation of the pressure gradient with the duct.

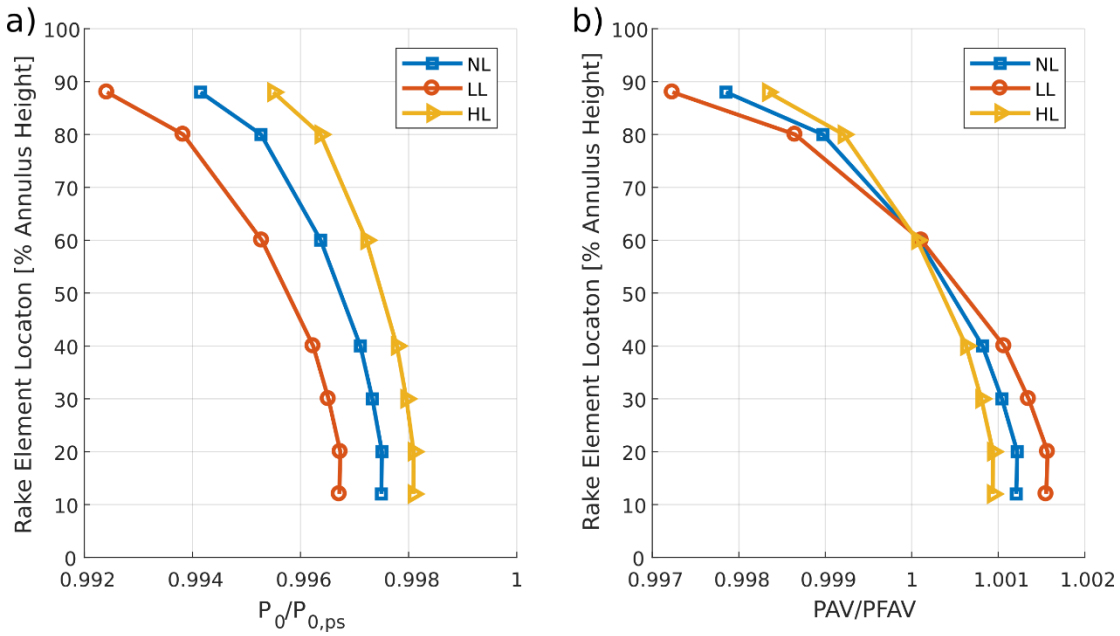

Figure 3-12 a) Radial Variation in Total Pressure, b) Profile Comparison at AIP – Loading Comparison

As per ARP-1420, the total pressure distortion can be reported using standardized distortion descriptors which are presented in section 2.5.2. A common method of reporting these descriptors is using bar charts as shown in Figure 3-13 for the nominal loading condition. Figure 3-14 shows the circumferential total pressure variation at nominal loading for varying radial positions. These charts are used to determine the circumferential intensity, the extent, and the location of max distortion as per the methodology prescribed in ARP-1420. These figures are included as an example of the post-processing technique used in this study.

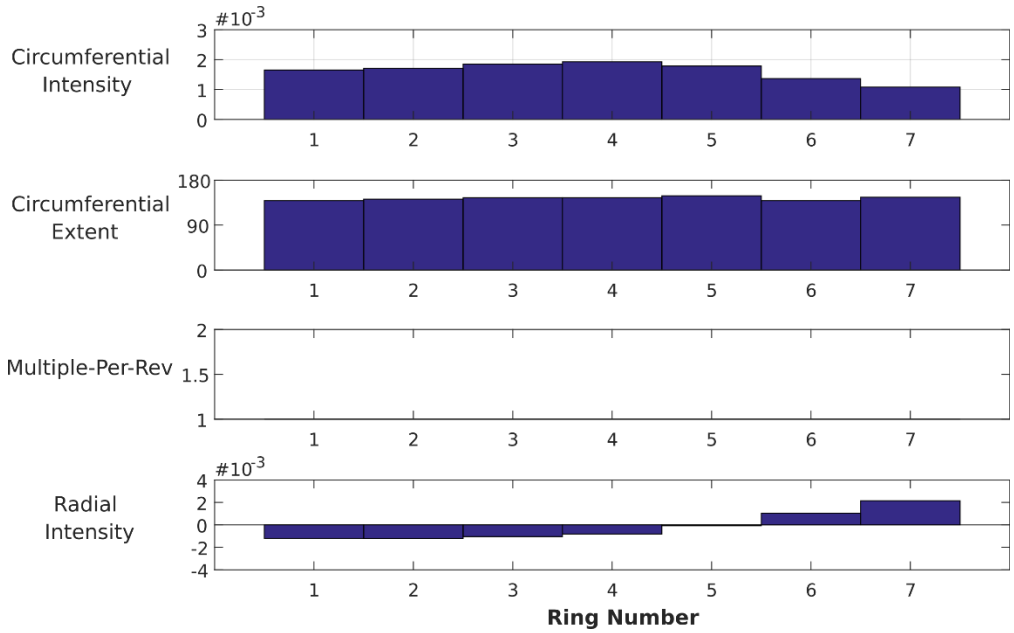

Figure 3-13. Distortion Descriptors Summary as per ARP-1420 at Nominal loading

In addition to the distortion descriptors, Table 3-1 provides a quick summary of the distortion magnitudes and the circumferential extents achieved in this study.

Table 3-1. Summary of Distortion Magnitude and Extent

Condition	Max Distortion %[1]	Circumferential Extent[2]
Nominal loading (NL)	0.42%	144°
Low-Loading (LL)	0.56%	144°
High-Loading (HL)	0.32%	145°

[1] See Eqn. (2.22)
[2] Area-averaged as per Table 2-1

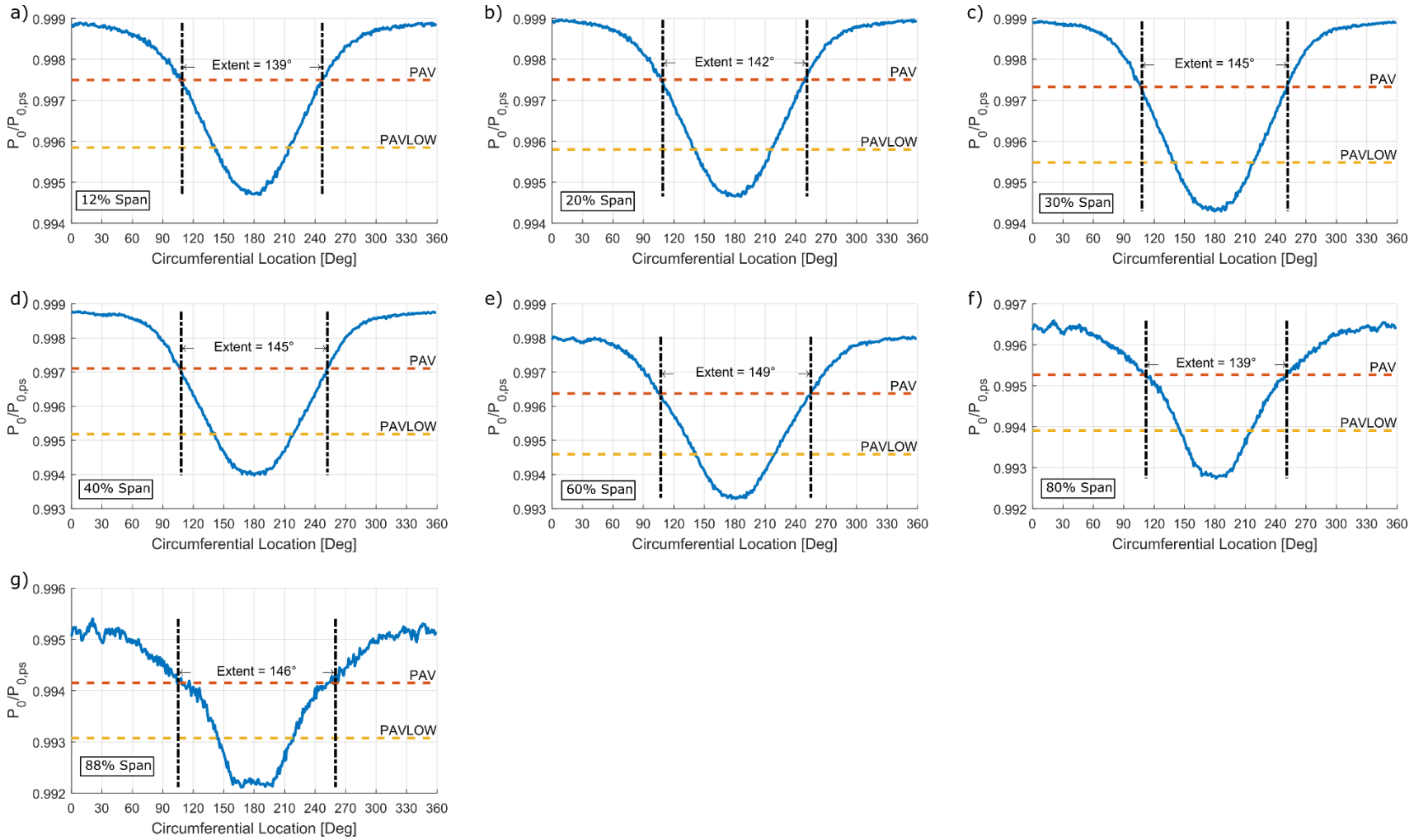

Figure 3-14. Sample Circumferential Distortion Charts as per ARP-1420 at a) 12% b) 20% c) 30% d) 60% e) 80% f) 88% Span - Nominal Loading

3.5 AIP Turbulence Measurements

This section presents results of thermal anemometry velocity and turbulence intensity measurements acquired at the AIP for three compressor operating conditions. Turbulence intensity characterization is an important part of properly defining inlet flow boundary conditions for CFD simulations. In the absence of any circumferential flow distortion, turbulence intensity should vary only in the span-wise direction.

As discussed, a circumferential total pressure distortion will inevitably be accompanied by some degree of non-uniform turbulent mixing which acts to equalize the pressure difference in the duct. Furthermore, recall that turbulence and flow instabilities can also be caused by the distortion screens themselves; specifically, the random interaction between coalescing jet flows. In this study, an attempt was made to mitigate the introduction of excessive flow unsteadiness by using multiple screens of varying porosity instead of a single low porosity screen. Furthermore, the screens were mounted upstream of a honeycomb carrier, which acts to promote flow straightening and jet flow coalescence.

To fully characterize the turbulence intensity at the AIP, both radial and circumferential traverses were performed to study the spatial variation. Set-up and calibration of the hot-wire is detailed in section 2.5.3. The hot-wire traverses for all three compressor conditions were performed on the same day during the same run. Ambient temperature variation during the entire hot-wire data acquisition remained within the tolerance of the temperature correction correlation. Steady compressor data were also recorded simultaneously and compressor corrected speed checks were performed prior to recording hot-wire data. The temperature of the flow for each hot-wire measurement is approximated by the middle rake element of the AIP total temperature rake, which is simultaneously recorded.

Similar to the total pressure field characterization procedure discussed in section 2.5.2, the distortion screen is rotated relative to the fixed hot-wire probe, which was positioned at 50% span for all measurements. A 120 point, 3° increment traverse was performed at the nominal loading operating condition. For high-loading and low-loading conditions, 60

point, 6° increment traverses were performed. Since these loadings were deemed to be secondary objectives, the traverse resolution was reduced to shorten compressor run time.

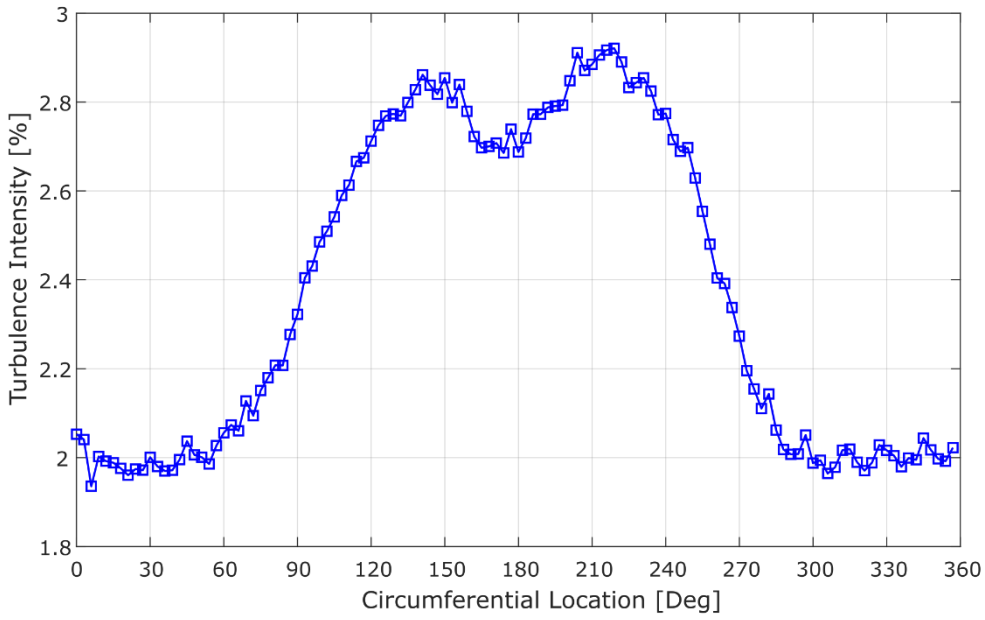

Figure 3-15. Hot-Wire Turbulence Intensity Measurement at 50% Span – Nominal loading

The circumferential variation in turbulence intensity at 50% span at the AIP for the nominal loading operating condition is shown in Figure 3-15. Turbulence intensity was calculated using the procedure outlined in section 2.5.3. The hot-wire probe was sampled at 200,000Hz for a total of 1.2 million samples for each measurement.

Figure 3-15 shows a nearly 1% variation in turbulence intensity between distorted and undistorted regions with an average intensity of 2.38%. The variation is symmetric about the BDC which corresponds to location maximum total pressure distortion, however, this location does not also correspond to the peak turbulence intensity. Rather, there two nearly symmetric peaks in turbulence intensity that occur at roughly 30° to either side of BDC. Recall that a total pressure distortion is a flow velocity distortion. Flow inside the distorted region has a lower velocity compared to the undistorted flow. Therefore, the spike in

turbulence intensity may be indicative of the mixing occurring in the transition region between the low and high velocity regions.

Figure 3-16 shows the variation in normalized velocity at the AIP measured using the hot-wire probe at 50% span for the nominal loading operating condition. The velocity at each circumferential location was obtained by averaging the velocity of all 1.2 million samples for each measurement. The velocity was then normalized by the average of all circumferential locations.

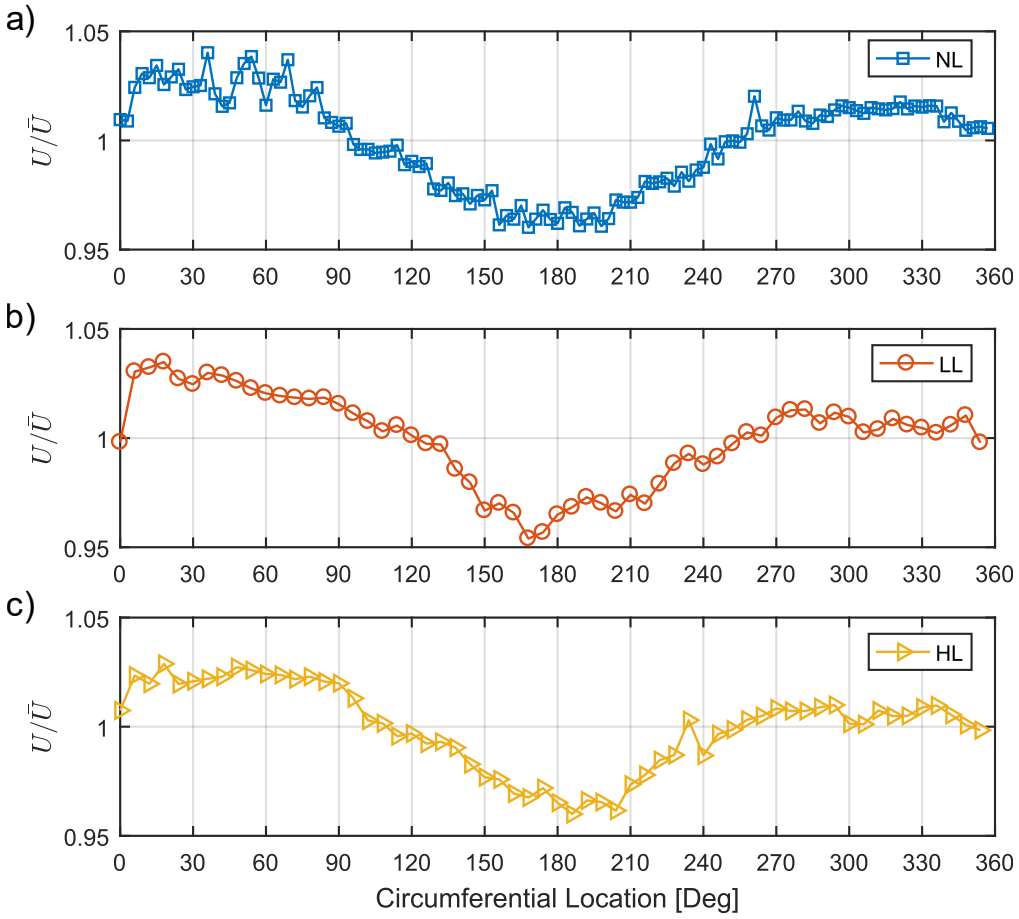

Figure 3-16. Hot-Wire Normalized Velocity Measurement at AIP – a) Nominal Loading b) Low Loading c) High Loading

The lack of symmetry in Figure 3-16 is most likely attributed to the long data acquisition time between the first and last measurement. Despite the use of the temperature correction

relation, there still exists significant error in measurements taken over long periods of time. Furthermore, a second post-run calibration of the sensor revealed that the probe had not been damaged or contaminated during the data acquisition. Velocity variation is presented here for the purposes of discussion since the trends still provide valuable insight, however, the velocity data should not be utilized to for boundary condition definition. To improve the accuracy of velocity measurements, the time between the start and end of the data acquisition should be reduced to minimize ambient condition variation between measurements. This can be achieved by reducing the resolution of circumferential traverse. Velocity measurements were secondary objectives for this investigation and are included here for discussion purposes to aid in the design of future experiments.

Despite the lack of symmetry, the shape of the circumferential velocity curve is similar to the total pressure variation near mid-span presented earlier in Figure 3-7 and Figure 3-13. Specifically, the circumferential location of the sloped transition regions between the high and low velocity regions agree for velocity, total pressure, and turbulence intensity measurements. This finding is true for all three compressor operating conditions. Furthermore, Figure 3-17 shows that the turbulence intensity profile appears to be independent of the inlet mass flow rate, and hence, independent of the magnitude of circumferential pressure distortion.

Figure 3-18 shows the corresponding rake area-averaged total pressure (PRAA) circumferential variation for the three inlet mass flow rates. Similar to the turbulence intensity, the change in mass flow rate causes a vertical translation and vertical stretching of the profile, but it does not affect the circumferential extent of the distortion. Therefore, the circumferential extent of the distortion does not appear to be a function of the compressor mass flow rate or the magnitude of pressure drop across the screen.

For the low-loading condition, the mass flow rate is highest resulting in the largest magnitude of pressure drop across the screen. However, an increase in distortion intensity does not appear to correspond to an increase in turbulence intensity. On the contrary, Figure 3-17 shows that the turbulence intensity is lowest for the low-loading condition and greatest

for the high-loading condition which has the slowest inlet velocity and smallest pressure drop across the screen.

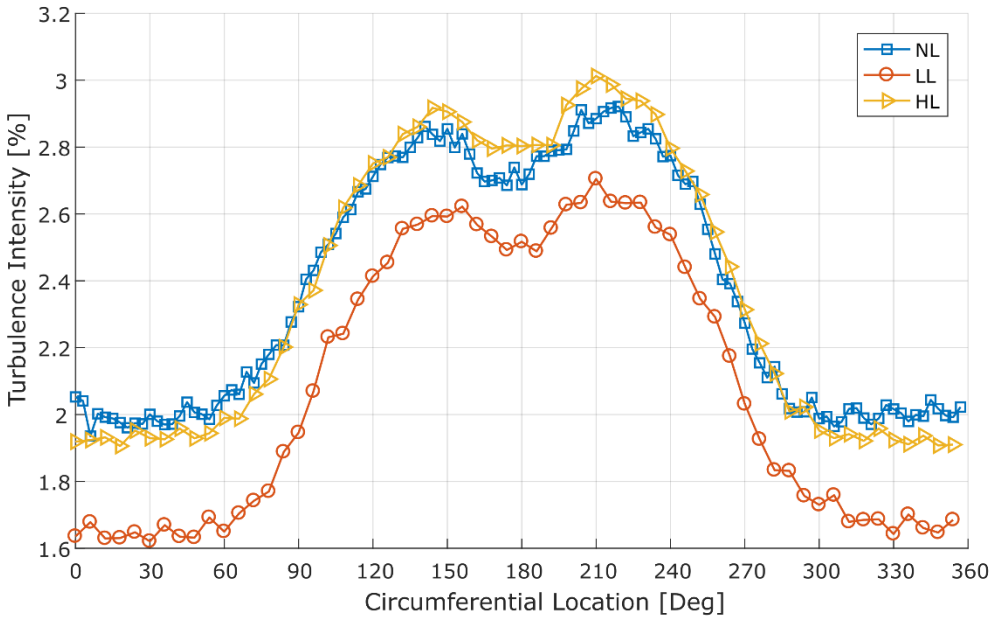

Figure 3-17. Comparison of Turbulence Intensity for Different Loadings

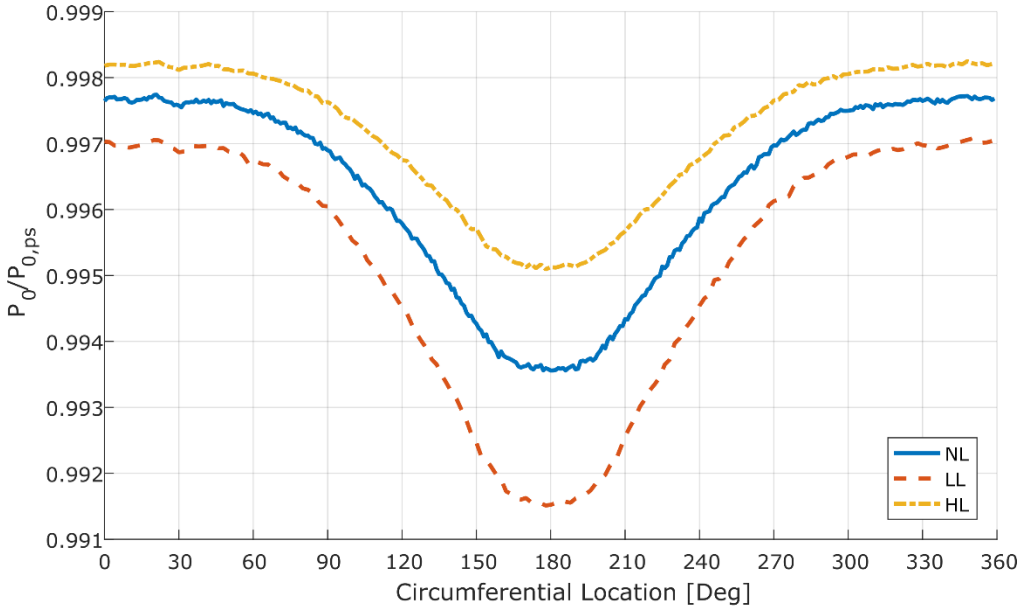

Figure 3-18. Comparison of Total Pressure Variation for Different Loadings

Radial variation in turbulence intensity was measured at four different circumferential positions which include TDC, BDC, 120°, and 240°. TDC and BDC were chosen because they represent profiles found inside and outside the least and most distorted regions, respectively. The remaining two positions were selected to be at the location of the distortion screen boundary and represent radial profiles in transition regions. The distortion screen was rotated to the appropriate orientation relative to the hot-wire probe and the L.C. Smith probe position was used to perform a 22-point radial plunge between and 8% and 92% span. Selected span points were biased towards the hub and shroud to provide high resolution in regions closer to the boundary layer. The hot-wire probe was again sampled at 200,000Hz for a total of 1.2 million samples for each measurement.

Figure 3-19, Figure 3-20, and Figure 3-21 show the resulting turbulence intensities and radial velocity profiles at the four locations investigated for nominal loading, low loading, and high loading, respectively.

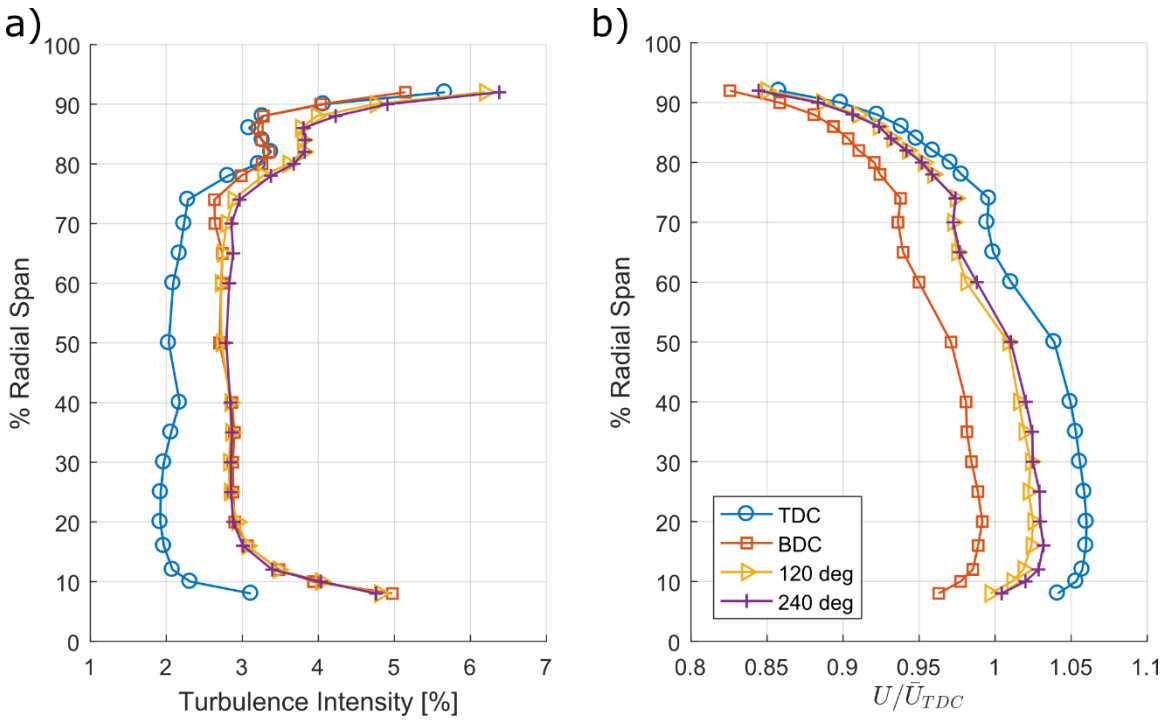

Figure 3-19. Radial Variation in a) Turbulence Intensity b) Velocity at AIP – Nominal Loading

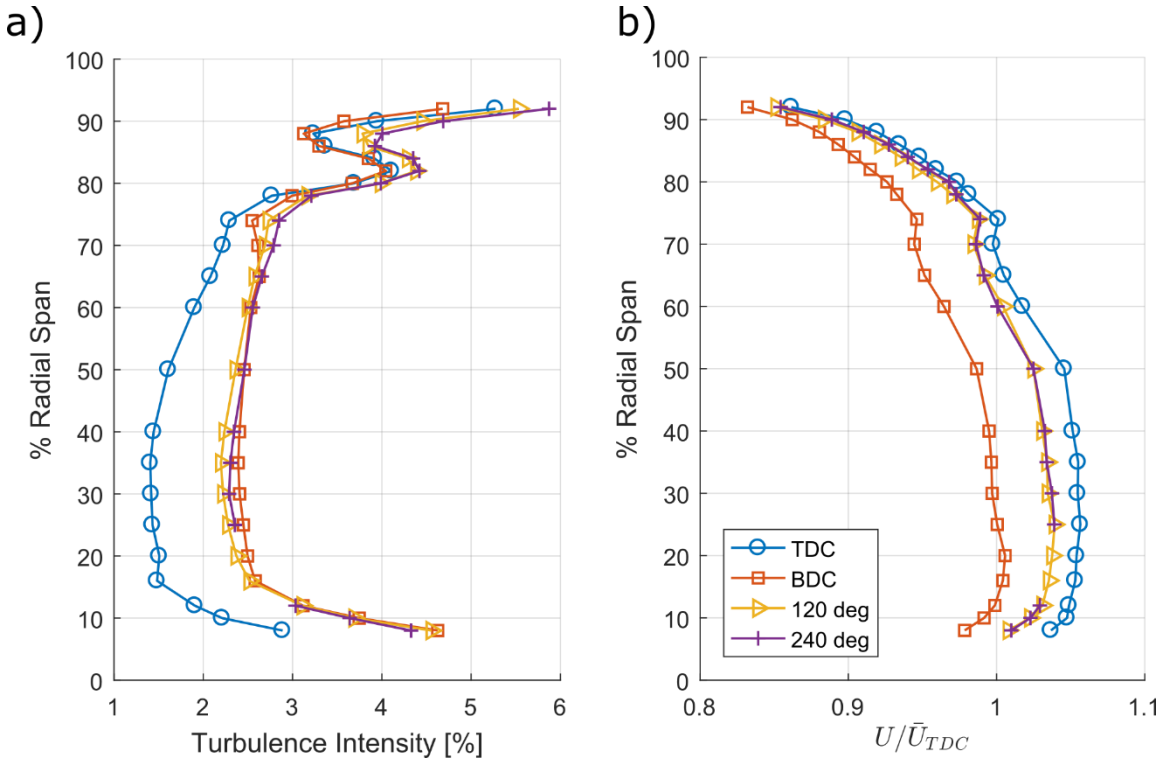

Figure 3-20. Radial Variation in a) Turbulence Intensity b) Velocity at AIP – Low Loading

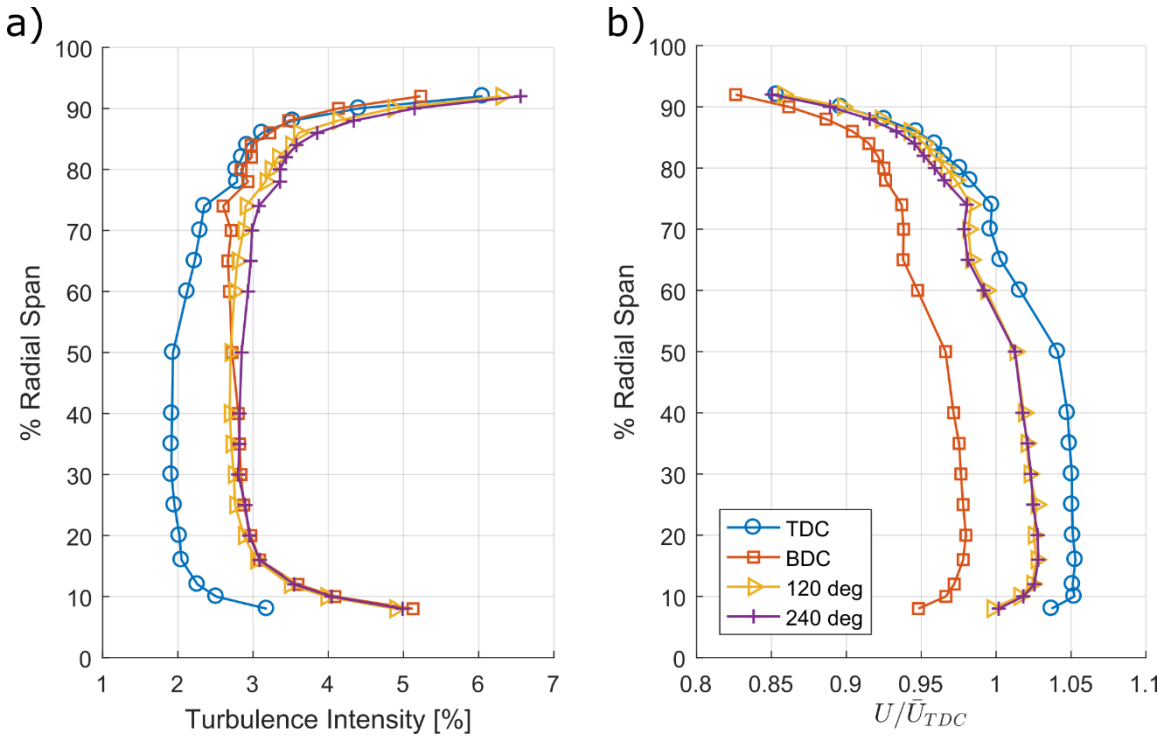

Figure 3-21. Radial Variation in a) Turbulence Intensity b) Velocity at AIP – High Loading

The turbulence intensities at 50% span, shown in Figure 3-17a, agree with the findings of the circumferential traverse. The velocity distribution, shown in Figure 3-17, shows a profile that is very similar to the total pressure profile measured by the Kiel-head rakes at the AIP. Furthermore, the agreement between the 120° and 240° profiles further demonstrates the symmetry of the distortion being investigated.

An interesting finding is the behavior of the 120° and 240° profiles, which will from here on out referred to as the transitions zone profiles. From 8% to 50%, the transition zone profiles almost identically match the max distortion profile at BDC. Beyond 50% span, the transitions zone and max distorted profiles begin to diverge and the BDC profile merges with the TDC profile at 80% span. This behavior is suggestive of the non-uniform radial mixing discussed in the previous section. The reduced turbulence intensity near the shroud for the BDC profile indicates that there is reduced mixing present in the tip region. This supports the hypothesis that non-uniform radial mixing in the distorted flow region leads to a minor radial distortion at the AIP which was shown previously in Figure 3-10.

A small spike in turbulence intensity occurs between 80% and 90% span for all three loadings. This spike could be an indication of boundary layer unsteadiness or fluctuating separated flow. The most prominent spike occurs for the low loading condition, which suggests that boundary layer unsteadiness at the tip is worsened with increasing mass flow rate. Boundary layer separation at the tip may be the result of a series of small internal ridges corresponding to the location of duct mating flanges.

In summary, the average turbulence intensities for the three inlet mass flow rates investigated are summarized in Table 3-2.

Table 3-2. Summary of Measured Turbulence Intensities

Condition	Average Turbulence Intensity
Nominal loading (NL)	2.38%
Low-Loading (LL)	2.09%
High-Loading (HL)	2.38%

3.6 Distortion Propagation and Attenuation Measurements

The following section presents the results of inter-stage total pressure measurements aimed at capturing the distortion propagation and attenuation from the AIP to the compressor exit. The experimental methodology for this investigation is discussed in detail in section 2.5.4. In summary, the flow passing through each vane passage is approximated using a single rake measurement positioned at a vane passage position located outside of the stator wake or potential. Past vane traverse studies on the PAX100 compressor have demonstrated that the total pressure between wakes is relatively constant. Therefore, a single measurement in this region serves as a reasonably good approximation of the bulk flow through each passage. Total pressure rake measurements were obtained at all inter-stage instrumentation locations between each blade and vane row as previously illustrated in Figure 2-3. Data were collected for nominal loading, low-loading, and high-loading compressor operating conditions.

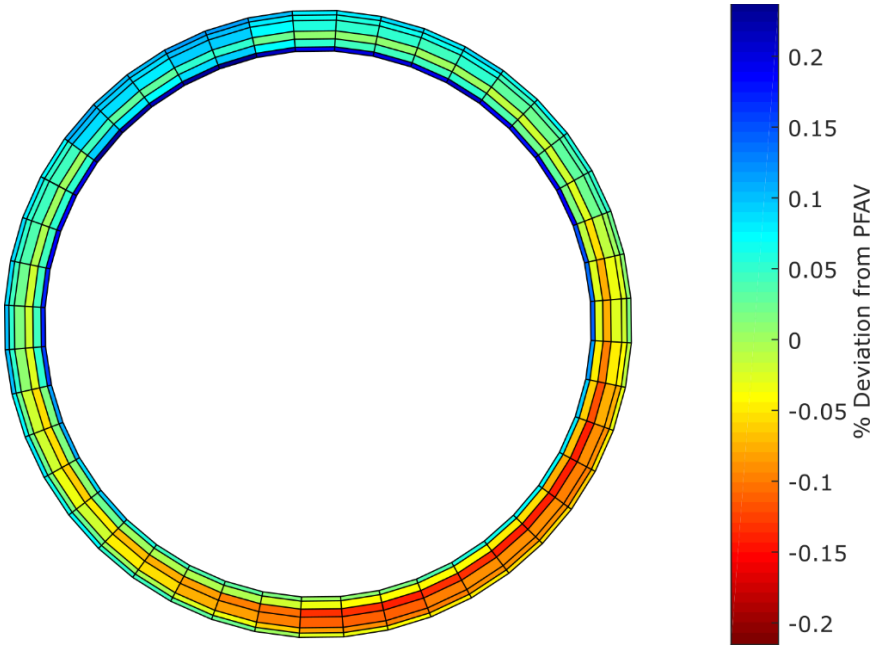

Figure 3-22. Sample Inter-Stage P_0 Measurement at S2 Exit – Nominal loading

Figure 3-22 shows an example of the total pressure rake data obtained downstream of stator 2. Each sector represents a single total pressure probe measurement. The size of each sector represents the area that is being approximated by that single measurement using this method. The flow field in reality is far more complex than what Figure 3-22 seems to

suggest as wakes are present, however, recall that the purpose of this measurement is simply to approximate the location and magnitude of the most distorted vane passage. For example, there is a clear circumferential non-uniformity between measurements in passages near TDC and BDC downstream of stator 2 which can be used study the global behavior of the low-pressure region as it passes through each stage.

Studying individual rake elements can be misleading since they give only small indication of a very complicated flow pattern downstream of rotors and stators. Therefore, studying a rake area averaged value, PRAA, for each stator passage provides a more meaningful approximation of the bulk flow. The circumferential variation of rake area-averaged total pressure is shown for each inter-stage measurement location in Figure 3-23 for the nominal loading operating condition. Similar charts showing the post-processing techniques for low-loading and high-loading can be found in Appendices A1 and A2, respectively.

Figure 3-23 shows that the circumferential variation becomes increasingly erratic for later stages, which is expected due to the progressively more complicated flow patterns that result from downstream wake interactions and the attenuation of the distortion. Therefore, the magnitude of the circumferential variation approaches the uncertainty of the measurement making it more difficult to distinguish the distortion from fluctuations due to measurement uncertainty. Despite this, a low-pressure distortion is still identifiable even at the compressor exit station. The extent of the distortion at each station was calculated using a method similar to that used at the AIP. The distorted region is that which falls below the face averaged pressure, PFAV. The beginning and end of the distorted region is demarcated by two black vertical dashed lines. To improve the approximation of the extent, the beginning and end of the distorted region are each offset by half a vane increment. The midpoint of the distorted region is identified by green vertical dashed lines. The midpoint is used to track the approximate center of the distortion for this study. Due to the erratic nature of the curve in the latter stages, using the location of the minimum rake area-averaged total pressure (PRAA) can provide misleading results. The data processing method presented here was chosen since it best fit the data and most readily lent itself to automation and, hence, to repeatability for data processing.

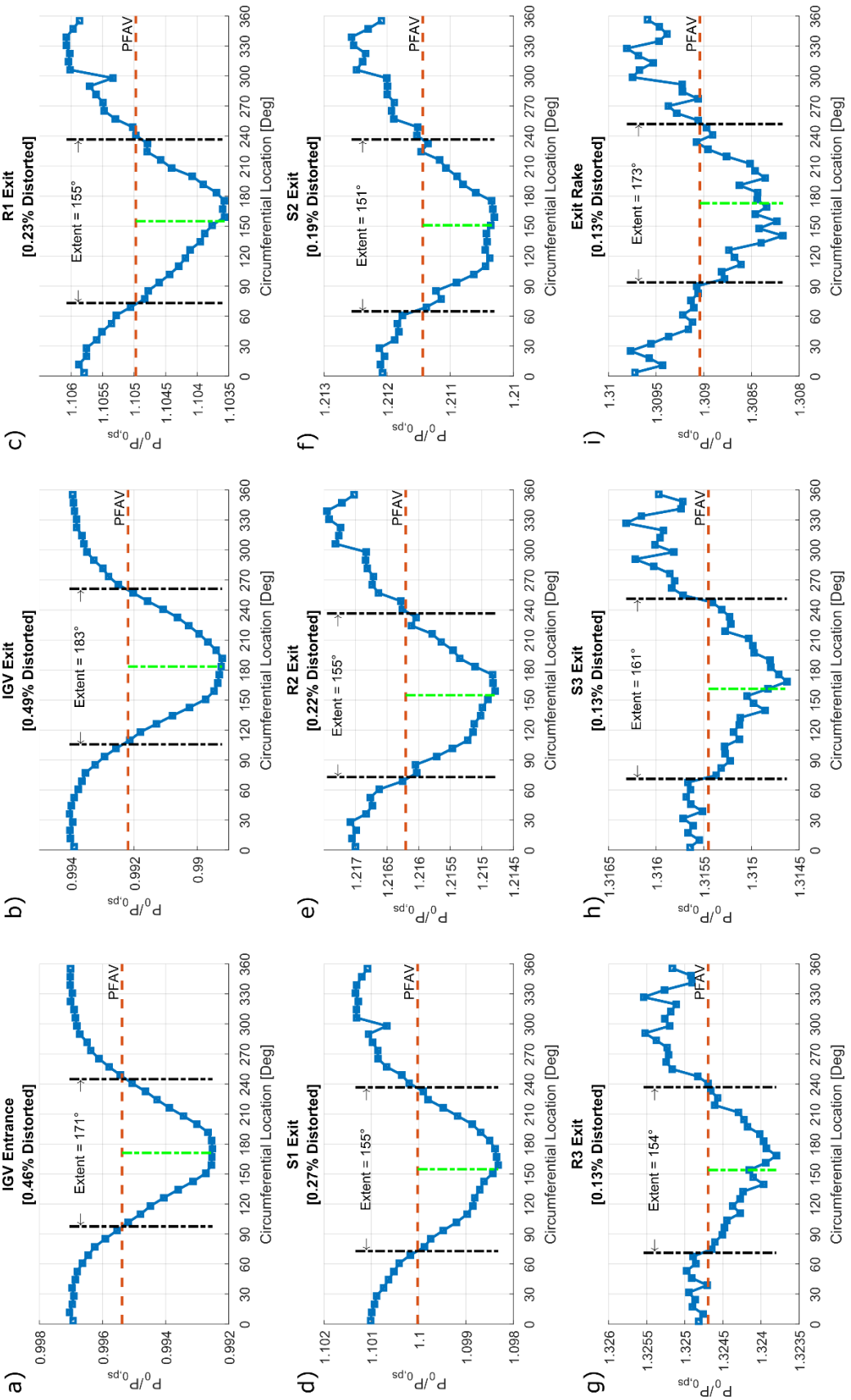

Figure 3-23. Circumferential Variation in Inter-Stage PRAA at a) IGV Entrance, b) IGV c) R1 d) S1 e) R2 f) S2 g) R3 h) S3 Exits and i) Exit Rake – Design Point

Using the results shown in the circumferential distortion figures, the maximum distortion percentage was calculated using equation (2.22). The maximum distortion intensity through the compressor is shown for all three compressor loading conditions in Figure 3-24.

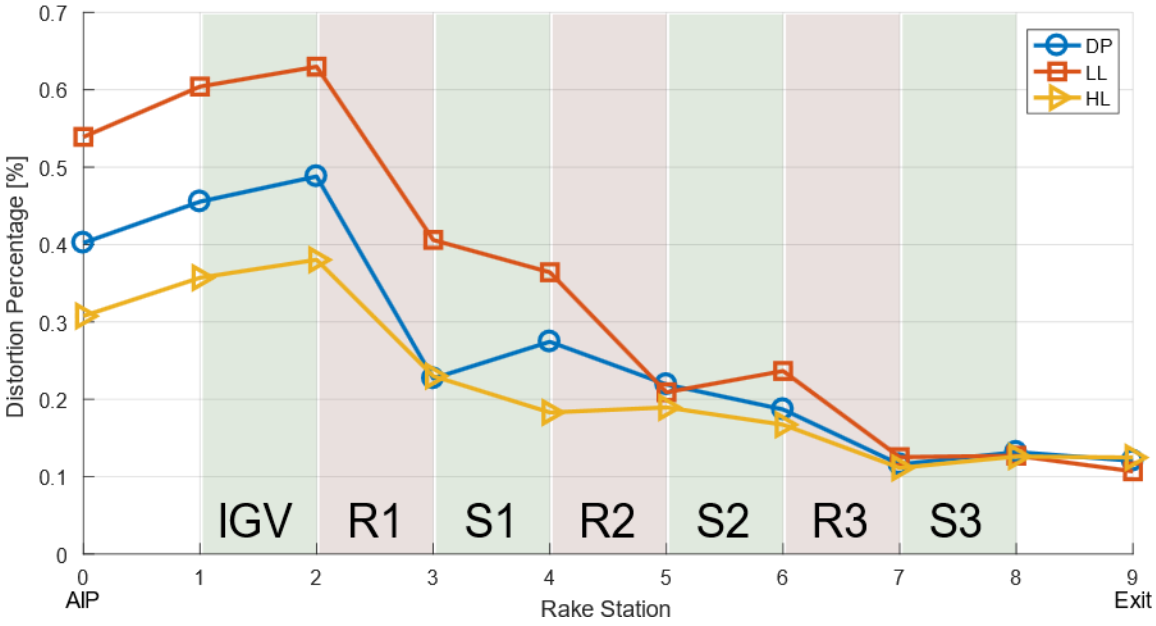

Figure 3-24. Distortion Intensity Attenuation

The distortion magnitude at the AIP for a given distortion screen is proportional to the square of velocity for a fixed screen loss coefficient. Hence, the low-loading condition produces the greatest distortion at the AIP followed by nominal loading and high-loading. The distortion intensity increases linearly until the IGV exit and is afterwards attenuated after each compressor stage. An interesting finding is that all three lines eventually converge to the same distortion level downstream of rotor 3. This suggests the amount of attenuation per stage is not constant for all distortion magnitudes. The attenuation-per-stage adjusts to provide the same distortion intensity at the exit regardless of the distortion intensity at the inlet. This observation is similar to one made by Roberts et al. (1968) discussed in section 1.3.4. Roberts concluded that the attenuation-per-stage adjusted to give the same distortion magnitude at the final stage regardless of the number of upstream stages in the machine.

In keeping with studies discussed in section 1.3.4, there is a nearly linear trend in the attenuation across the stages. The majority of the attenuation in distortion intensity occurs across the rotors while the stators appear to have a minimal impact. Plourde and Stenning concluded that the major factors contributing to total pressure distortion attenuation are the slope of the pressure rise versus velocity characteristic, resistance to crossflows, compressor length-to-radius ratio, and the multiple-per-rev of the distortion (Plourde & Stenning, 1967). Recall the effects of a total pressure inlet distortion on compressor operating point illustrated earlier in Figure 1-5 in section 1.3.3. The lower total pressure, lower velocity distorted flow region causes an increase in blade loading due to an increase in incidence angle. Therefore, the work input and resulting pressure rise of the distorted flow will be greater than the undistorted flow. In conclusion, this unequal circumferential work input and pressure rise results in an attenuation of the total pressure distortion across the rotor. As there is no work input across the stators, there is minimal change in distortion intensity observed.

Another mechanism by which total pressure distortion is attenuated is via cross flows between distorted and undistorted regions. Multi-stage axial compressor flows are often assumed to be axisymmetric. However in practice, secondary flows cause circumferential cross-flows and radial mixing which can be substantial under certain conditions (Gallimore & Cumpsty, 1986). The stator passages in the PAX100 compressor are shrouded, and therefore, crossflow cannot occur between passages. Crossflow can occur in the empty space between the rotors and stators and via tip leakage flows in the rotor passages. Plourde & Stenning (1967) attribute the increase in crossflow to a static pressure imbalance upstream and within the compressor arising from the nearly constant static pressure boundary condition upstream of the compressor at the throttle. Figure 3-25 shows the static pressure inter-stage circumferential variation for the low-loading condition.

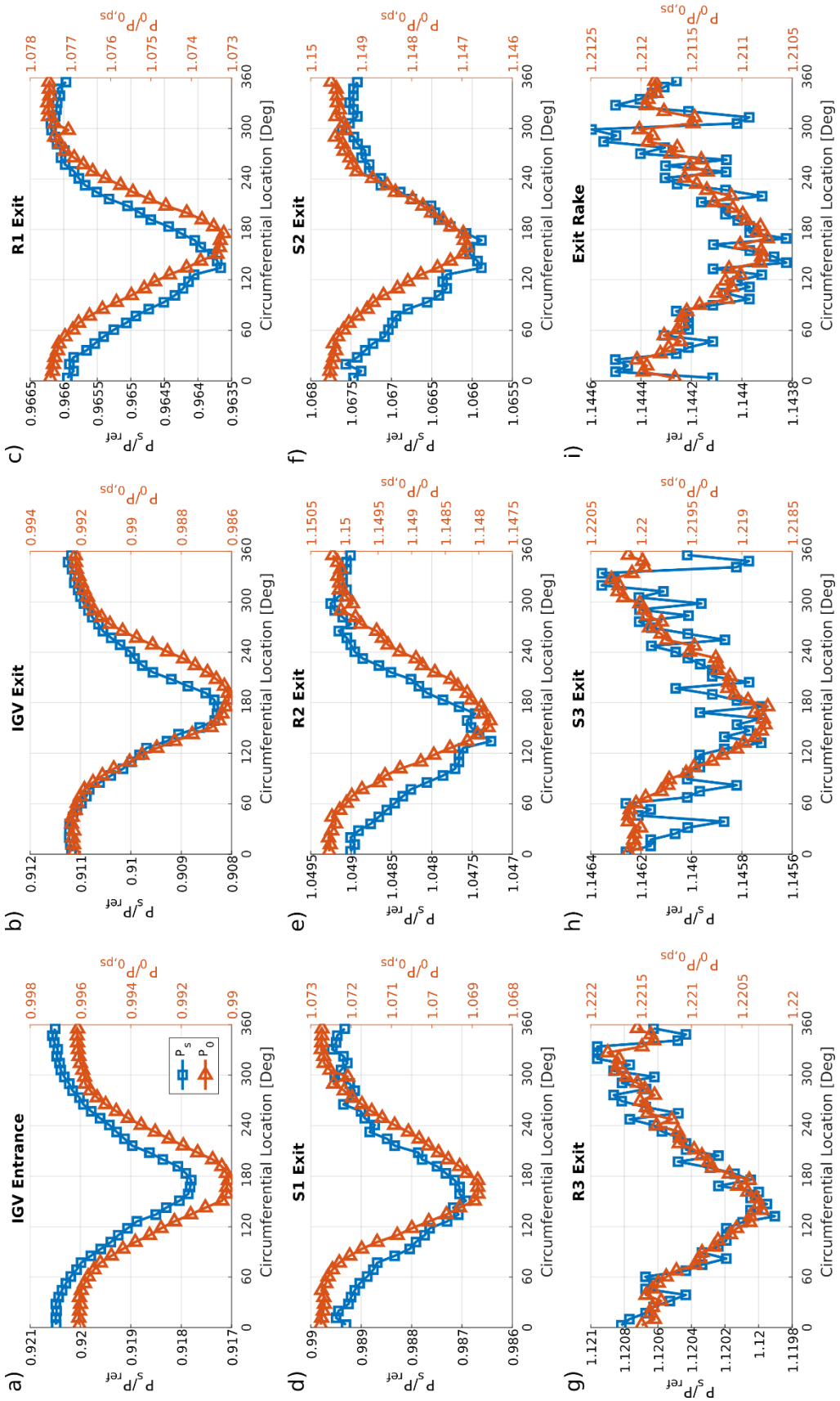

Figure 3-25. Circumferential Variation in P_s and Average P_0 at a) IGV Entrance, b) IGV c) R1 d) S1 e) R2 f) S2 g) R3 h) S3 Exits and i) Exit Rake – Low-loading

Also included in Figure 3-25 is the total pressure variation, which shows that the static pressure distortion and total pressure distortion are largely in phase throughout the entire compressor. These findings are in line with observations reported by Braithwaite & Soeder (1980) and Plourde & Stenning (1967). Although the magnitude of the distortion observed in this study is quite small, a clear distortion is evident especially in the forward stages of the compressor. Therefore, it is possible that this static pressure imbalance may promote an increased level of crossflow in the space between the rotor and stator. However, Plourde & Stenning (1967) concluded that cross-flows have very little impact on distortion attenuation for compressors with normal axial clearances. Further investigation would be required to study the degree of crossflow in the PAX100.

The dataset obtained from this study was also used to study the propagation of the distortion which is defined as the circumferential location peak distortion. As previously discussed, for this study, the centerline of distorted region is used in lieu of the maximum value. Figure 3-26 shows the propagation of the distortion from the AIP to the compressor exit for all three compressor loading conditions. A cascade view of the PAX100 compressor is overlaid to provide a reference for the relative size of stator and rotor passages. Recall that the data is comprised of two separate distortion traverses; one with 44 increments corresponding to stations 1 through 6, and one with 50 increments, corresponding to stations 6 through 9.

The distortion centerline remains close to the bottom-dead-center position at all stages and does not seem to be influenced significantly by the spin direction of the rotor. This suggests that there is no significant circumferential propagation of the peak distortion. The small variations by up to two passages are likely attributed to shortcomings of the single rake position approximation of the passage flow which cannot account for pressure redistribution within the vane passage. Furthermore, as shown in Figure 3-23, the distortion centerline becomes increasingly difficult to estimate due to the attenuation in the rear stages of the compressor. In conclusion, the circumferential propagation of the distortion seems to remain in phase with the static pressure distribution, shown in Figure 3-25, which remains centered about bottom-dead-center position at all stages.

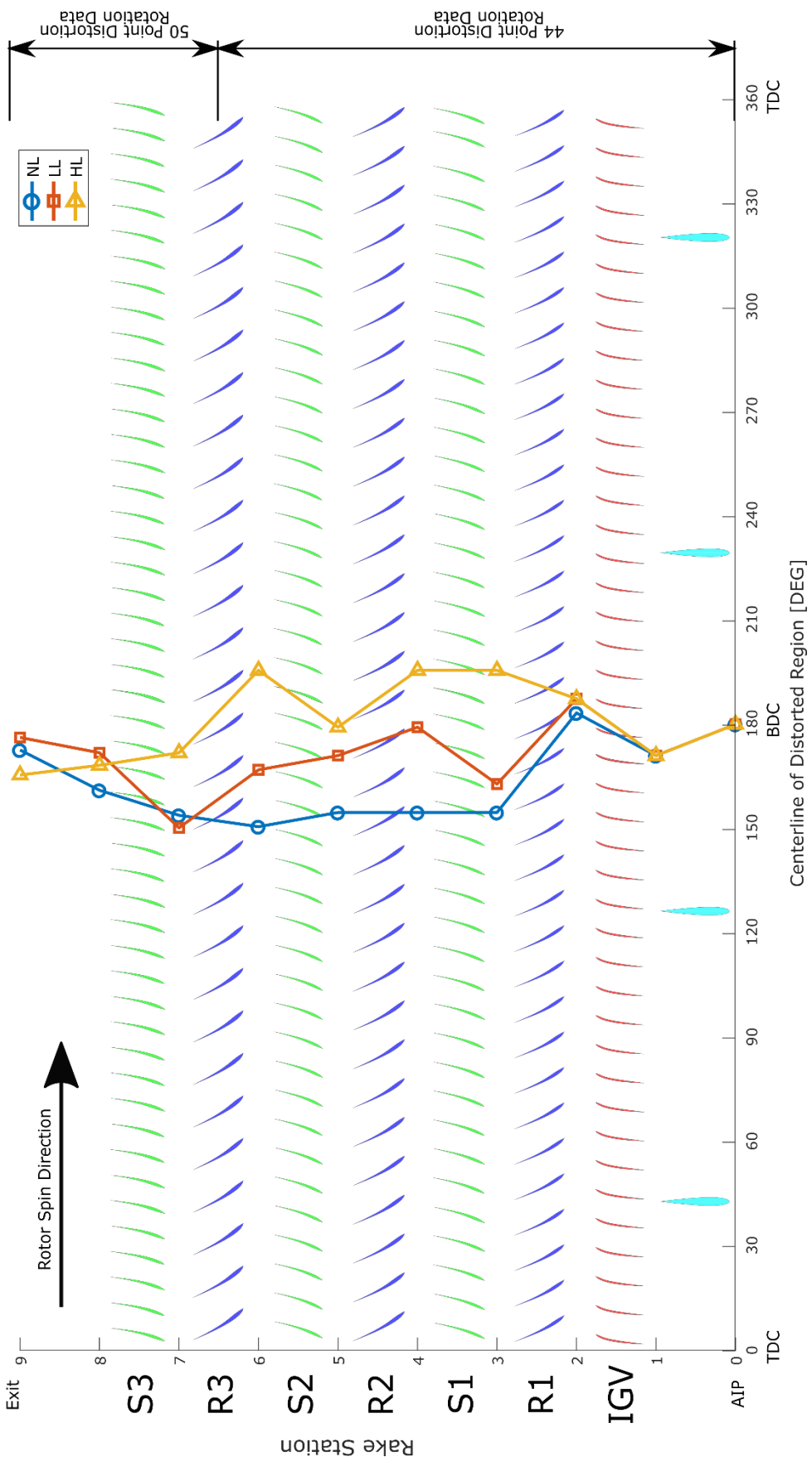

Figure 3-26. Distortion Centerline Propagation

3.7 Inter-Stage Flow Field Characterization

This section presents the results of the full annulus inter-stage flow field characterization at the stations downstream and upstream of the IGV, S1 and S2. The experimental procedure is outlined in detail in section 2.5.5. Because of the large number of vane and distortion traverse combinations required to characterize an inter-stage total pressure field, only the stations upstream and downstream of the 44 vane passage IGV, S1, and S2 were characterized for this study.

Recall Figure 2-21 which illustrates the locations of the instrumentation rake relative to the vane passage and distortion screen. To characterize the flow field upstream and downstream of the 50 vane S3 would have required a separate data acquisition campaign with modified traverse parameters. The distortion would need to be traversed for 50 equal increments as opposed to 40 for each of the 20 vane passage positions resulting in a much longer data acquisition time. Furthermore, the distortion is greatly attenuated prior to the third stage such that the magnitude of the distortion approaches the fluctuations due to measurement uncertainty. Therefore, the final stage was not characterized in detail for this study.

Figure 3-27, Figure 3-28, and Figure 3-29 show the resulting full annulus total pressure fields downstream of the IGV, S1, and S2, respectively, for the three loading conditions investigated. The contours are created from a total of 880 circumferential rake measurements providing a measurement every 0.41°. With 7 total pressure probes per rake, a total of 6160 measurements were used to characterize each flow field.

These contours are included to illustrate the resolution that can be achieved using this data acquisition technique. Despite the small magnitude of the distortion, a circumferential non-uniformity is still evident between the bottom-dead-center and top-dead-center vane passages. Also visible are the 44 wakes corresponding to each stator vane. The scale and distribution of the color bar has been adjusted to accentuate the low-pressure regions and make more evident the presence of circumferential non-uniformities.

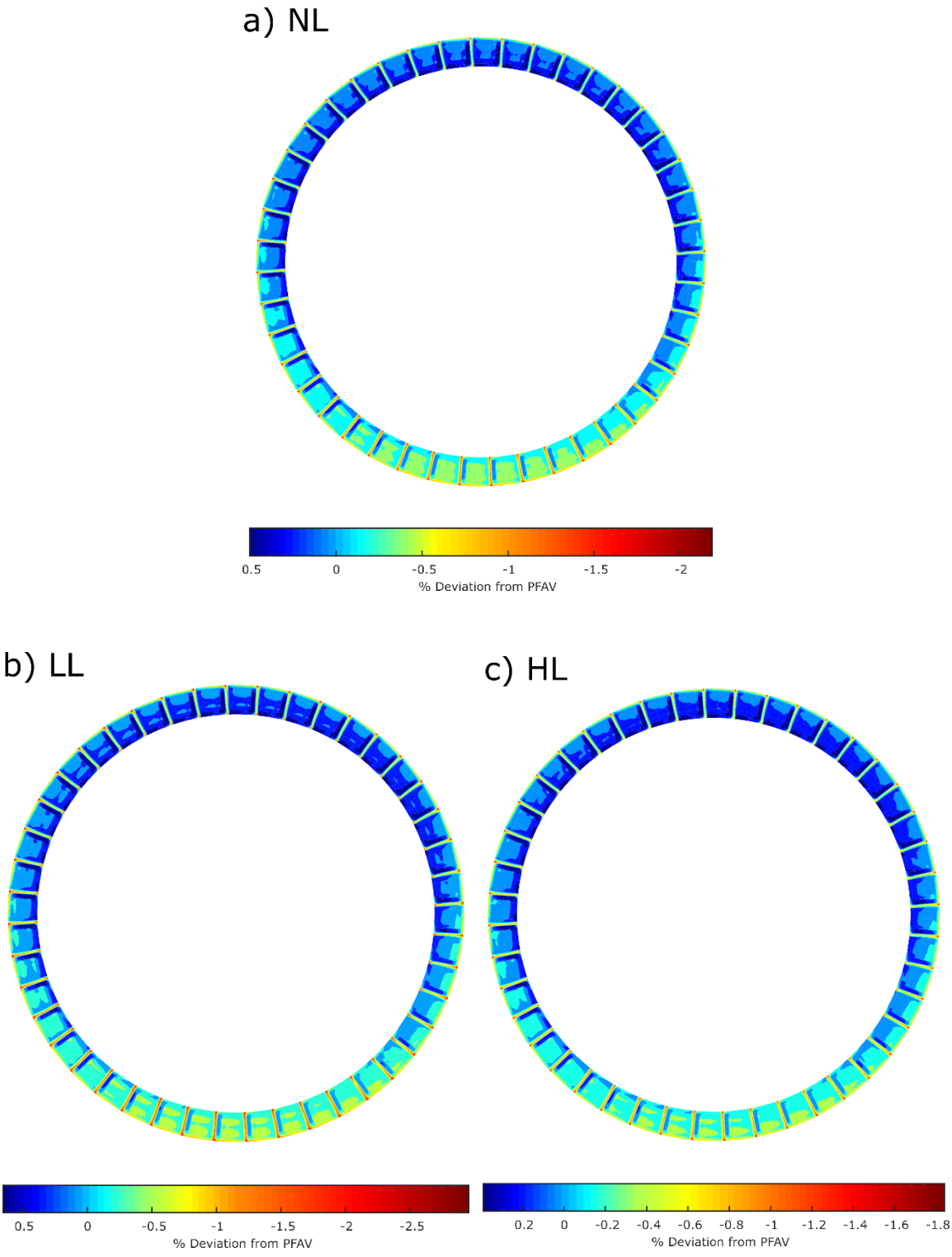

Figure 3-27. Total Pressure Field Downstream of IGV for a) NL b) LL c) HL

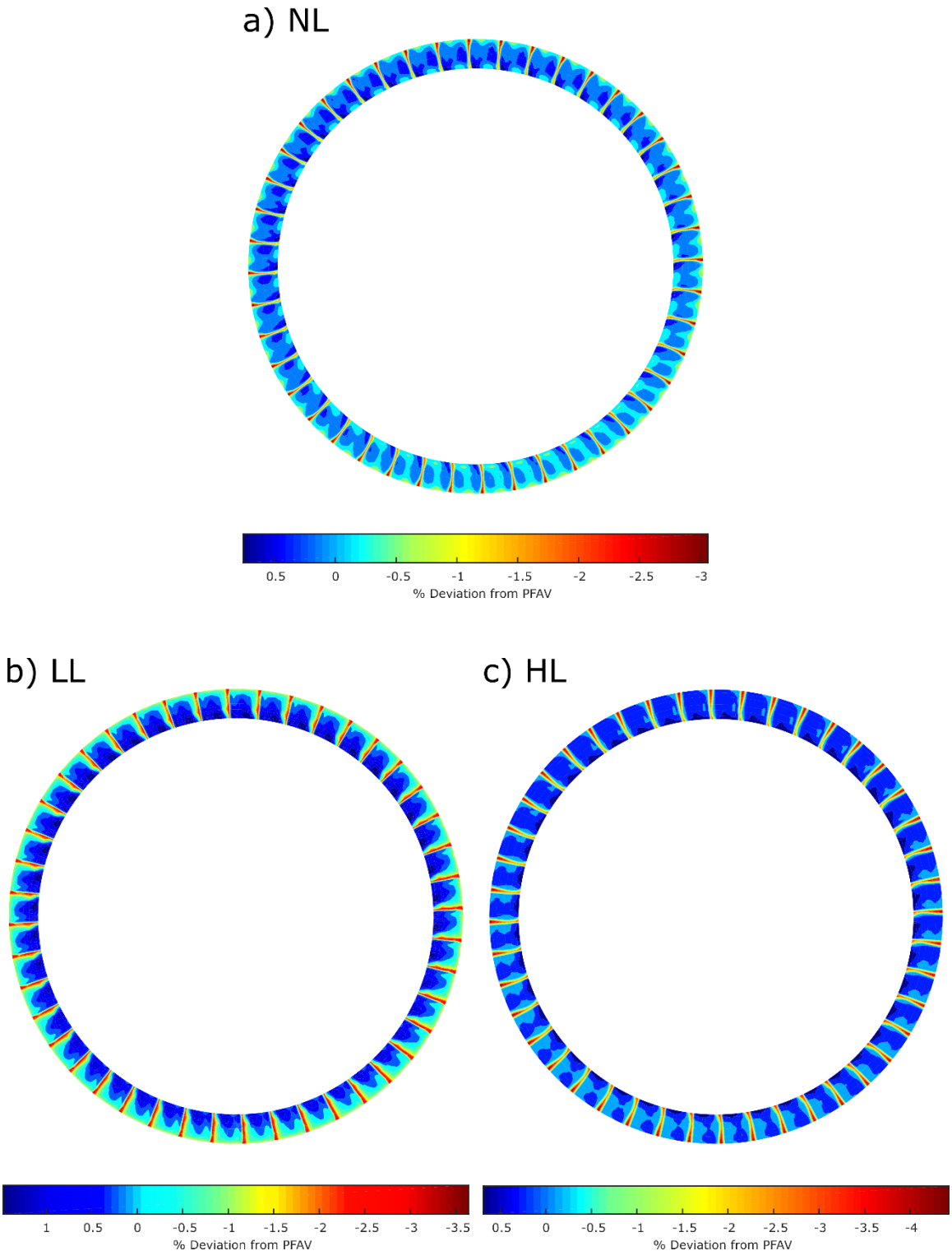

Figure 3-28. Total Pressure Field Downstream of S1 for a) NL b) LL c) HL

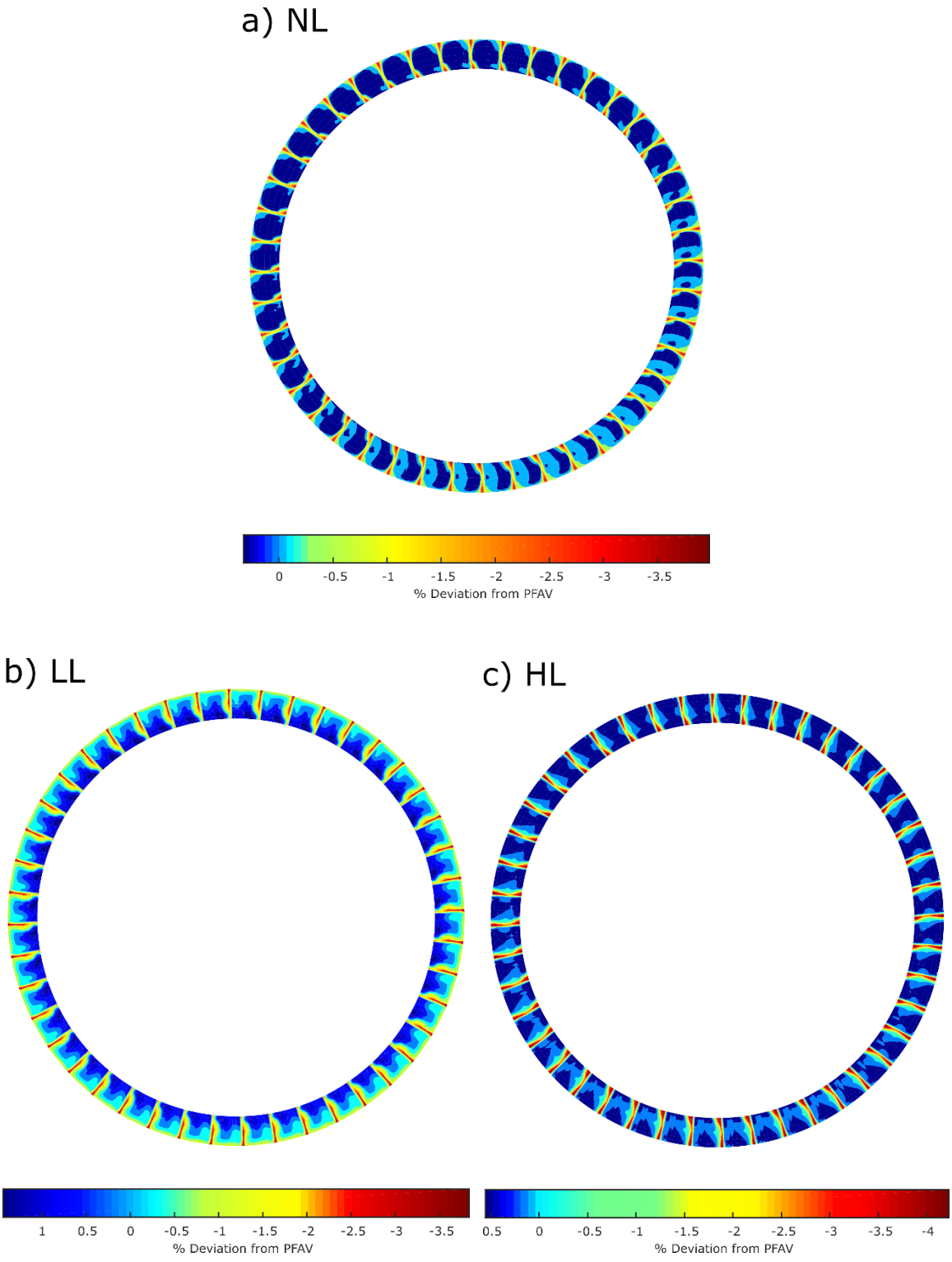

Figure 3-29. Total Pressure Field Downstream of S2 for a) NL b) LL c) HL

The total pressure field downstream of the IGV is relatively similar for the three loadings investigated. The lighter blue and green contours seen in the passages near bottom-dead-center are representative of the total pressure deficit propagating through the vane row. The only difference between the three loadings is the mass flow rate. Since the inlet flow upstream of the IGV is axial, the incidence angles are identical. Therefore, the only differences between the three loadings are the wake thicknesses which vary with changing Reynold's number due to a change in velocity. The total pressure outside of the thin wakes is relatively uniform within each passage which is indicative that secondary flows and loss mechanisms are minimal. Furthermore, the distortion shifts in a clockwise direction corresponding to the direction of the exit flow angle, which suggests that the distortion follows the direction of the IGV exit flow angle. This observation is in line with the distortion centerline propagation measurements shown in Figure 3-26.

Unlike the IGV, the inter-passage total pressure fields downstream of S1 and S2 are significantly different between the three loading conditions. Depending on the blade loading, the low total pressure regions seem to cluster in different regions of the vane passage. At nominal loading, the majority of the low total pressure regions are located at mid-passage and near the pressure surface. At low loading, the low total pressure regions are located more towards the shroud and pressure surface of the vanes. At high loading, a higher concentration of low total pressure is situated near the suction surface especially towards the hub and tip regions of the vanes. The differences in these plots are indicative of the various mechanisms by which the low total pressure distortion is propagated through each vane row for the different loading conditions.

Both the incidence and mass flow rates vary between the three loading conditions investigated. The incidence angle at nominal loading is closer to the design incidence of the vanes, which minimizes losses associated with incidence effects. This explains why the wakes appear thinner compared to the other two loading conditions, and there is less evidence of lower momentum secondary flows within the passages. The distorted flow regions, therefore, are centered within the passage and follow the bulk flow. At low loading, the wakes are larger towards the pressure side of the vane which is indicative of a

negative incidence angle. The low total pressure regions near the shroud are evidence of lower momentum flow regions which may be caused by secondary flow effects, such as passage vortices, which become more pronounced at off-design conditions. At high loading condition, the incidence increases, which again causes greater incidence losses leading to a larger separation wake on the suction surface of the vane.

In summary, the total pressure fields discussed provide evidence to suggest that the different secondary flows present at each loading influence the propagation of the distortion in a multi-stage environment. It is expected that for a larger magnitude distortion, the change in incidence circumferentially could lead to more substantial variation the in secondary flows observed within distorted and undistorted passages, which could result in different propagation behaviors. Flow angle measurements are recommended to further study the differences between the three loading conditions and identify the influence of secondary flows. The different mechanisms of distortion propagation may explain why the path of the distortion between loadings differs slightly in Figure 3-26.

Similar total pressure field contours can be generated using data measured downstream of the rotors. Although the total pressure measurement is an average of a highly unsteady rotor wakes, the resulting flow fields still show evidence of circumferential non-uniformities caused by the total pressure distortion. Figure 3-30 and Figure 3-31 show the resulting full annulus total pressure fields downstream of the R1 and R2, respectively, for the three loading conditions investigated.

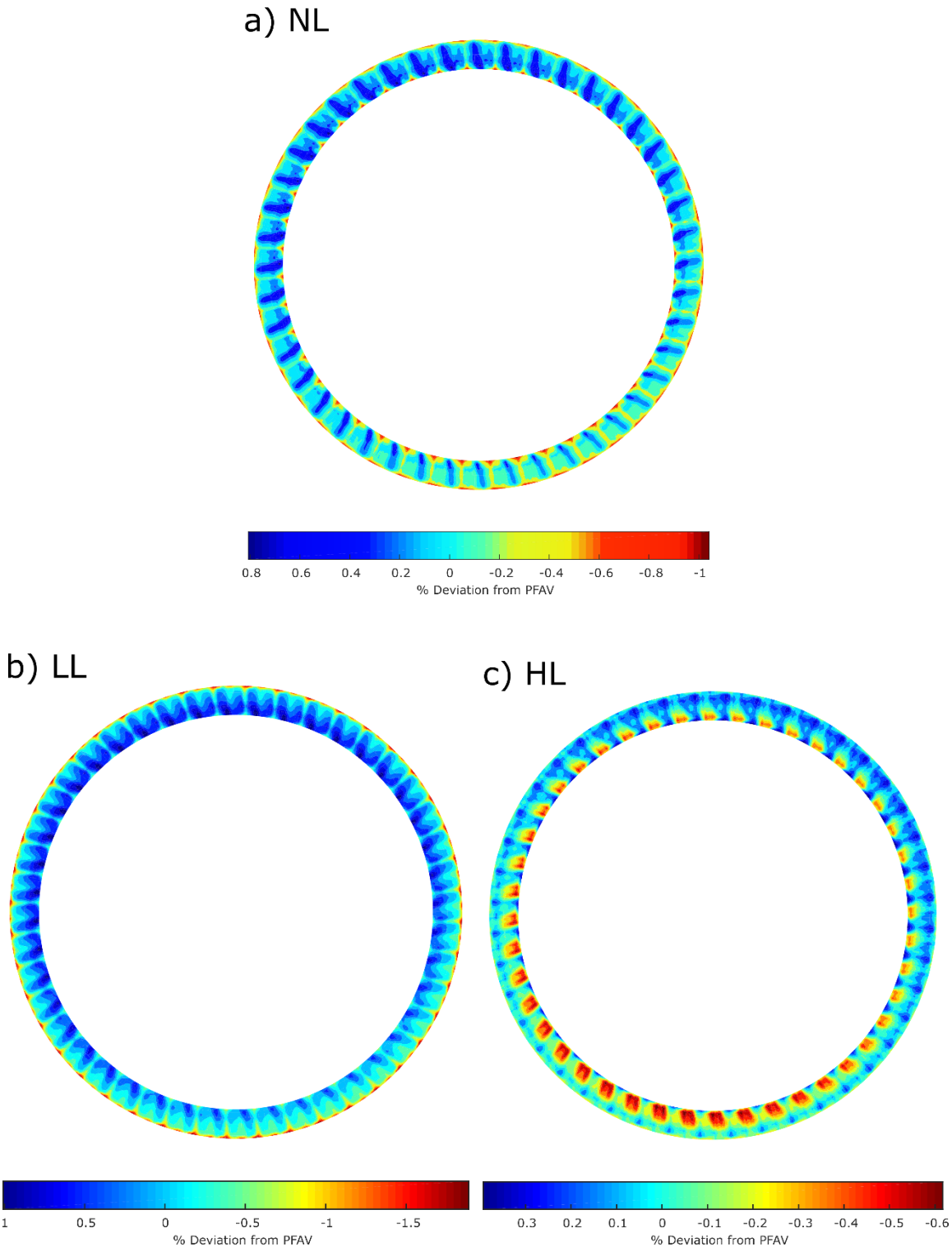

Figure 3-30. Total Pressure Field Downstream of R1 for a) NL b) LL c) HL

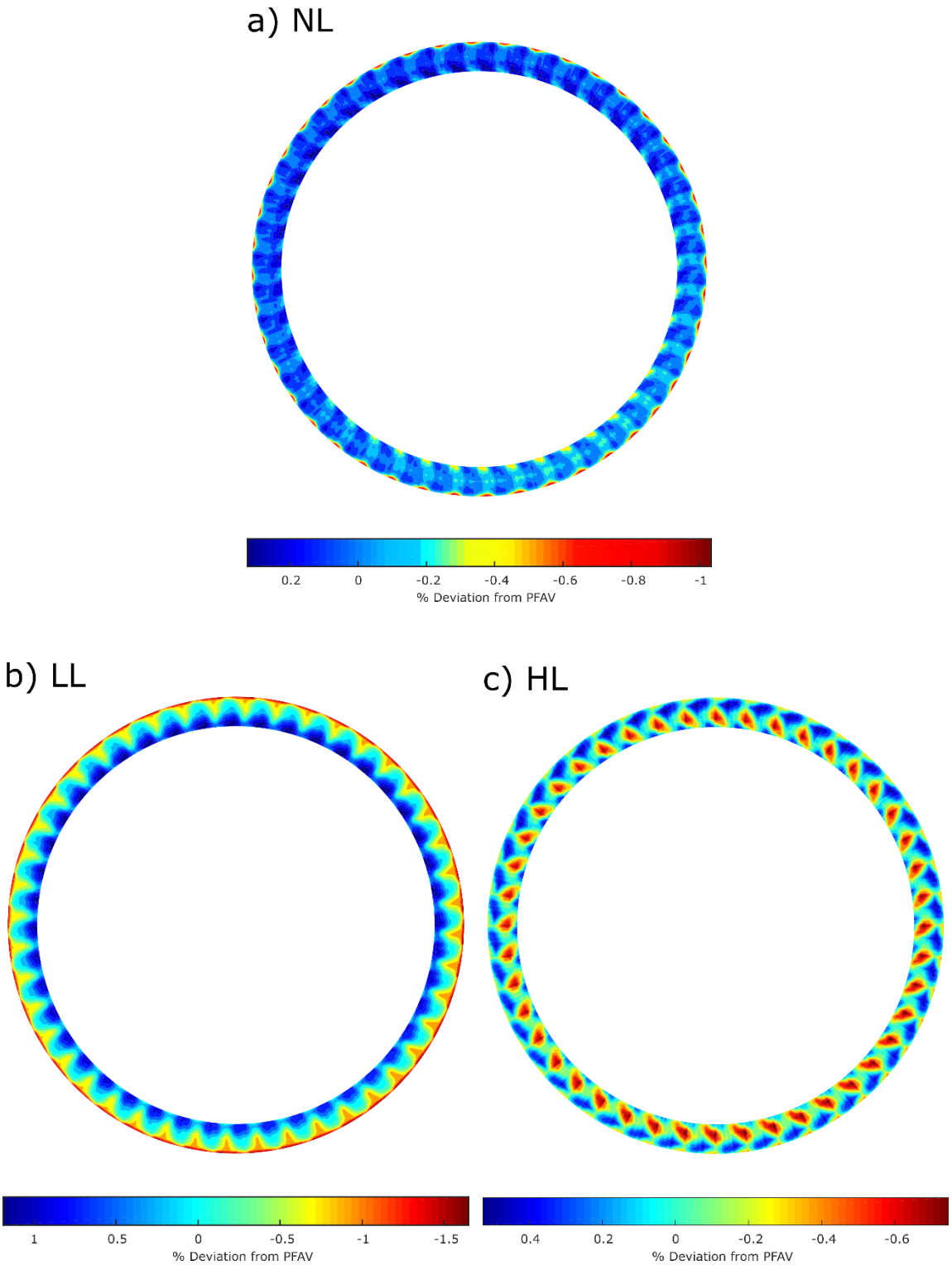

Figure 3-31. Total Pressure Field Downstream of R2 for a) NL b) LL c) HL

Studying the circumferential variation of the low total pressure regions provides insight into the behavior of the distorted flow as it passes through the rotor. The circumferentially cyclic total pressure patterns correspond to the leading edge potentials of the 44 vanes located immediately downstream of the instrumentation rakes. The total pressure field contours vary considerably between the three loading conditions signifying that, similarly to the stators, there are varying degrees of secondary flow effects present for each condition. The pressure field for nominal loading is relatively uniform whereas the fields for high and low loading show more substantial variation in total pressure within each passage. This is indicative of the increased significance of secondary flows at off-design loadings, which may affect the distortion propagation behavior.

The full annulus total pressure fields are compared to the earlier distortion propagation measurements presented in section 3.6. Recall that these measurements utilized a single vane passage location to approximate the bulk flow in each stator passage. The validity of this approximation is now assessed by comparing the single point measurements to a vane area-averaged total pressure, PVAA, calculated using the 20 measurements spanning one vane passage. The vane area-averaged total pressure gives a more representative measurement of the average total pressure for each passage since it includes both radial and circumferential variations and the effect of the stator wakes. The discretization of the annulus is done is such a manner that the vane average corresponds to the vane that was approximated by the single measurement in the previous section.

A comparison of the single rake area-average total pressure (PRAA) approximation and the vane area-averaged total pressure (PVAA) circumferential variation is shown in Figure 3-32 at nominal loading. The dashed lines represent the respective face average total pressure (PFAV) computed using each dataset. The two curves are in phase at all stages which indicates that the approximation method captures the location of the maximum distorted region well. Furthermore, the percent distortion calculated using the face average total pressure is consistently overpredicted by the single rake approximation with the overprediction increasing in the later stages. This discrepancy is likely due to the pressure drop in the wakes which increases in magnitude and circumferential span.

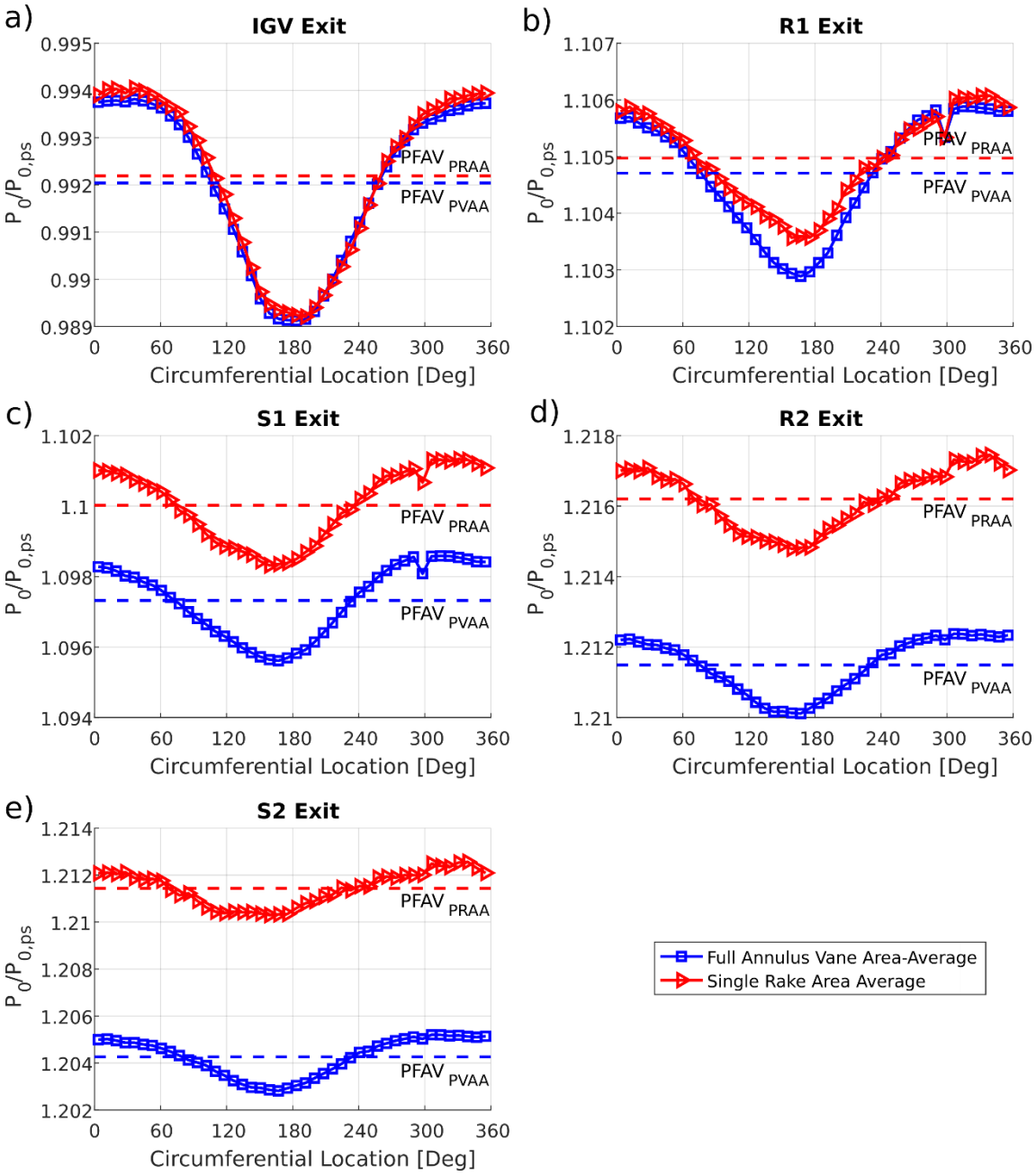

Figure 3-32. Comparison of Inter-Stage Distortion Characterization Methods at a) IGV b) R1 c) S1 d) R2 e) S2 Exits – Nominal Loading

The percent overprediction of face averaged-pressure using the approximation method is summarized for the IGV, S1, and S2 exit locations for nominal loading, low-loading, and high-loading in Figure 3-33. The high and low loading conditions both exhibit higher percent deviations compared to the nominal loading. This is indicative of the increased significance of the wakes in the downstream total pressure field. Despite the differences, the maximum observed overprediction is only around 1%. Given that the difference follows a nearly linear trend, the PFAV calculated using the approximate method may be adjusted for future studies using insights gained from the detailed full annulus characterization studies presented here.

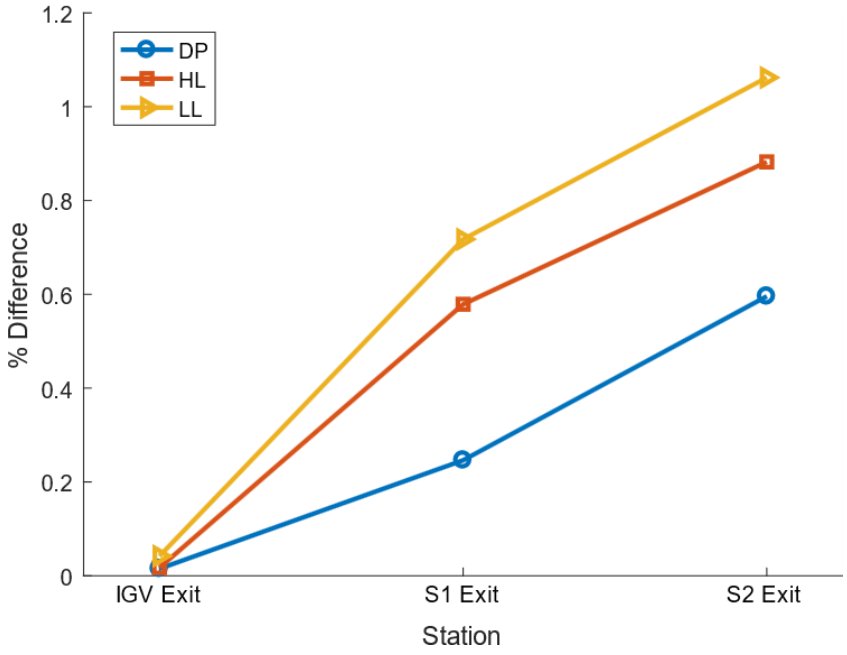

Figure 3-33. Percent Overprediction in PFAV due to Single Point Vane Passage Approximation

Figure 3-34 shows a comparison of the attenuation calculated using the full annulus data and the attenuation found using the single point passage approximation. Although the distortion magnitude is small, there appears to be a noticeable difference between the two measurements with the largest differences occurring downstream of the rotor. This is because the total pressure field downstream of the rotor is less uniform than the field downstream of the stators which makes approximation using a single rake position more

challenging. The magnitude of the distortion percentage and attenuation trend does not appear to be greatly shifted by the inclusion of wake data in the calculation. This indicates that the distortion affects both the passage and wake flow uniformly.

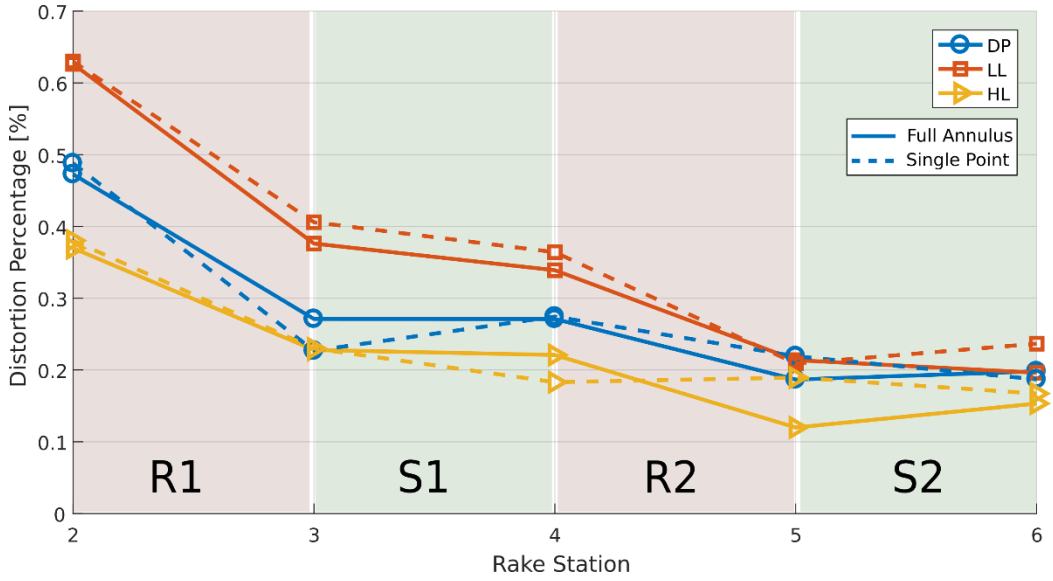

Figure 3-34. Comparison of Attenuation Measurement between Single Point and Full Annulus Measurements

The effects of the distortion on wake profiles downstream of the IGV, S1, and S2 are illustrated in Figure 3-35 at 50% span for the three loading conditions studied. The wake profiles shown are composed of 20 equally spaced measurements spanning one entire vane passage. At each pitch-wise location and loading, the top-dead-center and bottom-dead-center passages are shown, which represent an undistorted and distorted passage, respectively. The distortion at 50% span causes a nearly uniform shift in the total pressure profile with minimal effect on the profile shape. As discussed earlier, a total pressure distortion results in a change in incidence and vane loading, which should cause a corresponding change in the exit flow angle deviation due to incidence loss effects. The most noticeable evidence of a change in exit flow angle can be observed only at the 20% span location near the hub, which is shown in Figure 3-36.

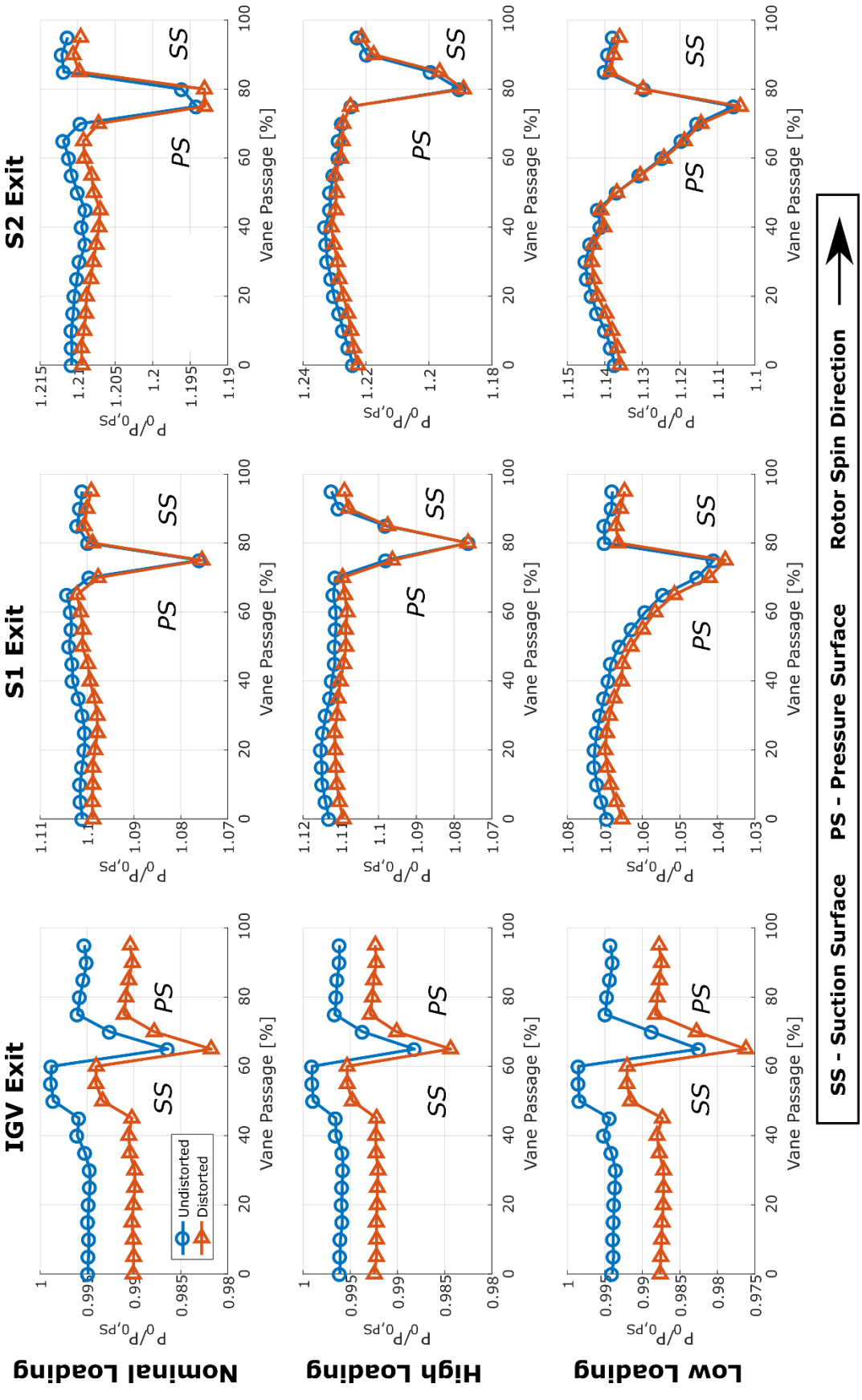

Figure 3-35. 50% Span Wake Comparison between Distorted and Undistorted Passages

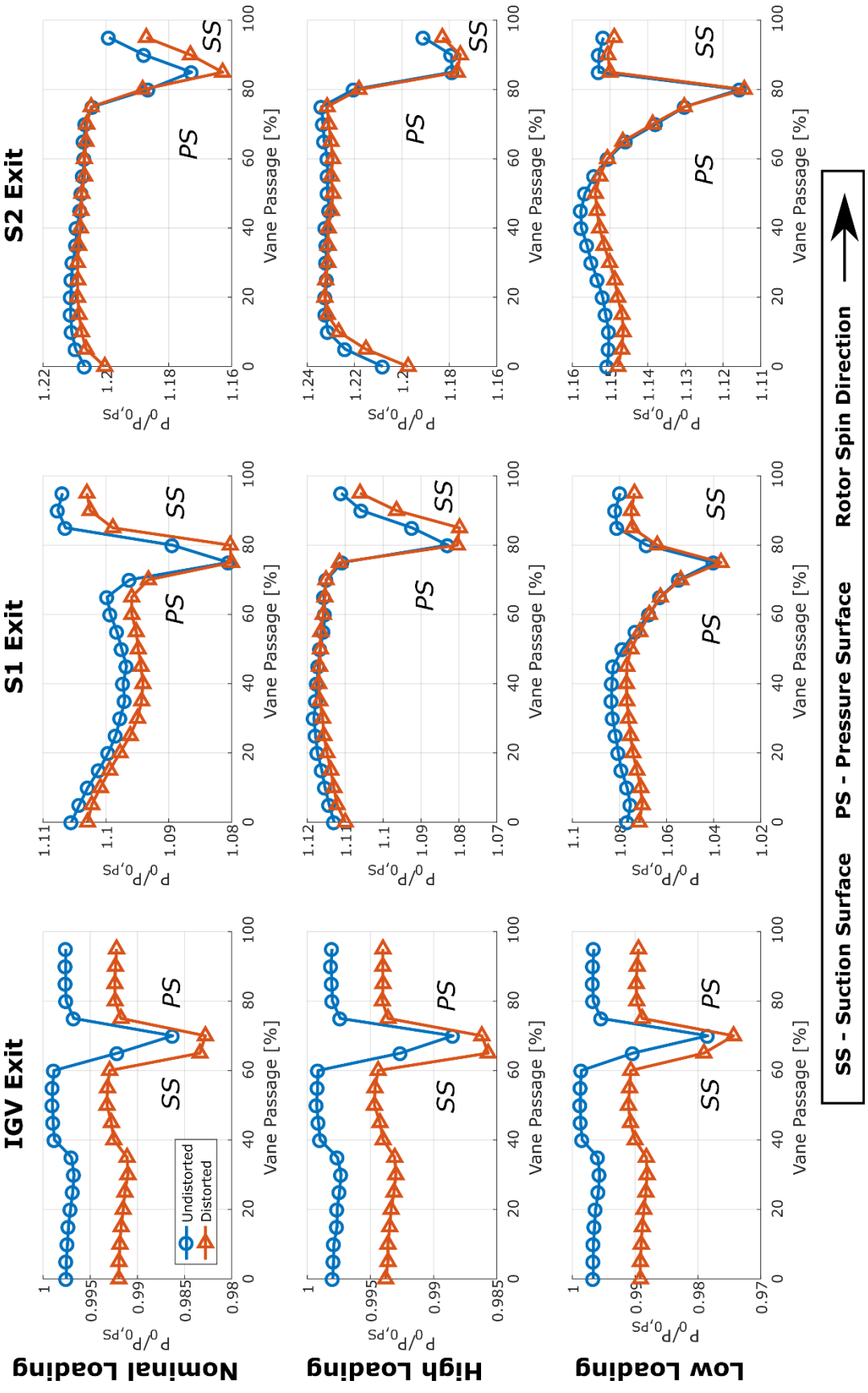

Figure 3-36. 20% Span Wake Comparison between Distorted and Undistorted Passages

At 20% span, widening of the wakes is most pronounced for the nominal and high loading conditions. The start of the wake on the pressure surface (PS) remains largely unchanged by the distortion while the wake thickens towards the suction surface (SS). This is indicative of a change in incidence angle at the 20% span leading to increased incidence losses, which result in a thicker wake resulting from a change in exit flow angle deviation and flow separation of the suction surface. The same phenomenon is not, however, observed at any span location for the low loading conditions location where the negative incidence causes a pressure surface separation wake. The effect of increased incidence angle due to the total pressure distortion at low loading causes a decrease in wake depth and thickness downstream of S1 and S2 since the incidence angle is brought closer to the design incidence. A larger magnitude distortion would likely cause a more significant change in the wakes which could be measured over a greater span of the vanes. However, the results presented here support the flow physics of how a total pressure distortion affects incidence flow angles.

Total pressure contour plots of the distorted and undistorted passages are shown in Figure 3-37, Figure 3-38, and Figure 3-39 for the nominal, high, and low loading conditions, respectively, to better visualize the radial and circumferential variations within each passage. The wake regions are shown in red which represents a pressure deficit compared to the rest of the passage. Black dots on the axes represent the locations of probes and rake locations used to generate the contour plot. Interpolation is used to generate a continuous contour to better study variation in flow features. The lighter shade of blue and darker red seen in the distorted vanes indicates that there is a global shift in the total pressure which confirms the observation made in Figure 3-35. While there are no drastic changes in passage flow features, the variation in total pressure fields at different loadings highlights the importance of considering the effects of different secondary flows when studying the propagation of inlet distortion in a multi-stage environment.

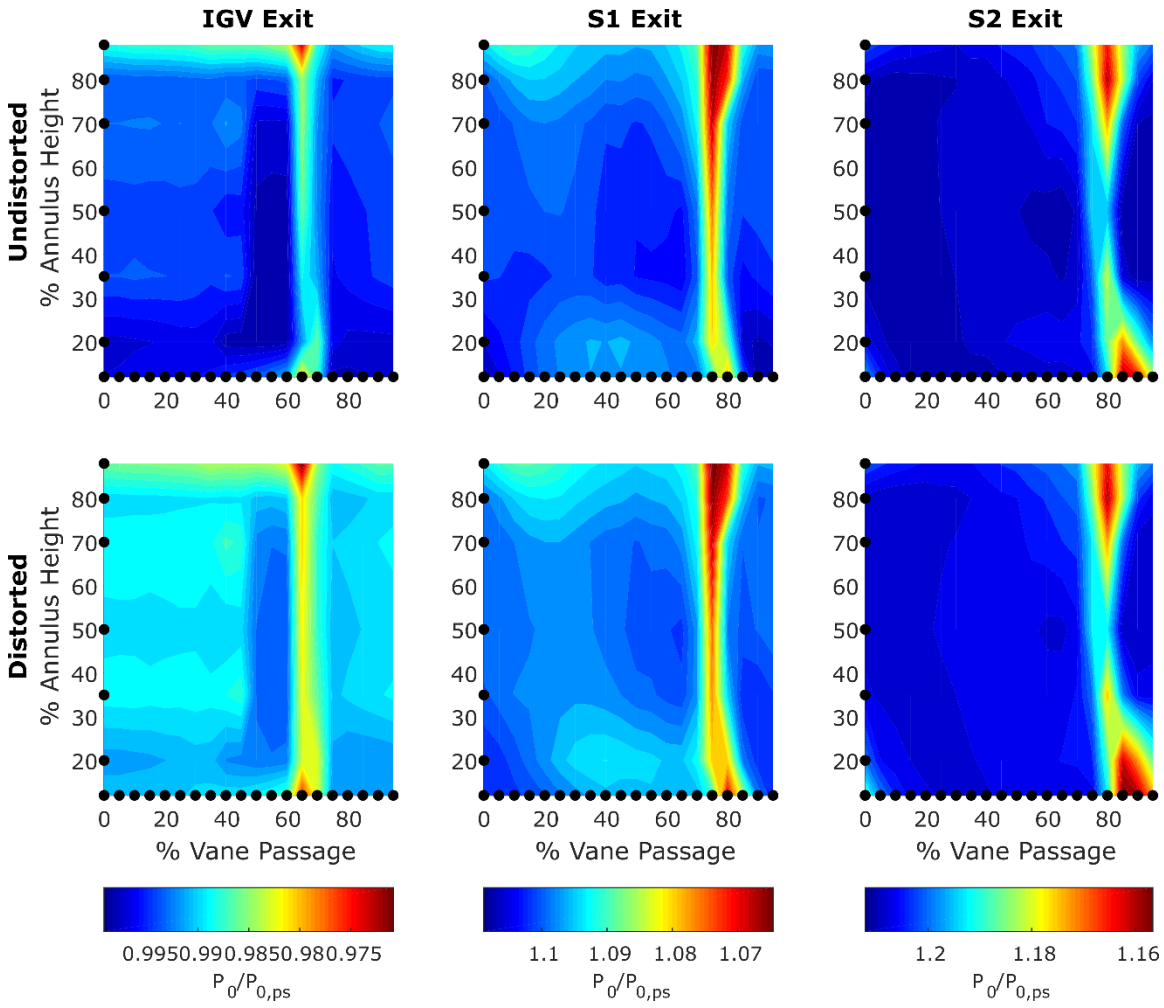

Figure 3-37. Comparison of Distorted and Undistorted Wake Passage Contour Plots – Nominal Loading

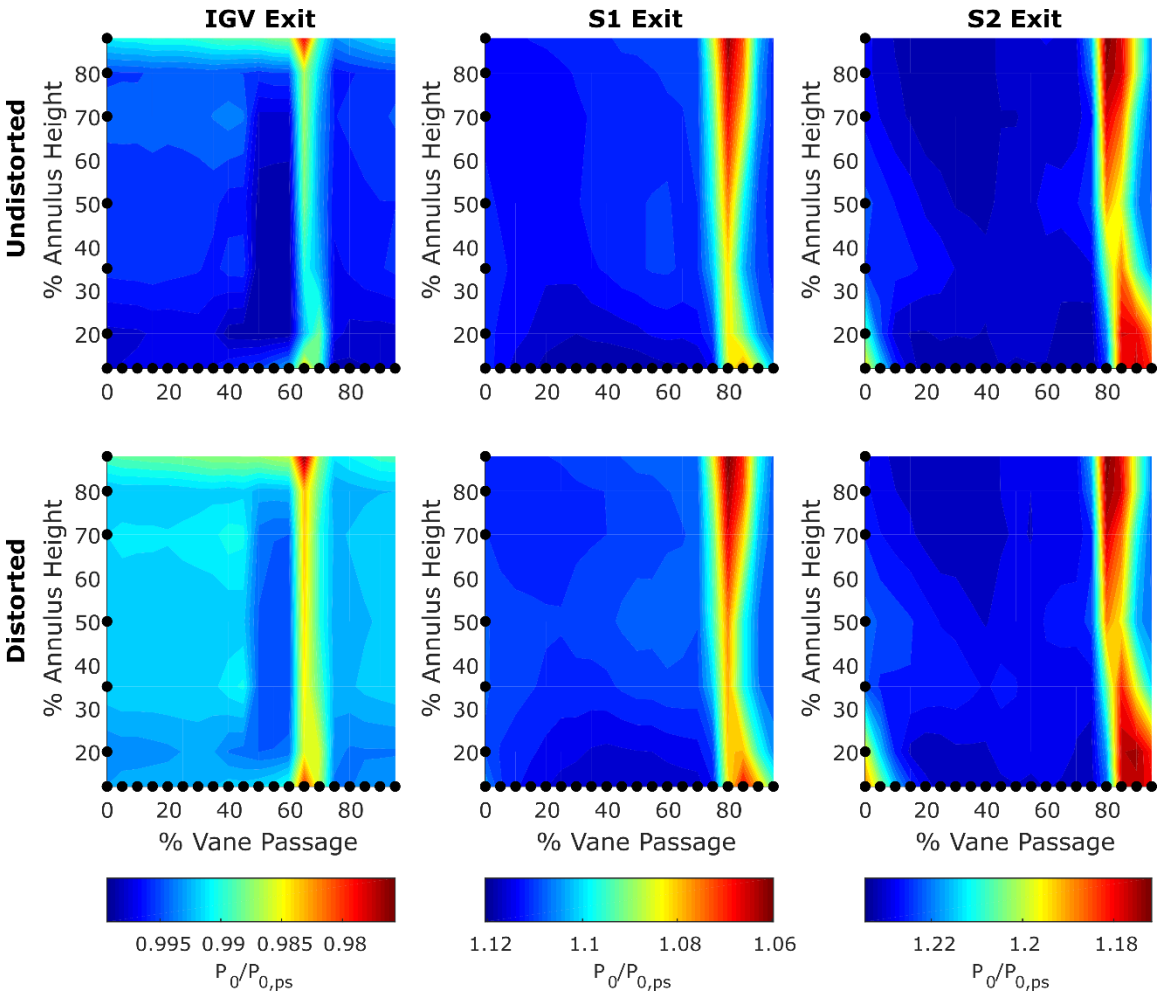

Figure 3-38. Comparison of Distorted and Undistorted Wake Passage Contour Plots – High Loading

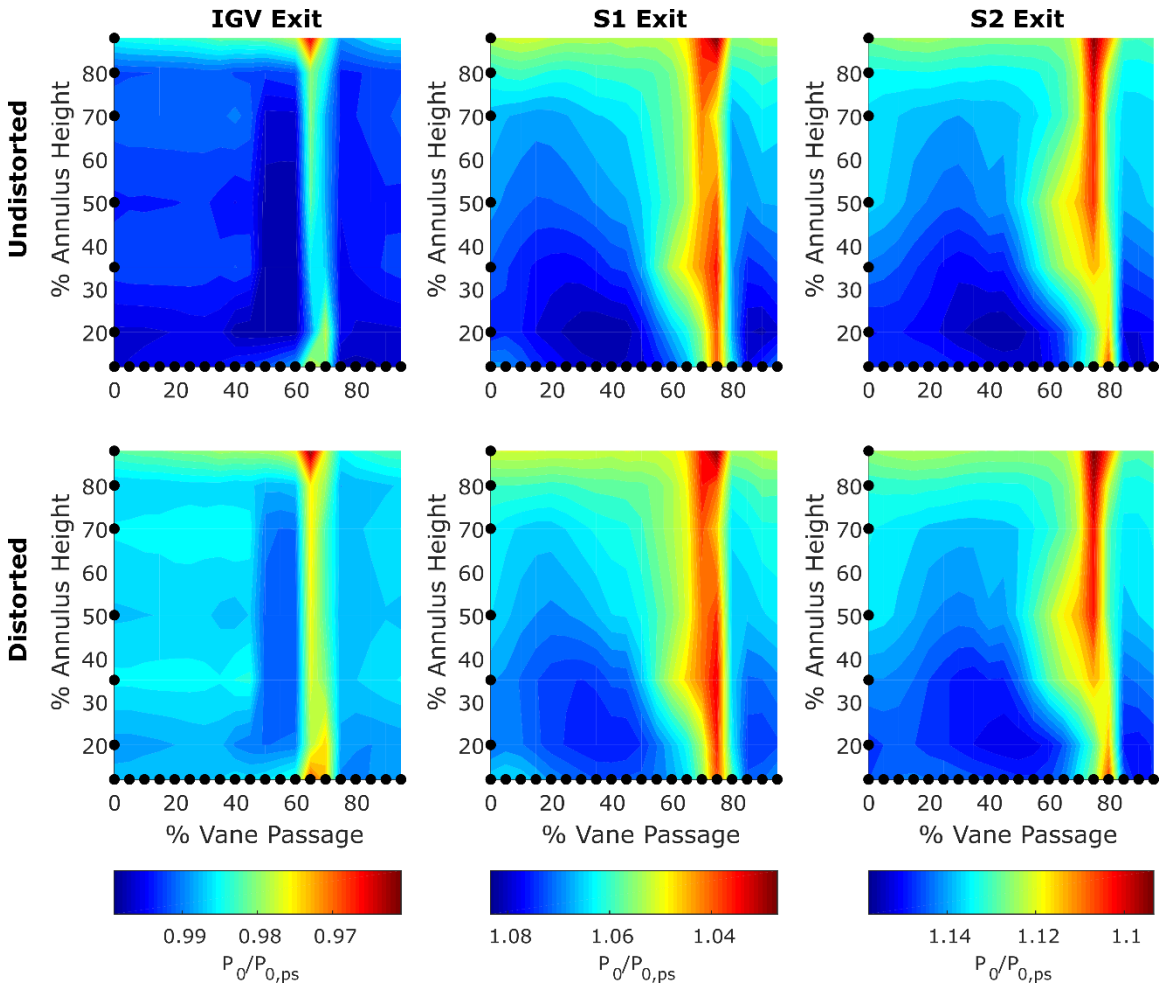

Figure 3-39. Comparison of Distorted and Undistorted Wake Passage Contour Plots – Low Loading

CHAPTER 4. STRAIN GAGE TELEMETRY SYSTEM PROPOSALS

4.1 Overview

Previous GUIde V studies used a Non-Intrusive Stress Measurement System (NSMS) provided by Agilis Measurement Systems to characterize the forced response condition of the embedded rotor stage on the PAX100 research compressor (Aye-Addo, 2016). The vibratory modes of interest were the 1st Torsion (1T), 1st Chord-Wise Bending (1CWB), and 2nd Chord-Wise Bending (2CWB). Similar to the current inlet distortion investigation, the experimental dataset acquired is intended to be used for validation of novel computational aeromechanical models. At the request of the GUIde V steering committee, an assessment of the feasibility of supplementing and validating NSMS data using traditional strain gage measurements was conducted.

The Campbell diagram for rotor 2, shown in Figure 4-1, is useful for defining the requirements for the strain gage telemetry system. The safe operating speed limit of the telemetry system should be at least 5000 RPM to safely accommodate data acquisition at all of the modes of interest. Furthermore, the Campbell diagram defines the requirements of the data acquisition hardware and strain gage transducers. The largest frequency of interest is just short of 6000Hz for the 2CWB. Therefore, using the Nyquist Sampling Theorem, the selected data acquisition hardware and transducers must permit a sampling frequency of at least 12,000Hz, although, modern digitizers can achieve much higher sampling frequencies.

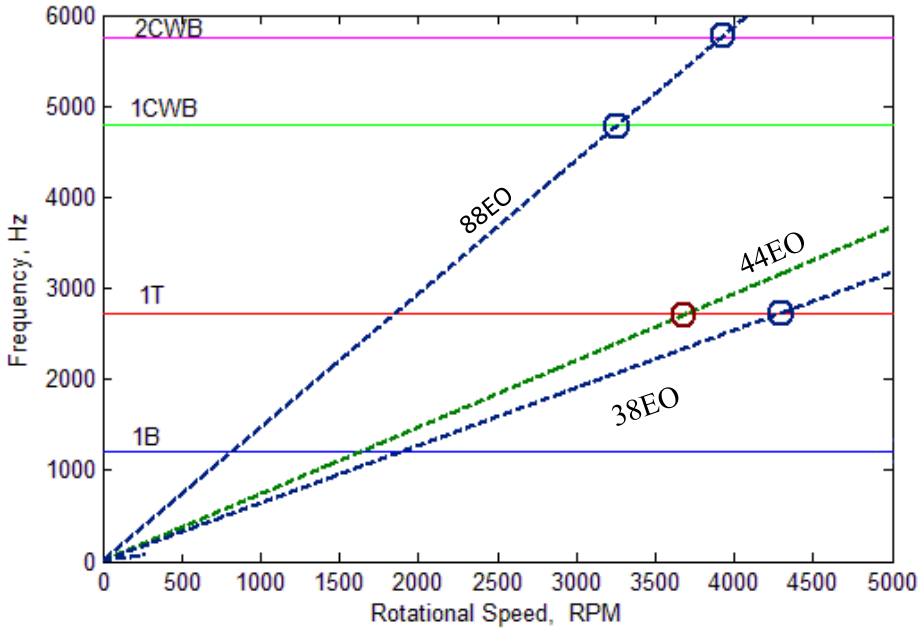

Figure 4-1. Campbell Diagram for Rotor 2

This chapter discusses proposals for outfitting the Purdue 3-Stage Axial Compressor Research (P3S) facility with a strain gage telemetry system. Strain gage telemetry systems include the strain gage transducers, wiring, signal telemetry, and data acquisition hardware. Signal telemetry is defined as the method of signal transmission, either analog or digital, between the transducers located on the rotating components and the data acquisition hardware in the stationary reference frame. Telemetry systems typically fall under two categories: slip rings or wireless telemetry. These categories can be further divided into digital and analog telemetry based on whether signal is digitized before or after the telemetry system.

For this study, two proposals are presented. The first proposal utilizes a traditional slip ring telemetry system and the second uses a digital wireless telemetry system. The two proposals are compared with regards to functionality, installation, cost, signal quality, maintenance life, and lead time. Methods of integrating telemetry hardware to the existing P3S facility are introduced along with a discussion on the necessary modifications to existing hardware.

4.2 Routing and Hardware Integration

The following section presents possible options for routing paths and the locations where telemetry hardware can be outfitted to the existing P3S compressor hardware. It is important that the selected routing and integration design minimizes the number and extent of modifications required to existing hardware. Telemetry hardware should also be accessible without major disassembly. The telemetry and strain gage wiring integration method presented is based on proposals and discussions with Florida Turbine Technologies (FTT) and Apex Turbine/Datatel Telemetry. As the writing of this work, only FTT had provided a complete proposal including strain gage installation, hardware modifications, new hardware, and integration services.

Telemetry hardware can be installed on the protruding end of the shaft in the cavity created by the front bearing support plate and the hollow elliptical nose cone as shown in Figure 4-2 and Figure 4-3. The shaft extends unobstructed into the cavity for 3.3 inches and measures 1.5 inches in diameter. This is the location where the slip ring interface assembly can be mounted to the shaft preferably via a keyless bushing to avoid the need for shaft modification.

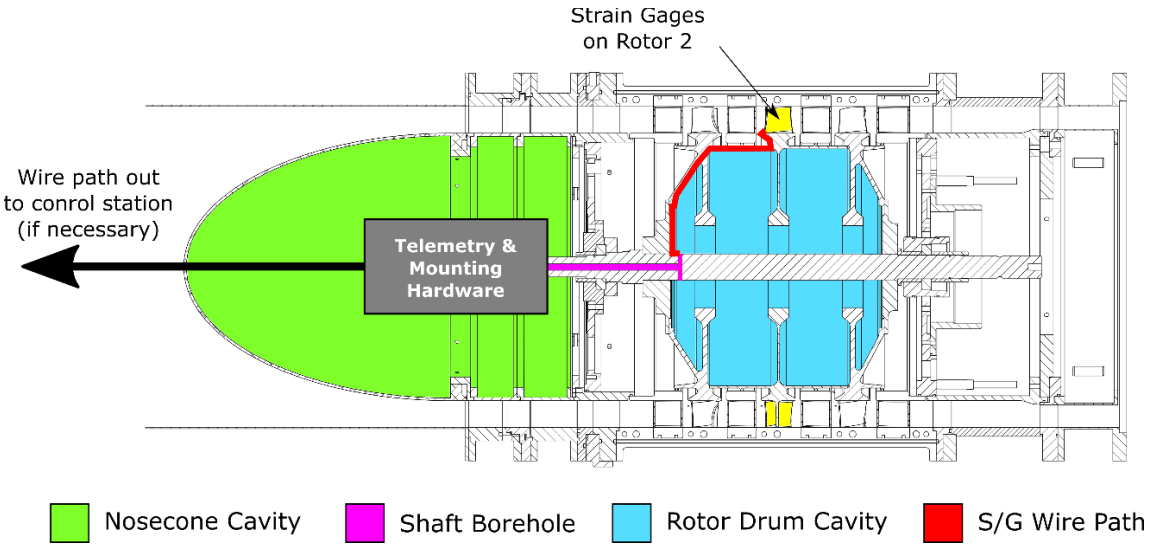

Figure 4-2: Available Telemetry Hardware and Wire Routing Cavities

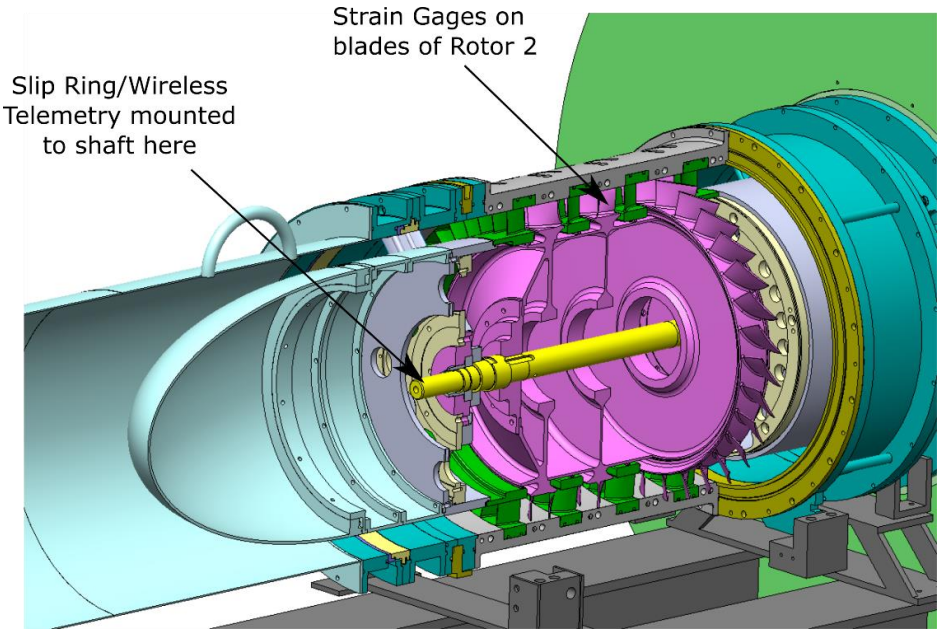

Figure 4-3. Cut-Away View of Nose Cone and Rotor Drum Cavities

The front portion of the shaft has an existing ½in bore which extends for 11in and joins a through hole as shown in Figure 4-4. This conveniently provides a path for wiring to pass between the rotor drum cavity and nose cone cavity as shown in Figure 4-2. Thus, minimal modification to the shaft would be required to route wiring from the strain gages on rotor 2 to the telemetry hardware in the nose cone cavity. FFT indicated that both rotor 1 and rotor 2 would require modification to permit proper routing and securing of strain gage wiring.

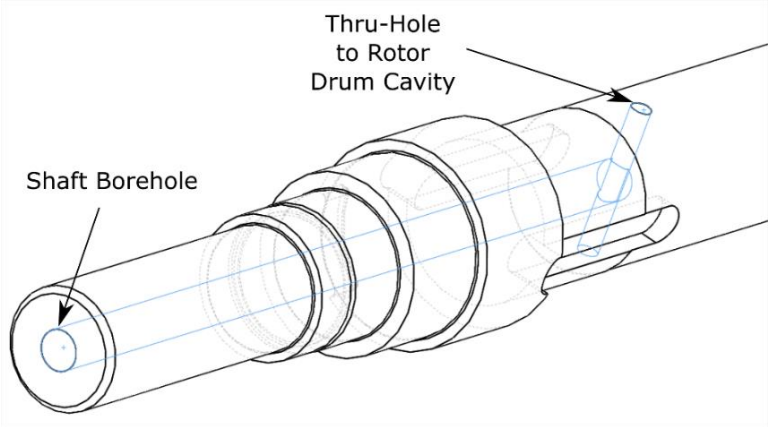

Figure 4-4. Existing Bore in Front End of Shaft Connecting Rotor Drum and Nose Cone Cavities

Regardless of whether the telemetry is a slip ring or wireless, a custom made shaft adapter is required for mounting. The slip ring rotor must affix to the end of the shaft while the housing must be restrained by attaching to some stationary component. Therefore, an additional adapter is required that would be affixed to the forward bulkhead following some minor modification.

Power and signal transmission to the telemetry hardware located inside the nose cone cavity can be route upstream through a pipe extending from the apex of the nose cone Figure 4-2. This pipe then exits the inlet duct approximately 10ft upstream of the nose cone. The modified nose cone and pipe are existing hardware that were utilized for another research project and would be available to be repurposed for the strain gage study. A photograph of the alternate nosecone is shown in Figure 4-5. Figure 4-6 shows the nose cone and pipe installed on the P3S compressor.

Figure 4-5. Pictures of Modified Elliptical Nose Cone

Figure 4-6. Photograph of Pipe Connecting to Nose Cone Cavity

4.3 Telemetry Selection

There are two methods of signal transmission that have been proposed by FTT and Apex Turbine. These include wireless telemetry and slip ring telemetry systems with channel counts varying from 10 up to 60 channels. An overview of the functionality and required hardware set-up is discussed in the following subsections.

4.3.1 Slip Ring

Slip rings have traditionally been the most popular option for telemetry systems for turbomachinery applications. Slip rings are electromechanical devices that continuously transmit electrical signals between stationary and rotating reference frames. The primary components in a slip ring are a brush and a ring both made of electrically conductive materials. The brush remains in continuous contact with the rotating ring which permits continuous conduction of current between the two reference frames. Slip rings counts typically indicate the number of ring and brush pairs contained within the device. The cost of slip rings is typically a function of the number of leads, however, the cost per count is lower for higher count devices.

Figure 4-7 shows a block diagram of the proposed slip ring telemetry system. The number of counts required is dependent on the type of transducer and number of transducers on the rotating side. For this study, strain gages are used to measure dynamic strain in order to capture the vibrational response of a particular rotor blade. For turbomachinery applications, the number of connections to each transducer is minimized to reduce the number leads required on the slip ring. It is recommended that the balanced constant current excitation method employed by Precision Filter's 28144 Quad-Channel Wideband Transducer Conditioner be used because it requires only two wires per sensor for dynamic strain measurements. The filtered signal is then digitized by a National Instruments multifunction digital acquisition (DAQ) card before being recorded onto a computer for post-processing.

A further consideration for slip ring telemetry is cooling and lubrication. At high rotational speeds, the friction between the brushes and rings generates a large amount of heat. An external cooling cart is required to circulate coolant to and from the slip ring to maintain safe operating temperatures. Proper cooling is essential to maximizing the useful life of the slip ring. In the current design, the cooling lines would use the same routing path to reach the slip ring as does the wiring. Consideration must be given to the size of the cooling lines such that there remains sufficient room for the signal wiring. In the event that the existing routing pipe is too small, some modification will be required to the nose cone to permit the attachment of a larger pipe.

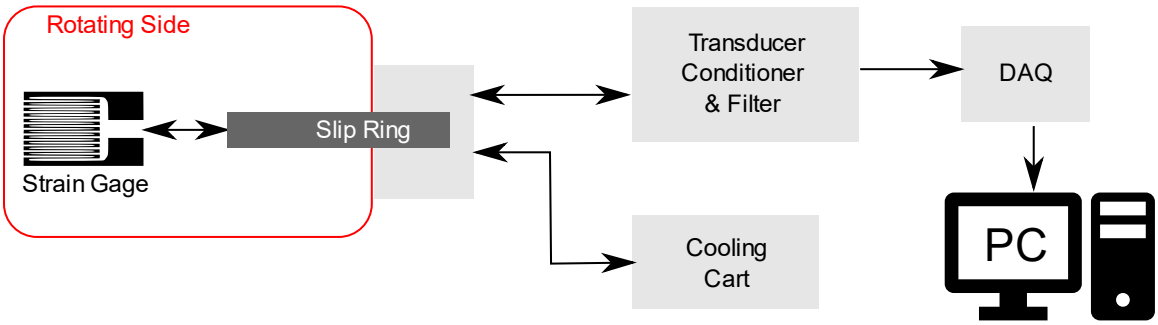

Figure 4-7. Slip Ring Telemetry Block Diagram

4.3.2 Wireless Telemetry

The second proposal considered for this project is a wireless telemetry system. The discussion is based on proposals put forth by Datatel Telemetry in partnership with Apex Turbine. As the name implies, wireless telemetry transmits the transducer signal without the use of any mechanical components or wiring. Wireless telemetry is especially popular for gas turbine applications since it requires no direct connection to any stationary components and thus, very little modification is required for integration into an existing machine.

Figure 4-8 shows a block diagram of the wireless telemetry system proposed by Apex Turbine and Datatel Telemetry. Sensor excitation and signal digitization both occur on the rotating side in the wireless telemetry unit. Power to the telemetry unit can be supplied either by a battery or using inductive charging. For longer operation times, such as those required for compressor studies, the inductive charging option is preferable. A telemetry receiver card located inside the test cell receives the signal wirelessly from the transmitter. A digital interface card is required for the computer to read the strain gage signals. The telemetry unit also provides health monitoring information of the transmitter and power supply. A remote-control unit sends commands to the telemetry unit via the telemetry card to operate functions such as programming the current excitation to the strain gages.

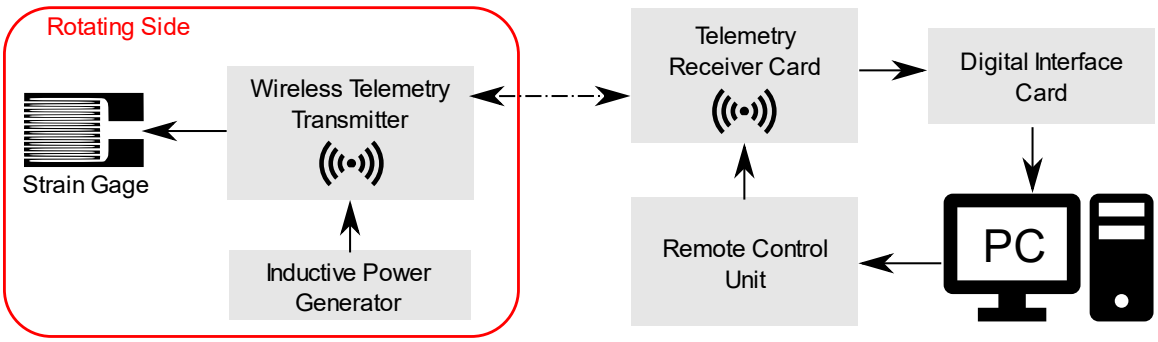

Figure 4-8. Wireless Telemetry System Block Diagram

4.3.3 Comparison of Telemetry Systems

Table 4-1 summarizes the differences between the two telemetry systems considered in this work.

Table 4-1. Comparison of Slip Ring and Wireless Telemetry Systems

	Slip Ring	Wireless Telemetry
Signal Quality	• Typically suffer from low signal-to-noise ratios (SNR) due to the nature of the brush-ring contact • Poor signal quality for lower magnitude vibrations • Expensive signal filtering equipment is required	• Signal is digitized on the rotating side having the potential for increased signal quality, especially at lower vibration amplitudes • Proper calibration is required to account for noise introduced by magnetism of rotor
Cooling & Lubrication	• Cooling & lubrication system is required to maintain safe operating temperatures of brushes and rings	• No cooling or lubrication system required
Maintenance	• Short-interval maintenance is required to service seals and abradable surfaces	• No short-interval maintenance is required
Operating Life	• On the order of a couple hundred hours for current speed application • Operating life is limited by the abradable precious metal contacts	• Very long life in low temperature environments
Intrusiveness	• Cooling system and wire routing requirements disturb upstream flow path in current design.	• Unit is self-contained, and no obstruction is required to route cables or coolant lines to nose cone cavity
Speed	• Lower speed rating • Long term operation at high speed reduces component life	• Very high-speed capabilities that far exceed current requirements
Post-processing	• Custom in-house post-processing codes must be created	• 'Black Box' operation – annual software licenses are required to read data using proprietary software
Cost	• Cheaper hardware cost • Higher maintenance costs • No proprietary software license cost	• Higher hardware cost • Lower maintenance costs • Annual proprietary software license costs
Lead Time	• Shorter lead time due to availability of commercial off-the-shelf products (COTS) • US-based suppliers	• Longer lead time necessitated by customization of all telemetry units • Overseas suppliers
Integration	• More modification is required to stationary and rotating hardware	• No modification required, only new adapter hardware

Neither option is clearly a better choice for the required application. There are advantages and disadvantages for each category discussed above. In summary, from a cost perspective, the slip ring option is more appealing especially if the system is not meant to be utilized for long term applications. From a performance and signal quality perspective, the wireless telemetry system has the potential to provide much higher quality data especially for lower amplitude vibration, such as those observed in higher order mode shapes. However, as previously mentioned, the more proprietary nature of the wireless telemetry system means that recurring license subscription costs be paid for the duration of the project which increases the financial commitment. However, this subscription also means that there is the possibility for support and troubleshooting for data-collection and post-processing.

4.4 Strain Gage Installation

In addition to the strain gage signal telemetry system, consideration was also given to the strain gage placement analysis and installation. The following activities surrounding strain gage installation are based on the proposal received from FTT. The first task is to identify the ideal placement of the strain gages on the rotor blades such that the vibrational modes of interest can be captured adequately with the least number of strain gages. The analysis is performed using Apex Turbine's GageMap software which utilizes the blade's modal analysis results obtained from a finite element model to determine the optimum strain gage placement location and orientation.

The next step is to use ping testing and holography in order to find the exact mode shapes for each airfoil. This step is required to account for the variations in mode shape caused by mistuning. Calibration strain gages will be used to verify the GageMap analysis and select the final placement location. Finally, the calibration strain gages are removed, and the final strain gages are installed. The wiring must be properly secured and routed such that it does not come loose during testing. It is recommended that the rotor be balanced prior to strain gage installation and after all modifications for routing have been made so that there is no risk to damaging the strain gages.

Based on past experience, FTT has recommended that a redundancy factor of three be used for each strain gage measurement. Each strain gage placement location should be repeated on at least three different blades. This is because of the high likelihood of strain gage failure when subjected to the harsh environments experienced in high speed turbomachinery. Repairing and replacing a faulty gage would be extremely costly and time intensive, and therefore, it is cheaper to increase redundancy.

CHAPTER 5. CONCLUSIONS AND RECOMMENDATIONS

The objective of this research was twofold. The first was to establish and validate a flexible testbed for studying inlet total pressure distortion patterns with a high degree of circumferential resolution. The second was to provide an experimental dataset consisting of flow measurements capturing the propagation and attenuation of the distortion in a multistage environment with a high degree of detail. All studies were performed at 100% corrected speed for three compressor loading conditions which include nominal loading (NL), low loading (LL), and high loading (HL). The goal of this dataset was to support the development and validation of novel computational techniques for the prediction of inlet total pressure distortion propagation through a multi-stage compressor environment. This project is part of an ongoing GUIde V research objective combining experimental and computational efforts to improve compressor design tools and methods.

This study was conducted at Purdue University's High-Speed Compressor Lab on the Purdue 3-Stage Axial Compressor Research facility (P3S) in the PAX100 configuration. This research compressor models the final three stages of a Rolls Royce turbofan engine's high-pressure compressor (HPC). The PAX100 consists of an IGV followed by three compressor stages. The IGV and three stator rows are individually indexable by up to two stator passages relative to stationary casing-mounted instrumentation. Since the instrumentation is fixed, circumferential measurements at the AIP and between blade rows were accomplished with a combination of coordinated vane and distortion screen traverses.

A new distortion screen traverse was designed, built, and integrated into the existing P3S facility for this study. A total pressure distortion was generated using a series of wire gauze screens located in the tubular inlet duct approximately 5.5 pipe diameters upstream of the compressor AIP. The screens were secured to the upstream side of an Aluminum honeycomb carrier. The carrier was affixed to a rotatable section that could be precisely rotated using an externally mounted stepper motor. Data acquisition and traverse control were effected by an automated program executed in LabVIEW to decrease operator workload, reduce traverse time, and improve repeatability.

Prior to introducing distortion screens into the flow, the effect of the honeycomb carrier on the inlet flow at the AIP was characterized. The carrier was rotated past stationary instrumentation at the AIP to capture a full 360° total pressure field. All circumferential variation in total pressure fell within the uncertainty bounds of the total pressure probe. The carrier was sufficiently uniform and did not introduce any circumferential non-uniformities into the inlet flow. The average total pressure loss introduced by the carrier compared to a clean inlet configuration was only 0.04%. Furthermore, the radial profile was shown to a have a slightly more curved appearance due a greater pressure loss at the hub and shroud.

Only one distortion screen was required for this investigation since the focus was on propagation and attenuation measurements rather than on the distortion parameter variations. The requirements of the screen were that it generate a one-per-rev total pressure distortion of sufficient circumferential extent and strength that it can be measured at the AIP and throughout the compressor. An iterative approach was employed for the screen selection process. Three screens were tested with 120° circumferential extent and 100% radial extent. The screens were composed of a series of varying porosity screens that were overlaid to reduce the effective porosity. The total pressure flow field was characterized for each of the screens which varied only in porosity. The screen with the greatest pressure drop was selected as the final screen candidate.

High-resolution total pressure fields at the AIP were acquired using the selected screen candidate to characterize the inlet flow boundary condition for the three compressor loading conditions. The max distortion percentage was observed to be 0.42%, 0.56% and 0.32% with circumferential extents of 144°, 144°, and 145° for NL, LL and HL, respectively. Evidence of non-uniform radial mixing was discerned from the change in radial profile at the AIP compared to the carrier alone. The results were indicative of greater mixing in the center of the duct which is in keeping with other studies found in literature. Despite the relatively long distance between the AIP and the distortion screen, the circumferential distortion persists, albeit with a shallower pressure gradient between the low and high-pressure regions due to mixing effects.

In an effort to further characterize the inlet flow conditions for defining boundary conditions necessary for CFD investigations, hot wire anemometry was used to measure turbulence intensity variation circumferentially and radially at select positions. Calibration of the constant temperature anemometer was performed at Purdue's Compressible Hotwire Calibration Facility and temperature correction was applied to all measurements. The average turbulence intensity was measured to be 2.38%, 2.09%, and 2.38% at NL, LL, and HL, respectively. These intensity magnitudes are within the typical range expected for turbomachinery inlet flow conditions.

The turbulence intensity variation reveals a circumferential non-uniform pattern with a nearly 1% difference between the intensity inside and outside the distorted flow region. Furthermore, the peak intensity does not coincide with the location of peak distortion, rather, two peaks exist to either side of the peak distortion position. These peaks are indicative of the mixing occurring on the boundary between the low and high-distortion regions. An increase in distortion intensity increased the turbulence intensity since the lowest turbulence intensity occurred at LL. Radial plunges were performed at the locations of maximum and minimum distortion and at the screen boundary locations. Evidence of non-uniform radial mixing occurred.

Distortion propagation and attenuation was evaluated with total pressure measurements between each blade row from the AIP to the compressor exit. A single rake measurement was used to estimate the bulk flow through each stator passage. The distortion was rotated by an increment equal to one stator vane passage in order to acquire virtual measurements in all stator vane passages. The total pressure distortion persisted through all of the stages all the way to the compressor exit, albeit greatly attenuated. The rotors had the greatest effect on reducing the distortion intensity while the intensity remained relatively constant through the stators. The attenuation-per-stage was not constant for all three compressor loading conditions. Regardless of the distortion intensity at the AIP, the resulting intensity at the compressor exit was approximately the same. The location of maximum distortion did not appear to follow any distinguishable pattern; however, it did remain within two stator passages of the initial position throughout the length of the compressor.

The final investigation sought to characterize the inter-stage total pressure flow field corresponding to the 44 vane IGV, S1, and S2 using a series of coordinated distortion and vane traverses. The resulting full annulus total pressure contour plots have a circumferential resolution of 880 rake positions, or one every 0.41°, for a total 6160 total pressure measurements used to characterize each annular flow field. All wakes, potentials, and inter-passage variations were captured using this method. This represents one of the most detailed inter-stage total pressure flow field characterizations for an inlet distortion study found in open literature to date. The primary purpose of these detailed measurements is to provide a database for the evaluation and adjustment of novel CFD models meant to predict inlet distortion flow propagation in multi-stage compressors.

Using the more detailed inter-stage flow field characterization, the single rake approximation of each vane passage was evaluated for the purposes of capturing the attenuation and propagation. The face average pressure was shown to be higher when approximated by a single point due to the increased significance of the wakes in downstream stages. The attenuation and average circumferential pressure variation, however, were in reasonably good agreement suggesting that the single point vane passage approximation serves as useful experimental method to significantly reducing data acquisition time.

Despite the high resolution of the total pressure field characterization, the distortion magnitude used in this study was too small to cause any significant changes in wake size or location between distorted and undistorted flow regions over a large radial span distance. A change in the wake shape was observed only at one span-wise location near the hub. The observations made at this vane span were, however, in keeping with expected flow phenomenon caused by a total pressure distortion. It is recommended that future studies try to measure the difference in flow angles using either hot wire measurements or a 2-dimensional directional pressure probe to attempt to detect differences between distorted and undistorted wakes. However, the uncertainty in these measurements may still be too large to capture the differences caused by such a small distortion magnitude. If the current distance between the AIP and the distortion screen is maintained, then additional iteration

of screen shape and porosity parameters is recommended to try to increase the distortion magnitude. An initial strategy may be to increase the extent from 120° to 180° circumferential extent such that mixing between the low and high-pressure region is further delayed for the given pipe length. Increasing the distortion magnitude, even marginally, would result in a larger circumferential variation in blade incidence. Once this variation becomes sufficiently large, it is expected that more significant changes in secondary flow features could be observed between distorted and undistorted vane passages.

An alternate strategy to increase the distortion magnitude is to decrease the distance between the AIP and the distortion screens such that upstream mixing and attenuation is reduced. The simplest option is to swap the location of the 10ft inlet duct and traverse assembly. Due to the differing geometry of the mating flanges and bolt patterns, the existing duct assemblies will require some modification. This configuration would reduce the distance between the distortion screen and AIP to 1.5 pipe diameters as illustrated in Figure 5-1.

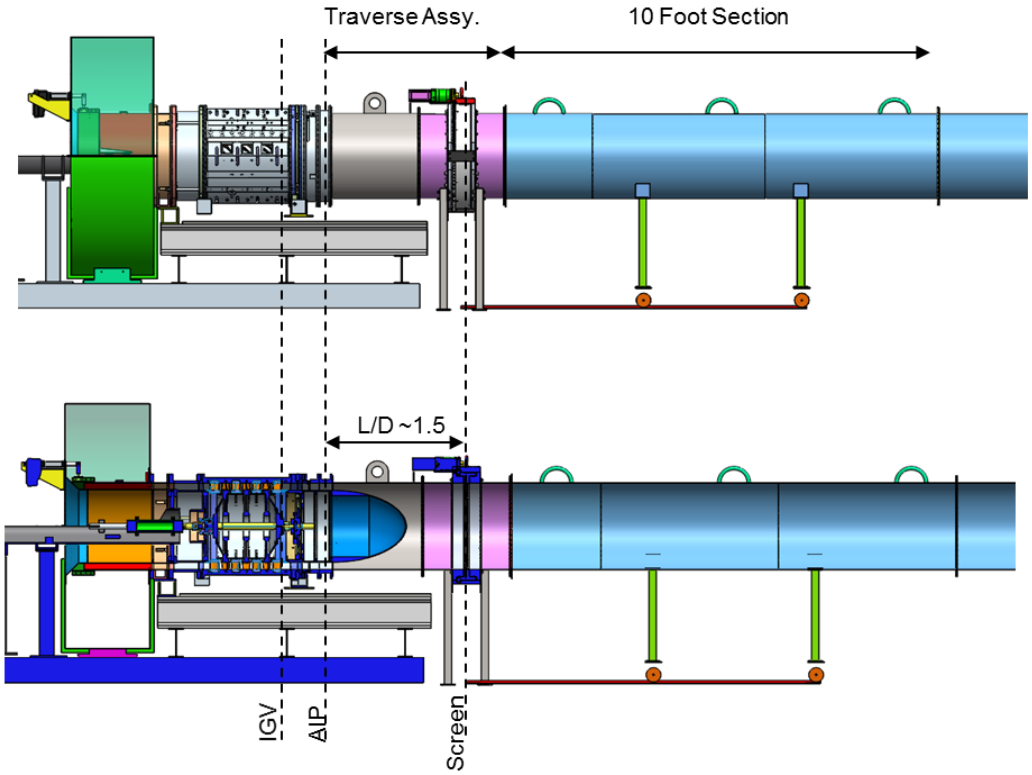

Figure 5-1. Alternate Integration of Inlet Distortion Traverse Assembly to Purdue 3-Stage Compressor Research Facility (Option #1)

A further step would be to move the distortion screen to the annulus where the pressure drop across the screens would be increased due to an increased flow velocity. This option, shown in Figure 5-2, would require that a new cylindrical extender section be manufactured to move the nose cone upstream so that there is sufficient space to introduce the distortion screen in the constant area annulus. The honeycomb carrier and mating flanges would also need to be modified along with the design of a new support structure. Due to the large number of modifications and new components required, this option would be the more expensive alternative. This option, however, would both decrease the distance between the AIP and distortion screen while also increasing the pressure drop across the screen due to an increase in flow velocity by a factor 3.3. The result is a pressure drop approximately 10 times greater than the one generated in the current configuration for a given screen porosity.

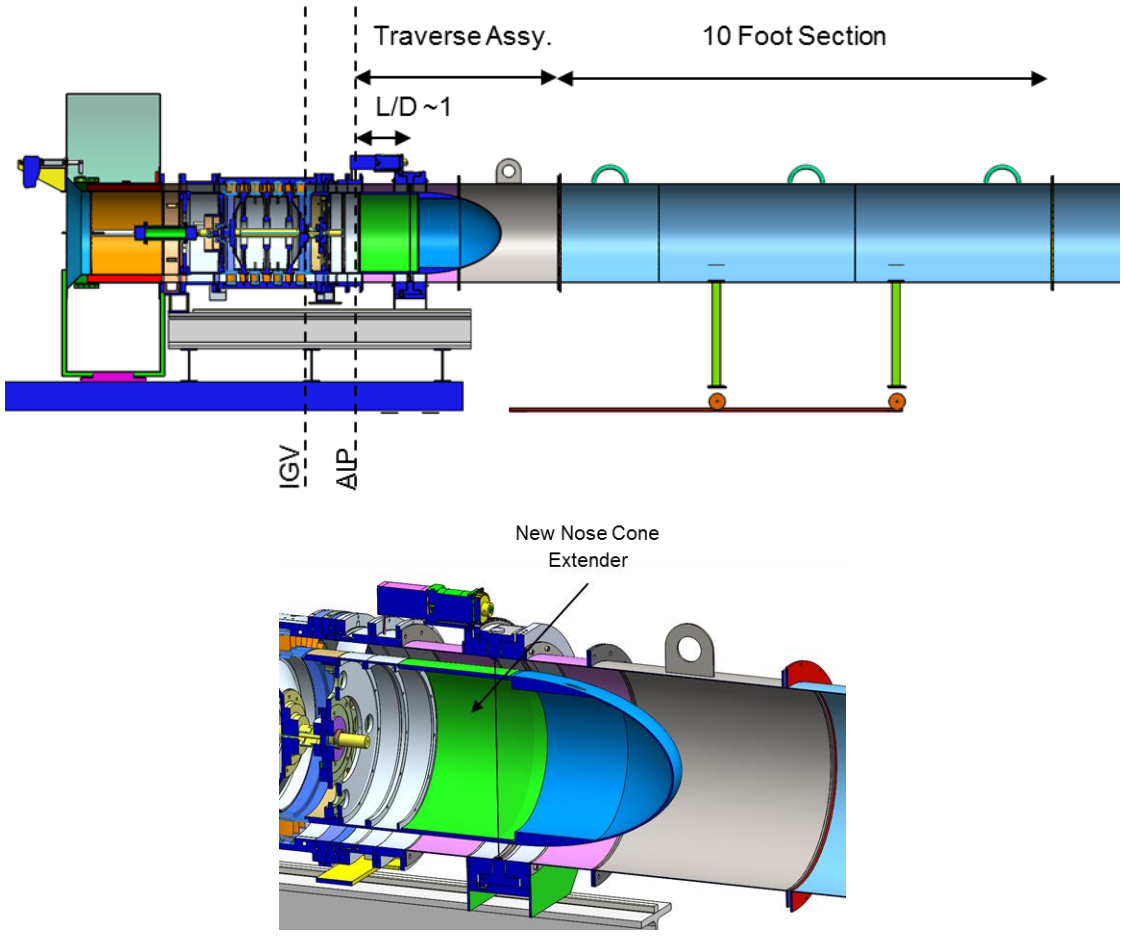

Figure 5-2. Alternate Integration of Inlet Distortion Traverse Assembly to Purdue 3-Stage Compressor Research Facility (Option #2)

In conclusion, the inlet distortion study presented in this work has demonstrated the successful integration of an automated inlet distortion traverse system to study the propagation and attenuation of a total pressure distortion in a 3-stage axial compressor. Data acquisition strategies have been demonstrated to yield inter-stage measurements in unprecedented detail which can be very valuable for supporting the development of novel CFD tools. The distortion traverse testbed can be readily extended to further studies relating to inlet distortion propagation or towards the study distortion effects on compressor performance and stability.

Proposals to outfit the P3S compressor research facility with strain gage telemetry functionality to supplement existing NSMS data have been documented and discussed. The presented proposals are based on consultations and formal proposals from two suppliers: Florida Turbine Technologies (FTT) and Apex Turbine/Datatel Telemetry. The options for signal telemetry discussed in this work are electromechanical slip rings or wireless digital telemetry. A qualitative comparison of the two systems has been presented to aid in the selection process for future investigators.

An evaluation of integration options has been performed to understand the scope of modifications and additional hardware required. Preliminary wire routing paths and hardware integration locations have been devised and presented to suppliers. Cost estimates, hardware requirements, and lead times have been submitted by both suppliers. FTT has submitted a proposal for both a slip ring and wireless telemetry and Apex Turbine/Datatel have submitted proposals for wireless telemetry system. The proposals are documented here to aid future investigators continuing work on this project.

APPENDIX A. ADDITIONAL RESULTS – DISTORTION PROPAGATION

A1. Low Loading Condition

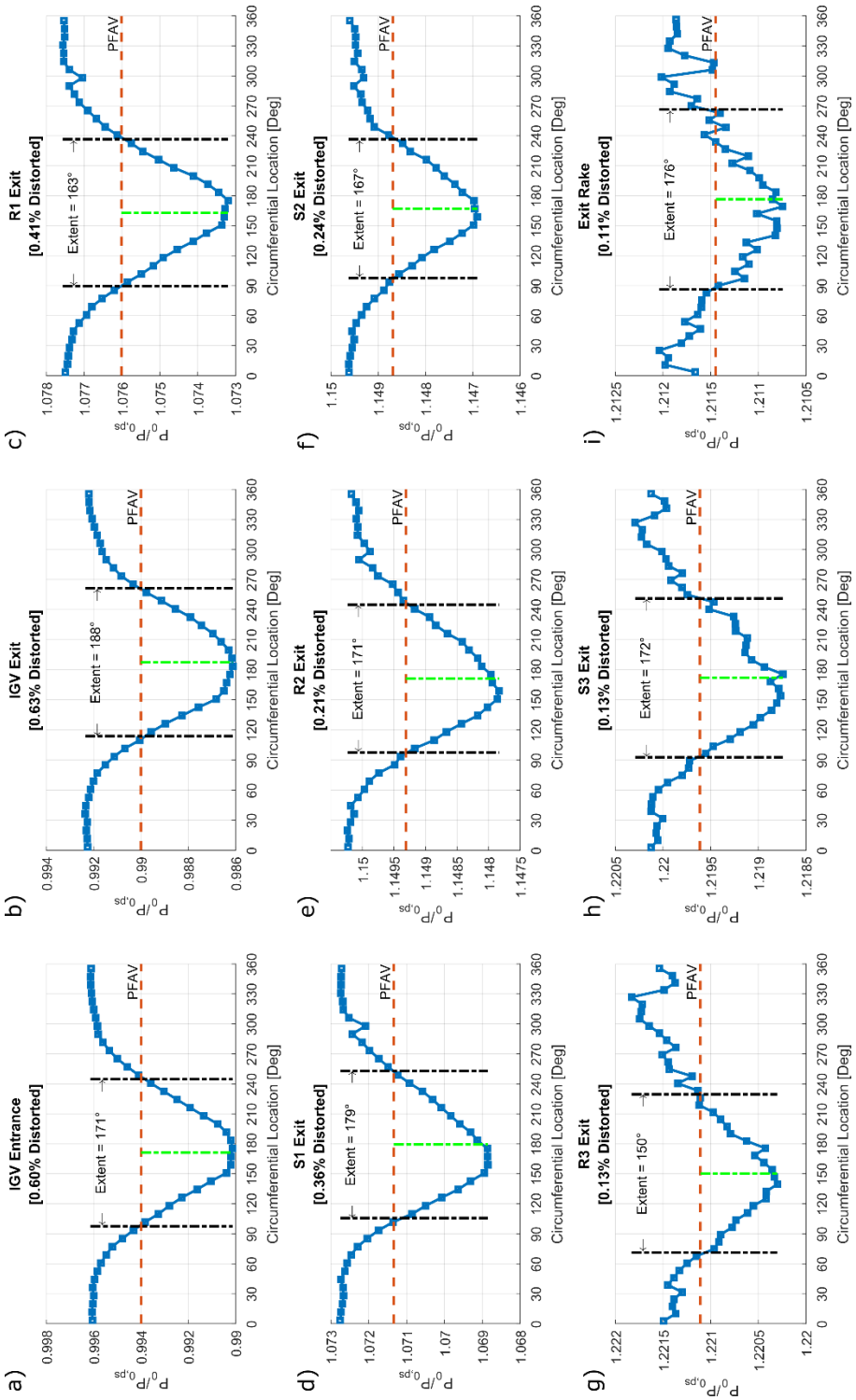

Figure A-1. Circumferential Variation in Inter-Stage PRAA at a) IGV Entrance, b) IGV c) R1 d) S1 e) R2 f) S2 g) R3 h) S3 Exits and i) Exit Rake – Low Loading

A2. High Loading Condition

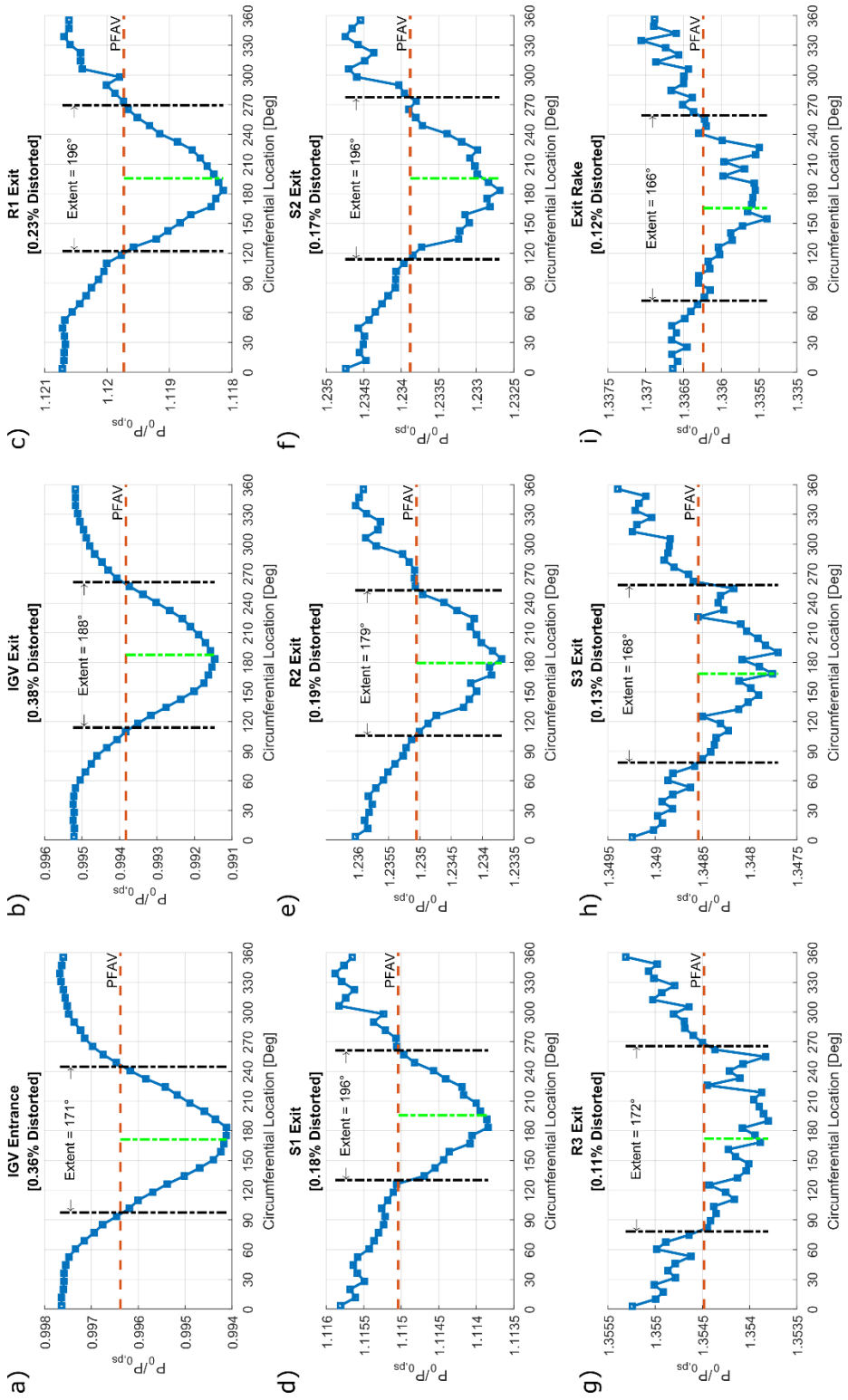

Figure A-2. Circumferential Variation in Inter-Stage PRAA at a) IGV Entrance, b) IGV c) R1 d) S1 e) R2 f) S2 g) R3 h) S3 Exits and i) Exit Rake – High Loading

REFERENCES

Ackerman, R. I., Jr, R. W. A., Keith, S. R., Leeke, L. E., & Jr, R. E. M. (2003, March 5). *EP1288440 A2*. Retrieved from http://www.google.com/patents/EP1288440A2

Ariga, I., Kasai, N., Masuda, S., Watanabe, Y., & Watanabe, I. (1983). The Effect of Inlet Distortion on the Performance Characteristics of a Centrifugal Compressor. *Journal of Engineering for Power*, *105*(2), 223. https://doi.org/10.1115/1.3227406

Aye-Addo, P. A. N. (2016). *An Experimental Study of the Effects of Vane Count and Non-Uniform Vane Spacing on Rotor Resonant Response*. Purdue University.

Ball, P. R. (2013, May). *An Experimental and Computational Investigation on the Effects of Stator Leakage Flow on Compressor Performance*. Purdue University.

Beale, D., Cramer, K., & King, P. (2002). Development of Improved Methods for Simulating Aircraft Inlet Distortion in Turbine Engine Ground Tests (Invited). American Institute of Aeronautics and Astronautics. https://doi.org/10.2514/6.2002-3045

Beauseroy, P., & Lengellé, R. (2007). Nonintrusive turbomachine blade vibration measurement system. *Mechanical Systems and Signal Processing*, *21*(4), 1717–1738. https://doi.org/10.1016/j.ymssp.2006.07.015

Beirow, B., Kühhorn, A., Figaschewsky, F., & Nipkau, J. (2015). Effect of mistuning and damping on the forced response of a compressor blisk rotor (Vol. 7B). American Society of Mechanical Engineers ASME. https://doi.org/10.1115/GT2015-42036

Berdanier, R. A. (2015). *An Experimental Characterization of Tip Leakage Flows and Corresponding Effects on Multistage Compressor Performance*. Purdue University.

Berdanier, R. A., Smith, N. R., Fabian, J. C., & Key, N. L. (2015). Humidity effects on experimental compressor performance—corrected conditions for real gases. *Journal of Turbomachinery*, *137*(3), 031011.

Braithwaite, W. M., Graber, E. J., & Mehalic, C. M. (1973). The Effect of Inlet Temperature and Pressure Distortion on Turbojet Performance. AIAA 73-1316.

Braithwaite, W. M., & Soeder, R. H. (1980). Combined Pressure and Temperature Distortion Effects on Internal Flow of a Turbofan Engine. *Journal of Aircraft*, *17*(7), 468–472. https://doi.org/10.2514/3.57927

Breuer, T., & Bissinger, N. C. (2010). Basic Principles – Gas Turbine Compatibility – Gas Turbine Aspects. In *Encyclopedia of Aerospace Engineering*. John Wiley & Sons, Ltd. https://doi.org/10.1002/9780470686652.eae573

Campbell, A. F. (1981). *An investigation of distortion indices for prediction of stalling behavior in aircraft gas turbine engines*. Virginia Polytechnic Institute and State University.

Chivers, N. J. D., & Topliss, P. S. (2008, November 4). *US7445433 B2*. Retrieved from http://www.google.com/patents/US7445433

Cousins, W. T. (2004). History, philosophy, physics, and future directions of aircraft propulsion system/inlet integration. *ASME Paper GT2004-54210*.

Cousins, W. T., Dalton, K. K., Andersen, T. T., & Bobula, G. A. (1994). Pressure and Temperature Distortion Testing of a Two-Stage Centrifugal Compressor. *Journal of Engineering for Gas Turbines and Power*, *116*(3), 567–573. https://doi.org/10.1115/1.2906857

Cousins, W. T., & Davis, M. W. (2011). Evaluating Complex Inlet Distortion with a Parallel Compressor Model: Part 2–applications to complex patterns. In *Proceedings of ASME Turbo Expo* (pp. 6–10).

Cousins, W. T., Georges, M. J., & Rezaei, H. (2003). Inlet distortion testing and analysis of a high-bypass ratio turbofan engine. *ISABE Paper*, (2003–1110).

Cumpsty, N. A., & Horlock, J. H. (2005). Averaging Nonuniform Flow for a Purpose. *Journal of Turbomachinery*, *128*(1), 120–129. https://doi.org/10.1115/1.2098807

Danforth, C. E. (1975). Distortion-induced vibration in fan and compressor blading. *Journal of Aircraft*, *12*(4), 216–225.

Davis, M., Hale, A., & Beale, D. (2002). An Argument for Enhancement of the Current Inlet Distortion Ground Test Practice for Aircraft Gas Turbine Engines. *Journal of Turbomachinery*, *124*(2), 235–241. https://doi.org/10.1115/1.1451087

Di Maio, D., & Ewins, D. J. (2012). Experimental measurements of out-of-plane vibrations of a simple blisk design using Blade Tip Timing and Scanning LDV measurement methods. *Mechanical Systems and Signal Processing*, *28*, 517–527. https://doi.org/10.1016/j.ymssp.2011.09.018

Dimitriadis, G., Carrington, I. B., Wright, J. R., & Cooper, J. E. (2002). Blade-Tip Timing Measurement of Synchronous Vibrations of Rotating Bladed Assemblies. *Mechanical Systems and Signal Processing*, *16*(4), 599–622. https://doi.org/10.1006/mssp.2002.1489

Dreier, F., Gunther, P., Pfister, T., Czarske, J. W., & Fischer, A. (2013). Interferometric Sensor System for Blade Vibration Measurements in Turbomachine Applications. *IEEE Transactions on Instrumentation and Measurement*, *62*(8), 2297–2302. https://doi.org/10.1109/TIM.2013.2255993

Gallimore, S. J., & Cumpsty, N. A. (1986). Spanwise Mixing in Multistage Axial Flow Compressors: Part I—Experimental Investigation. *Journal of Turbomachinery*, *108*(1), 2–9. https://doi.org/10.1115/1.3262019

Greitzer, E. M. (1980). Axial compressor stall phenomena. *Journal of Fluids Engineering*, *102*(2), 134–151.

GUIde 5 Consortium. (n.d.). Retrieved July 13, 2017, from https://aeromech.pratt.duke.edu/about

Gwashavanhu, B., Oberholster, A. J., & Heyns, P. S. (2016). Rotating blade vibration analysis using photogrammetry and tracking laser Doppler vibrometry. *Mechanical Systems and Signal Processing*, *76–77*, 174–186. https://doi.org/10.1016/j.ymssp.2016.02.019

Hale, A., Davis, M., & Sirbaugh, J. (2004). *A Numerical Simulation Capability for Analysis of Aircraft Inlet–Engine Compatibility*. ASME GT2004-53473.

Hamed, A., & Numbers, K. (1997). Inlet Distortion Considerations for High Cycle Fatigue in Gas Turbine Engines. *AIAA Paper*, (97–3364).

Heath, S., & Imregun, M. (1998). A Survey of Blade Tip-Timing Measurement Techniques for Turbomachinery Vibration. *Journal of Engineering for Gas Turbines and Power*, *120*(4), 784. https://doi.org/10.1115/1.2818468

Herbert, M., & Pinker, R. (1967). Pressure loss associated with compressible flow through square-mesh wire gauzes (Pressure loss measurements of compressible flow through gauzes with different porosity). *JOURNAL OF MECHANICAL ENGINEERING SCIENCE*, *9*, 11–22.

Holzinger, F., Wartzek, F., Schiffer, H.-P., Leichtfuss, S., & Nestle, M. (2016). Self-Excited Blade Vibration Experimentally Investigated in Transonic Compressors: Acoustic Resonance. *Journal of Turbomachinery*, *138*(4), 041001.

Jackson, N. A. (1972). Theoretical velocity distributions downstream of non-uniform single and multiple smoothing screens. *The Aeronautical Journal*, *76*(736), 251–255.

Johnsen, I. A., & Bullock, R. O. (1965). Aerodynamic Design of Axial-Flow Compressors. NASA SP-36. *NASA Special Publication*, *36*.

Jones, H. (1996). A Nonintrusive rotor blade vibration monitoring system. In *ASME 1996 International Gas Turbine and Aeroengine Congress and Exhibition* (p. V002T02A003–V002T02A003). American Society of Mechanical Engineers.

Kadambi, J. R., Quinn, R. D., & Adams, M. L. (1989). Turbomachinery blade vibration and dynamic stress measurements utilizing nonintrusive techniques. *Journal of Turbomachinery*, *111*(4), 468–474.

Karnik, U., & Tavoularis, S. (1987). Generation and manipulation of uniform shear with the use of screens. *Experiments in Fluids*, *5*(4), 247–254.

Klauke, T., Kühhorn, A., Beirow, B., & Golze, M. (2009). Numerical Investigations of Localized Vibrations of Mistuned Blade Integrated Disks (Blisks). *Journal of Turbomachinery*, *131*(3), 031002. https://doi.org/10.1115/1.2985074

Kurzke, J. (2008). Effects of Inlet Flow Distortion on the Performance of Aircraft Gas Turbines. *Journal of Engineering for Gas Turbines and Power*, *130*(4), 041201-041201-7. https://doi.org/10.1115/1.2901190

Laws, E. M., & Livesey, J. L. (2003, November 28). Flow Through Screens [review-article]. https://doi.org/10.1146/annurev.fl.10.010178.001335

Lemmon, E. W., Huber, M. L., & McLinden, M. O. (2013). NIST Standard Reference Database 23: Reference Fluid Thermodynamic and Transport Properties-REFPROP, Version 9.1,. 2013. *National Institute of Standards and Technology, Standard Reference Data Programm, Gaithersburg*.

Lim, S.-H., Pierre, C., & Castanier, M. P. (2006). Predicting Blade Stress Levels Directly From Reduced-Order Vibration Models of Mistuned Bladed Disks. *Journal of Turbomachinery*, *128*(1), 206. https://doi.org/10.1115/1.2098754

Logan, E., & Roy, R. (Eds.). (2003). *Handbook of turbomachinery* (2nd ed., and expanded). New York: M. Dekker.

Longley, J. P. (1990). Measured and predicted effects of inlet distortion on axial compressors. *ASME Paper*, (90–GT), 214.

Mazzawy, R. S. (1977). Multiple segment parallel compressor model for circumferential flow distortion. *ASME J. Eng. Power*, *99*(2), 288–296.

Möller, D., Jüngst, M., Holzinger, F., Brandstetter, C., Schiffer, H.-P., & Leichtfu\s s, S. (2017). Mechanism of Nonsynchronous Blade Vibration in a Transonic Compressor Rig. *Journal of Turbomachinery*, *139*(1), 011002.

Morrison, E. (2013, May). *Development of a Three Dimensional Compressible Flow Calibration Facility for Thermal Anemometry*. Purdue University.

Neumann, M., Dreier, F., Günther, P., Wilke, U., Fischer, A., Büttner, L., … Czarske, J. (2015). A laser-optical sensor system for blade vibration detection of high-speed compressors. *Mechanical Systems and Signal Processing*, *64–65*, 337–346. https://doi.org/10.1016/j.ymssp.2015.04.026

O'Brien, W. F., & Bailey, J. (2013). The Influence of Duct Development Distance on Screen-Generated Total Pressure Distortion Profiles. American Institute of Aeronautics and Astronautics. https://doi.org/10.2514/6.2013-3602

Plourde, G., & Stenning, A. (1967). The attenuation of circumferential inlet distortion in multi-stage axial compressors. American Institute of Aeronautics and Astronautics. https://doi.org/10.2514/6.1967-415

Procházka, P., & Vaněk, F. (2011). Non-contact systems for monitoring blade vibrations of steam turbines. In *ISMA2012-USD2012* (p. 012116). Retrieved from http://iopscience.iop.org/article/10.1088/1742-6596/305/1/012116/meta

Rao, S. S. (2011). *Mechanical vibrations* (5th ed). Upper Saddle River, N.J: Prentice Hall.

Reinhardt, A. K., Kadambi, J. R., & Quinn, R. D. (1995). Laser Vibrometry Measurements of Rotating Blade Vibrations. *Journal of Engineering for Gas Turbines and Power*, *117*(3), 484. https://doi.org/10.1115/1.2814121

Roberts, F., Plourde, G. A., & Smakula, F. (1968). *Insights into axial compressor response to distortion*. American Institute of Aeronautics and Astronautics.

Russhard, P. (2015). The Rise and Fall of the Rotor Blade Strain Gauge. In J. K. Sinha (Ed.), *Vibration Engineering and Technology of Machinery* (Vol. 23, pp. 27–37). Cham: Springer International Publishing. Retrieved from http://link.springer.com/10.1007/978-3-319-09918-7_2

SAE. (2011). *Gas Turbine Engine Inlet Flow Distortion Guidelines* (Standard No. ARP1420B).

SAE. (2013). *Inlet Total-Pressure-Distortion Considerations for Gas-Turbine Engines* (Standard No. AIR1419B).

Talalayev, A. (2011, August). *On the Renovation of the Three-Stage Axial Compressor Research Facility for Compressor Performance Research*. Purdue University.

Thomassin, J., Vo, H. D., & Mureithi, N. W. (2011). The Tip Clearance Flow Resonance Behind Axial Compressor Nonsynchronous Vibration. *Journal of Turbomachinery*, *133*(4), 041030–041030. https://doi.org/10.1115/1.4001368

Yao, J., Gorrell, S. E., & Wadia, A. R. (2010a). High-Fidelity Numerical Analysis of Per-Rev-Type Inlet Distortion Transfer in Multistage Fans—Part I: Simulations With Selected Blade Rows. *Journal of Turbomachinery*, *132*(4), 041014.

Yao, J., Gorrell, S. E., & Wadia, A. R. (2010b). High-Fidelity Numerical Analysis of Per-Rev-Type Inlet Distortion Transfer in Multistage Fans—Part II: Entire Component Simulation and Investigation. *Journal of Turbomachinery*, *132*(4), 041015.